

1. THE USE OF A LARGE CONVENTIONAL SHOCK TUBE  
AS A PRE-IONIZER FOR AN INVERSE PINCH  
SHOCK TUBE
  
2. THE APPLICATION OF THIN-FILM HEAT TRANSFER  
GAUGES AND FLUSH ELECTROSTATIC PROBES TO  
PARTIALLY IONIZED FLOWS IN SHOCK TUBES

Thesis by  
Alan F. Klein

In Partial Fulfillment of the Requirements  
For the Degree of  
Doctor of Philosophy

California Institute of Technology  
Pasadena, California

1967

(Submitted August 1, 1966)

1. THE USE OF A LARGE CONVENTIONAL SHOCK TUBE  
AS A PRE-IONIZER FOR AN INVERSE PINCH  
SHOCK TUBE

ACKNOWLEDGEMENTS

The author wishes to express his appreciation to two people: Professor H. W. Liepmann, his advisor, and Dr. Z. O. Bleviss, whose interest and encouragement helped to make this thesis possible.

The generous cooperation of J. A. Smith, who made the 6" shock tube available for some of the experiments, and Mrs. Geraldine Krentler, who typed the manuscript, is also gratefully acknowledged.

The author is indebted to the California Institute of Technology, the Aerospace Corporation and the National Science Foundation for various forms of financial assistance. The research was partially supported by the Office of Naval Research.

Finally, the deepest appreciation of all is felt for his wife Ronnie, who sacrificed the most to make this a reality.

## ABSTRACT

A large diameter (17"), conventional shock tube has been used as the pre-ionizer for an inverse pinch shock tube in an attempt to achieve separation of the shock front and the current sheath in the inverse pinch. The inverse pinch was mounted in the endwall of the shock tube and was operated without an anode, either behind the incident or reflected shock wave generated by the pre-ionizer shock tube. The test gases used were Xenon, Argon, and Helium. Separation was not achieved, but in Argon the pressure front did move closer to the front of the current sheath. In Xenon, no improvement in the performance of the inverse pinch was observed as a result of the pre-ionization, and in one case it was noticeably degraded, with the piston appearing to leak excessively. Because of test time limitations it was only possible to operate the inverse pinch behind the incident shock wave in Xenon. By measuring the ionization relaxation time in Xenon it was found that for all the conditions of the present experiments, ionization equilibrium was not attained in the times available. Therefore, the inverse pinch was being operated in a slightly ionized, relaxing gas. The electrical conductivity of such a gas was calculated for Xenon and Argon and the results in Argon were found to be in good agreement with previous shock tube measurements of the conductivity. The relaxation

time measurements, conducted primarily in the GALCIT 6" shock tube, show that  $p_1\tau$ , the product of the initial pressure and the relaxation time behind the incident shock, depends strongly upon the magnitude of  $p_1$ , especially for  $p_1 < .5$  mm Hg of Xenon. The dependence decreases as the Mach number is increased in the range  $10 < M_g < 20.6$ .

## TABLE OF CONTENTS

PART	TITLE	PAGE
	Acknowledgements	ii
	Abstract	iii
	Table of Contents	v
	List of Tables	vii
	List of Figures	viii
I.	Introduction	1
II.	The Combined Operation of an Inverse Pinch and a Conventional Shock Tube	5
	2.1 The Inverse Pinch	5
	2.2 Early Pre-Ionization Experiments	8
	2.3 The Inverse Pinch Mated with the Shock Tube	10
	2.4 The Inverse Pinch with No Top Electrode	12
III.	Compatibility Requirements	14
	3.1 Incident versus Reflected Shock Operation	14
	3.2 Shock Tube Size	18
	3.3 Molecular Weight Effects	19
IV.	Degree of Pre-Ionization	21
	4.1 Ionization Relaxation	21
	4.1a Relaxation in Xenon	21
	4.1b Relaxation in Argon and Helium	24

## TABLE OF CONTENTS (cont.)

PART	TITLE	PAGE
	4.2 Electrical Conductivity	25
V.	Results	30
VI.	Summary and Conclusions	37
Appendices		
A.	Ionization Relaxation Time Measurements in Xenon	40
B.	Equilibrium Electrical Conductivity	56
	References	60
	Tables	62
	Figures	64

LIST OF TABLES

1. Typical operating conditions of 17" shock tube with Helium driver gas.
2. Summary of ionization relaxation time experiments in Xenon.

## LIST OF FIGURES

1. Schematic of typical inverse pinch shock tube.
2. Inverse pinch in the 17" shock tube.
3. Kerr cell pictures of 6" diameter inverse pinch with no top electrode.
4. x-t diagram for combined shock tube operation.
5. x-t diagram including ionization relaxation.
6. Previous relaxation time measurements in Xenon.
7. Ionization relaxation times in Xenon.
8. Electrical conductivity of shock-heated Argon for  $p_1 = 1 \text{ cm Hg}$  (Ref. 17).
9. Relaxing gas conductivity  $\sigma_*$  in Xenon.
10. Pre-ionization in Argon behind the incident shock.
11. Magnetic and pressure probe data without pre-ionization in Argon.
12. Pre-ionization in Argon behind the reflected shock.
13. Pre-ionization in Xenon behind the incident shock.
14. Magnetic and pressure probe data without pre-ionization in Xenon.
15. Pre-ionization in Xenon behind the incident shock.
16. Magnetic and pressure probe data without pre-ionization in Xenon.
17. Pressure probe data in Helium with and without pre-ionization.

LIST OF FIGURES (cont.)

18. Relaxation time definitions and typical continuum intensity oscillogram in Xenon.
19. Schematic of 6" shock tube diagnostics.
20. Relaxation times in Xenon at high initial pressures.
21. Wavelength-integrated, line, and continuum radiation.

## I. INTRODUCTION

From the viewpoint of fluid mechanics and high temperature gas dynamics, interest in electromagnetic shock tubes such as the inverse pinch can be considered as having evolved rather naturally as shock Mach number and gas temperature horizons have expanded. The major steps forward in shock tube technology have been marked by significant developments with respect to the nature of the "piston" used to drive the shock wave. First there were cold and heated compressed gas drivers, then combustion and electric arc drivers. This eventually led to the currently popular use of the energy stored in electromagnetic fields, or electromagnetic drivers. Now several laboratories are working on explosive drivers, in which advantage is taken of the large energy densities stored in explosives. To date such devices have of necessity been of the expendable variety.

The shock velocity regime attainable with electromagnetic drivers is high enough that devices such as the inverse pinch can be considered for use in producing magnetohydrodynamic (MHD) shock waves. In collision-dominated flows (collisionless flows will not be considered here) there are two classes of MHD shock waves, depending on whether the gas ahead of the shock wave is pre-ionized and electrically conducting, or not. For both classes an

external magnetic field parallel to the plane of the shock wave is required. If the gas is not pre-ionized the shock wave is commonly referred to as a gas-ionizing MHD shock, whereas a "true" MHD shock wave is one in which the gas is pre-ionized. Marked differences in the two types of shocks are predicted theoretically and these are summarized in references 1 - 3. The conditions necessary for producing these shocks are also considered.

The early inverse pinch experiments reported by Vlases in reference 2 qualitatively verified these predicted differences. The method of pre-ionization used by Vlases consisted of discharging a capacitor bank into the device, operating it as an inverse pinch. Then after waiting approximately 100  $\mu$ sec the main capacitor bank was discharged, sending out the "MHD shock wave".

As an alternative, the idea was conceived of using a conventional shock tube as the pre-ionizer for the inverse pinch. A discussion of various aspects of combining the two devices, the advantages and difficulties, is presented in sections II and III.

At the time the present experiments were undertaken it was recognized that the inverse pinch, and all electromagnetic shock tubes, did not operate as a shock tube in the sense that the flow field generated did not consist of a shock wave, followed by a region of shock heated gas (the test gas), followed by a piston; but rather, the shock

front was imbedded in the piston and there was no clear "separation" between the shock and the piston under any operating conditions.

Early explanations of this behavior argued that the current sheath, or piston, was diffusing faster than the shock could separate from the piston. If the gas was sufficiently pre-ionized the diffusion would proceed at a slower rate and the shock should be able to move out ahead of the piston. This provided the second source of motivation for the pre-ionization experiments, the attainment of separation in the inverse pinch.

Recently, Sorrell (Ref. 4) has conducted experiments directed towards an understanding of the actual acceleration mechanism in an un-preionized inverse pinch, and he concludes that the diffusion rate provides only part of the explanation. Sorrell considers the problem in terms of how strongly the front of the advancing current sheath interacts with the ambient gas. From this viewpoint if the gas ahead of the current sheath is highly pre-ionized it will interact more strongly with the piston than if it is not pre-ionized. Therefore, either from the point of view of diffusion or degree of interaction the conclusion is the same, namely that pre-ionization should help achieve separation in the inverse pinch.

In the work of both Vlases and Sorrell "snowplow" theory (see Refs. 1, 4) was used to describe the dynamics

of the inverse pinch operation. In snowplow theory the piston is considered as impermeable and infinitely thin, and is assumed to sweep up all of the mass it encounters. Sorrell has relaxed the impermeability assumption and has considered "leaky" pistons. Even more recently, Hoffman (Ref. 5) has solved the conservation equations numerically considering a distributed force field, corresponding to a piston of finite thickness. For such a distributed force field Whitham (Ref. 6) has given an interpretation of the separation problem based on the location in the current sheath of the point at which characteristics first intersect, forming the shock wave. From this point of view the gas need only be pre-heated and the characteristics will converge more rapidly, forming the shock closer to the front of the current sheath and enhancing the possibility of separation.

Due to the fundamental difficulty of achieving separation, the original goal of producing laboratory MHD shock waves was reduced to secondary importance and in all of the present experiments no external magnetic field was used.

## II. THE COMBINED OPERATION OF AN INVERSE PINCH AND A CONVENTIONAL SHOCK TUBE.

### 2.1. The inverse pinch.

Detailed descriptions of standard inverse pinch devices are presented in references 1 and 4. Some pertinent aspects of the previous discussions are repeated in this section since such a review serves as a useful introduction to the present work.

A standard inverse pinch, or cylindrical magnetic shock tube, is shown schematically in figure 1. The device is typically housed in a cylindrical vacuum chamber which contains ports for the radial insertion of probes. Devices have been built ranging in diameter from 6" to more than 18". The capacitor bank is charged to the desired voltage and the discharge is initiated by triggering the ignitron switches. The gas between the two electrodes breaks down in a thin annular sheath close to the center insulator. The self-magnetic field of the current in the center conductor ( $B_\theta$  in figure 1) interacts with the current sheath ( $j_z$ ), providing a  $\underline{j} \times \underline{B}$  or Lorentz force in the radial direction. This force drives the current sheath radially outwards, and the current sheath interacts with and accelerates the gas as it moves outwards. If the current sheath truly acted as a thin, impermeable piston a shock wave would be driven out ahead of the advancing

piston. To study MHD shock waves the external magnetic field is provided by winding a suitable system of coils around the circumference of the device (Ref. 1).

Experience has shown that the velocity of the propagating current sheath is very accurately predicted by "snowplow" theory (see Ref. 1) in which the equation of motion is solved for an infinitely thin, impermeable current sheath which is assumed to sweep up and accelerate all of the mass it encounters. The velocity predicted by this model is a constant called the snowplow velocity  $U_{sp}$  and is given by

$$U_{sp} = \left[ \dot{I}^2 \frac{\mu_0}{8\pi^2 \rho_0} \right]^{1/4}, \quad (1)$$

where  $\mu_0$  is the magnetic permeability of free space,  $\rho_0$  is the initial mass density, and  $\dot{I}$  is the rate of current increase, which is assumed constant. The constant rate of current increase is approximately provided by using the first quarter-cycle of the current pulse (which is a damped sine wave).

Since  $\dot{I}$  approximately equals  $V/L$ , where  $V$  is the capacitor bank voltage and  $L$  is the circuit inductance, the velocity of the current sheath depends only on circuit parameters and the initial gas density in the inverse pinch.

For the present experiments an inverse pinch was constructed with the following parameters:

Diameter	17.1"
Separation between "electrodes"	4 "
Total circuit inductance	0.3 $\mu$ h
Bank capacitance	219.2 $\mu$ f
Typical operating voltage	15 KV

It should be noted that the previous inverse pinch devices built in this laboratory have all been housed in Pyrex vacuum chambers. The present device was built into a section of the conventional shock tube, which is made of stainless steel. This means that for MHD shock studies the external magnetic field would have to be provided by a dc, rather than a pulsed current source.

## 2.2. Early pre-ionization experiments.

The pre-ionization scheme used by Vlases and described in section I suffers from the disadvantage that the discharging of the first capacitor bank sends out several waves that successively accelerate the gas towards the outside of the chamber. The hot gas interacts with the cold outer wall of the chamber and then relaxes back towards the center. Consequently, by the time the main bank is fired the degree of pre-ionization of the gas is unknown, as is the spatial distribution of the gas. In principle the state of the gas could be determined experimentally, as could the spatial variation of the gas properties, but this would have to be done for each set of operating conditions.

This disadvantage of the earlier experiments helped motivate the choice of a conventional shock tube to act as the pre-ionizer, since the gas properties could be determined with fairly good accuracy from just a measurement of the shock Mach number and the initial pressure. In addition one could predict in advance the degree of pre-heating and pre-ionization to be expected under various operating conditions. This was an important factor in the selection of the present technique of pre-ionizing because an accurate description of the state of the pre-ionized gas is an essential prerequisite for any evaluation

of the effect of the pre-ionization on the resulting performance of the inverse pinch.

### 2.3. The inverse pinch mated with the shock tube.

To obtain the configuration used in the present experiments it was necessary to remove the top electrode of the inverse pinch shown in figure 1, rotate it  $90^{\circ}$ , and mount it in the endwall of the conventional shock tube. A scale drawing of this arrangement is shown in figure 2.

The shock tube used in these experiments is the GALCIT 17" shock tube. This facility is described in reference 7. The shock tube was originally constructed for application to problems in rarefied gasdynamics. In such studies it is more important that the densities be low than that the shock Mach number be very high. Consequently the shock tube has good vacuum qualities but limited Mach number capability. This limitation of the shock tube and its affect on the present experiments is discussed in section 3.3.

A purely geometrical problem was posed by the location of the probe ports in the shock tube section available for use in these experiments. The section had four ports located 20 cm from the end of the section, spaced  $90^{\circ}$  apart. It was planned that the probes be located at approximately the mid-plane of the inverse pinch, which would require an axial length of 40 cm if the endwall of the shock tube was also used as the ground electrode of the inverse pinch. Experience has indicated that such large breakdown

distances are undesirable. The problem was resolved by positioning the ground electrode approximately 15 cm into the shock tube as indicated in figure 2. In this way the probes were located at the mid-plane of the inverse pinch with the device 10.2 cm long. The ground electrode of the inverse pinch was also used to support the vacuum by means of an O-ring around its circumference which sealed to the inner wall of the shock tube. This provided an adequate seal for the present experiments, but not as low a base pressure as that obtained with the standard endwall arrangement.

The ground electrode itself was instrumented with a piezo-electric pressure probe which monitored the arrival of the incident shock wave and provided a good timing reference for the firing of the inverse pinch.

#### 2.4. The inverse pinch with no top electrode.

A vital factor in the use of the two devices as shown in figure 2 is the operation of the inverse pinch with no top electrode, or anode. To determine the effect of removing the top electrode one of the smaller inverse pinches (6" dia.) in the laboratory was operated in this manner and Kerr cell pictures were taken at various times after breakdown. Samples of these pictures are presented in figures 3(a) and 3(b) for Argon at an initial pressure of 2 mm Hg and a capacitor bank voltage of 12 KV. In figure 3(b), taken 10  $\mu$ sec after breakdown, a second current sheath has already started to propagate outwards, corresponding to the second half-cycle of the discharge.

A small washer is visible at the top of the center conductor in figures 3(a) and 3(b). This was used to help initiate the breakdown of the gas. In later experiments this was replaced by either a corona ball or a 15° half-angle cone. The cone was used only in the experiments in the 17" shock tube to inhibit the formation of a detached shock at the end of the center conductor.

The Kerr cell pictures indicate that even without the top electrode the breakdown is uniform and the luminous front is extremely plane and stable. In fact, a slight tilting of the luminous front from top to bottom that is noticeable in most Kerr cell pictures taken with a top

electrode, has been eliminated.

Further evidence of the successful operation of the inverse pinch with no top electrode is obtained by plotting  $r-t$  diagrams from magnetic probe data. In all cases the maximum of  $\dot{B}_\theta$  (the time-derivative of  $B_\theta$ ) propagates at a constant velocity and at precisely the velocity predicted by snowplow theory. This property of the propagation of  $\dot{B}_{\theta_{\max}}$  has been used in the past as a criterion for successful operation of the inverse pinch, and in this case is taken to indicate that the device is operating essentially as it does with the top electrode in place. Several  $r-t$  diagrams, both with and without pre-ionization, are presented and discussed in section V.

### III. COMPATIBILITY REQUIREMENTS

Inasmuch as the present experiments involve the simultaneous operation of two distinct devices it seems natural to expect there will be some interface or compatibility problems which arise because something which enhances the operation of one of the devices might detract from the performance of the other.

Throughout the following discussion the shock tube numbering system described in reference 8 will be used. This system is indicated in the x-t diagram of figure 4 for an ideal shock tube.

#### 3.1. Incident versus reflected shock operation.

The first interface problem is related to the option of firing the inverse pinch behind the incident or the reflected shock wave of the 17" shock tube. The original idea envisioned firing the inverse pinch after the pre-ionizing shock wave had reflected from the ground electrode and moved back up the shock tube past the end of the inverse pinch. This corresponds to time  $t_1$  in figure 4. Ideally this would result in the inverse pinch being discharged into a gas at rest and at the equilibrium - 5 (E-5) temperature and degree of ionization, both of which are of course higher than the corresponding values behind the incident shock. However, the density is also much higher than behind the incident shock, and since the snowplow

velocity is proportional to  $\rho_0^{-1/4}$  (Eq. 1) this detracts from the performance of the inverse pinch. Furthermore, the test time behind the reflected shock wave (the time in laboratory coordinates between the passage of the shock and the arrival of the contact surface) is much less than that behind the incident shock, and for many interesting operating conditions of the 17" shock tube (e.g., high Mach numbers and low initial pressures) the length of the test gas slug behind the reflected shock is actually less than the length of the inverse pinch.

When operating behind the incident shock wave the inverse pinch is fired just when the incident shock hits the ground electrode. This corresponds to time  $t_2$  in figure 4. The inverse pinch is then fired into a gas which is moving with axial velocity  $u_p$ , the gas velocity behind the incident shock. This is certainly less desirable than having the gas at rest. However, the radial snowplow velocities are typically an order of magnitude larger than the axial velocity behind the incident shock and the axial gas motion can therefore be neglected. Furthermore, in the present experiments the current sheath propagates at constant velocity for approximately 10  $\mu$ sec. This is therefore the duration of the experiment. The maximum reflected shock velocity is on the order of 1 mm/ $\mu$ sec. If the inverse pinch is fired when the incident shock hits the ground electrode, then in 10  $\mu$ sec the reflected shock

will have traveled a maximum of 10 mm. The inverse pinch is just over 100 mm long so the reflected shock will have traversed less than 10% of the inverse pinch by the time the experiment is completed.

A further complication associated with operation behind the incident shock is provided by the finite ionization relaxation time. This is due to the fact that the internal degrees of freedom adjust more slowly to the large change in energy of the shocked gas than do the translational degrees of freedom. Immediately downstream of the shock wave all properties of the shocked gas may be calculated by assuming that no energy has been invested in internal degrees of freedom. This corresponds to a shock wave in a calorically perfect gas and is known as the region of "frozen flow". Eventually equilibrium is restored between the internal degrees of freedom and the translational degrees. The time associated with the re-establishment of thermal equilibrium is known as the relaxation time.

The ideal  $x-t$  diagram in figure 4 must now be modified to include this important real gas effect. This is done in figure 5 in which only the region in the vicinity of the inverse pinch is shown. The time  $t_1$  now corresponds to operation behind the reflected shock plus the reflected shock relaxation zone (which is much narrower than the incident shock relaxation zone). If the test time is long

enough to permit firing of the inverse pinch at  $t_1$  then equilibrium (E-5) conditions would prevail.

Behind the incident shock (time  $t_2$  in figure 5) conditions are more significantly affected by the presence of the relaxation zone. Since equilibrium is restored by means of collisions between the particles, relaxation times are shorter at high initial pressures and high shock Mach numbers, but in Argon and Xenon at moderate Mach numbers (10-14) and low initial pressures (50 - 200  $\mu$  Hg) the relaxation time can be on the order of 50-100  $\mu$ sec. At shock velocities of  $\sim 2\text{mm}/\mu\text{sec}$  this corresponds to 4-8 inches of length behind the incident shock. Therefore, if the inverse pinch is 4" long, at time  $t_2$  in figure 5 it will be filled with gas that has not yet reached ionization equilibrium. In fact, due to the details of the processes by which equilibrium is approached there may be essentially no pre-ionization of the gas in the inverse pinch, although the gas will have been heated and compressed to the frozen - 2 (F-2) density and temperature (see Appendix A).

### 3.2. Shock tube size.

It is important that the pre-ionizing shock tube be large for two reasons. The first is that the test time is proportional to the square of the shock tube diameter and inversely proportional to the Mach number (Refs. 9 and 10), so that acceptable test times can be obtained at high Mach numbers (and hence high degrees of pre-ionization) by using a large shock tube. Secondly, the larger the diameter of the shock tube, the larger the diameter of the inverse pinch, and the longer the time the current sheath has to propagate out radially. This longer running time gives the radial shock wave more time to move to the front of the current sheath and eventually, to move out ahead.

Making the shock tube as large as possible is not without its disadvantages since the larger the shock tube the more difficult and costly it is to run at high enough Mach numbers to get appreciable pre-ionization and short enough relaxation times.

### 3.3. Molecular weight effects.

Consider now the effects of the molecular weight of the test gas on the performance of the two devices. In a conventional shock tube, for a given pressure ratio across the diaphragm, the resultant shock Mach number increases as the ratio of the driver-to-driven gas sound speeds  $a_4/a_1$  increases. For both driver and driven gases at the same temperature this ratio is maximized by using a light driver gas and a heavy driven gas. As was previously noted the 17" shock tube was not designed as a high Mach number facility. To maximize the Mach number capability of the shock tube it was planned that a Helium driver would be used with Xenon as the driven gas. With  $p_1 = 50 \mu \text{ Hg}$  of Xenon and the highest practical driver pressure (80 psi absolute of Helium) the shock Mach number is 13.5. Table 1 contains a compilation of typical operating conditions for the 17" shock tube with Helium as the driver gas and various driven gases.

On the other hand, one of the experimental observations of Sorrell (Ref. 4) was that as the inverse pinch is operated in heavier and heavier gases the shock front forms farther and farther back in the current sheath. In Hydrogen the shock front is found at the leading edge of the current sheath and in Argon it is found close to the trailing edge. In the present experiments it was found

that in un-preionized Xenon the shock is located even farther back in the current sheath than in Argon.

In view of this very negative effect of gas molecular weight on the inverse pinch, experiments have also been conducted in pre-ionized Argon and Helium, trading 17" shock tube pre-ionization capability for enhanced performance of the inverse pinch. This is felt to be the most serious limitation of using a conventional shock tube as a pre-ionizer for the inverse pinch; namely that it is difficult to generate the high shock Mach numbers necessary for effective pre-ionization in the light gases that are desirable from the viewpoint of inverse pinch performance.

#### IV. DEGREE OF PRE-IONIZATION

##### 4.1. Ionization relaxation.

##### 4.1a. Relaxation in Xenon.

Early in the present work it became apparent that it would not be possible to operate the inverse pinch behind the reflected shock wave in Xenon in the range  $12 < M_s < 14$ . This was mainly due to the limited test time available. Of secondary importance was the fact that at these Mach numbers the density ratio  $\rho_5/\rho_1$  is so high (see Table 1) that the corresponding snowplow velocities behind the reflected shock are too low to be of practical interest. This latter difficulty can be alleviated by operating at much higher voltages.

Once it was acknowledged that operation in Xenon would be restricted to firing behind the incident shock, the magnitude of the relaxation time became a significant parameter of the experiment. A literature search quickly uncovered a paucity of data on ionization relaxation times in Xenon (Refs. 11-13). The shock Mach number and initial pressure ranges of the previous experiments are summarized in Table 2. Included in Table 2 is the size of the shock tube used in each experiment and the diagnostic techniques employed in the determination of the relaxation time. In all three cases both the shock Mach number and initial pressure range were quite limited, with no Mach numbers greater

than 12 and no initial pressures less than .78 mm Hg of Xenon. The results of the previous experiments are plotted in figure 6, in which  $p_1\tau_2$  is plotted versus the shock Mach number\* ( $\tau_2$  is the relaxation time in region 2).

Due to the large disparity in the results of the previous experiments a separate experimental program was undertaken to measure ionization relaxation times in Xenon in the GALCIT shock tubes. Because of the limited Mach number capability of the 17" shock tube, and also the comparatively high cost of operating the large tube, it was decided that the relaxation times would be measured in the higher performance, less costly 6" shock tube. The program consisted of measuring the relaxation time over a wide range of shock Mach numbers and initial pressures in the 6" shock tube, and at a few overlapping conditions in the 17" shock tube. In this way a good estimate could be made of the relaxation time for other conditions in the 17" shock tube.

The present experiments are included in Table 2 and are discussed in detail in Appendix A. The results are plotted in figure 7, in which  $p_1\tau_{1/2}$  is plotted versus shock Mach number, with the initial pressure  $p_1$  as a parameter.  $\tau_{1/2}$  is defined in section III of Appendix A. In figure 7 curves have been drawn through the results for initial pressures

---

\* The results plotted in figure 5 of reference 13 are for  $0.78 < p_1 < 1.20$  mm Hg, but the points are not labeled. Therefore, an average initial pressure of 1.0 mm Hg was assumed.

of 50, 100, and 500  $\mu$  Hg of Xenon. These are the three pressures for which runs were made over a wide enough range of Mach numbers to fit a curve to the data.

The most striking feature of the present measurements is that at a given Mach number  $p_1\tau_{1/2}$  is not independent of pressure, but rather is directly proportional to  $p_1$  (for a discussion of why  $p_1\tau_{1/2}$  should be independent of  $p_1$ , see Ref. 14). Furthermore, as the shock Mach number is increased  $p_1\tau_{1/2}$  becomes less and less a function of  $p_1$ . These and other aspects of the present relaxation time measurements are discussed in Appendix A, including a comparison of the 6" and 17" shock tube results.

#### 4.lb. Relaxation in Argon and Helium.

With respect to Argon, sufficiently accurate values of the relaxation time can be obtained from the results of Petschek and Byron (Ref. 15). Recently, Friedman and Fay have extrapolated the results of Petschek and Byron to higher shock Mach numbers (Ref. 16). However, because of the limited Mach number capability of the 17" shock tube the maximum shock Mach numbers attainable in Argon are on the order of 8 (see Table 1). At these comparatively low Mach numbers and initial pressures the relaxation times are so long that even for operation behind the reflected shock wave the inverse pinch is fired into a relaxing rather than an equilibrium gas.

For operation of the combined shock tubes in Helium the question of ionization relaxation times is irrelevant, since with a Helium-Helium combination in the 17" shock tube the maximum shock Mach number is on the order of 3, and at such a low Mach number the shocked Helium behaves as a calorically perfect gas with no relaxation effects due to lagging internal degrees of freedom.

#### 4.2. Electrical conductivity.

Once it has been determined whether the inverse pinch is being fired into a relaxing gas or one in thermal equilibrium, the degree of pre-ionization may be further specified by calculating the electrical conductivity of the gas. The conductivity depends upon both the temperature and the degree of ionization (or electron number density). If the gas is in thermal equilibrium the calculation is comparatively straightforward. In the limit of either a slightly or highly ionized gas in thermal equilibrium there are equations which apply and these are summarized in Appendix B. For intermediate degrees of ionization a hybrid conductivity suggested by Lin, Resler, and Kantrowitz (Ref. 17) is frequently used. It has generally been found in shock tube experiments in Argon that the measured conductivities are somewhat lower than those predicted theoretically (Ref. 18; no such comparison between experiment and theory has been found for shock-heated Xenon).

In the equilibrium case the degree of ionization (or electron density) is determined from the Saha equation (see Appendix B) and the temperature is given by the shock jump conditions. On the other hand, for a relaxing gas the Saha equation cannot be used, and although the gas temperature can be calculated from the shock jump conditions for a perfect gas, it has been argued in the past that the electron temperature is less than the temperature of the neutrals and

ions (Refs. 15 and 19). This is because for low degrees of ionization the electrons are heated primarily by elastic collisions with the neutrals. Due to the Ramsauer effect the cross-section for this process is small and the heating of the electrons by elastic collisions with the neutrals proceeds at a slow rate. Thus the electron temperature would be lower than the gas temperature while the gas is relaxing (from the Argon results of Wong and Bershader the electron temperature appears to be about a factor of two less than the atom and ion temperature at  $M_s = 16.3$  and  $p_1 = 5$  mm Hg of Argon). However, a recent computer calculation by Kelly (Ref. 20) indicates that in Xenon and Argon at the Mach numbers and pressures of interest in the present experiments, the difference between the electron and atom temperatures is appreciably less than a factor of two (more typically 10%) and in some cases the electron temperature directly behind the shock front is actually higher than the atom temperature. In view of Kelly's results the electron temperature was taken as approximately equal to the atom temperature for the purposes of the present calculations.

The electrical conductivity of a slightly ionized equilibrium gas is given in equation (B-5) of Appendix B.

$$\sigma_0 = 3.84 \times 10^{-10} \frac{\alpha}{QT_e^{1/2}} \text{ mho cm}^{-1}. \quad (\text{B-5})$$

$Q$  is the electron-atom collision cross-section,  $\alpha$  is the

degree of ionization, and  $T_e$  is the electron temperature.

For a slightly ionized, relaxing gas the conductivity may be calculated with  $\alpha$  determined not by Saha's equation, but by integrating the rate equation for the production of electrons, using the activation energies and cross-sectional slope constants measured by Kelly (Ref. 21). The electron temperature is taken equal to the atom temperature as calculated from the shock jump conditions for a calorically perfect gas.

The rate equation for the production of electrons by atom-atom collisions (see Appendix A) is (Ref. 21)

$$\frac{DN_e}{Dt} = 4C_1 N^2 (kT) \left( \frac{kT}{\pi M} \right)^{\frac{1}{2}} \left[ \frac{E_a}{2kT} + 1 \right] \exp \left[ \frac{-E_a}{kT} \right]. \quad (2)$$

$N$ ,  $M$ , and  $T$  are the atom number density, mass and temperature, respectively.  $N_e$  is the electron number density.  $E_a$  is the activation energy and  $C_1$  is the cross-sectional slope constant. For Argon and Xenon the activation energies measured by Kelly are 11.548 and 8.315 ev respectively, and the constants  $C_1$  are  $1.2 \times 10^{-19}$  and  $1.8 \times 10^{-20}$   $\text{cm}^2/\text{ev}$ .  $N$  is the ambient atomic particle density which equals  $N_1(\rho_2/\rho_1)$ , where  $\rho_2/\rho_1$  is the frozen density jump across the shock and  $N_1$  is the initial density ahead of the shock wave. Equation (2) can be integrated by assuming the temperature and density are approximately constant in the region of atom-atom relaxation (regime I of Appendix A).

It is assumed that the electron number density at the shock front ( $t = 0$ ) is negligibly small. In equation (2) the time is particle time rather than laboratory time after the passage of the shock. They are related by

$$t = (\rho_2/\rho_1)t_L ,$$

where  $t_L$  is laboratory time. With  $\alpha = \frac{N_e}{N}$  ,

$$\alpha = 4C_1 t_L \left( \frac{kT}{\pi M} \right)^{\frac{1}{2}} kT \left( \frac{\rho_2}{\rho_1} \right)^2 N_1 \left[ \frac{E_a}{2kT} + 1 \right] \exp \left[ -\frac{E_a}{kT} \right] \quad (3)$$

Equation (3) involves constants, the initial density, time, the atom temperature, and the density jump across the shock. The two latter quantities are determined by the shock Mach number. Therefore,

$$\alpha(M_s, t_L, N_1) = B(M_s) N_1 t_L , \quad (4)$$

where  $B(M_s)$  will depend on whether the gas is Xenon or Argon.

When equation (4) is combined with (B-5), the conductivity for a slightly ionized, relaxing gas is obtained

$$\sigma_* = 3.84 \times 10^{-10} \frac{B(M_s) N_1 t_L}{QT_e^{\frac{1}{2}}} . \quad (5)$$

The conductivity results of Lin, Resler, and Kantrowitz are plotted in figure 8. The open circles

correspond to experimental conditions for which the gas is still relaxing. In the temperature range of 5000-8000°K, the measured conductivities are as much as two orders of magnitude lower than the values predicted according to the equilibrium theory.  $\sigma_*$  has been calculated for these conditions and the results, plotted in figure 8, are seen to be in good agreement with the experimental values.

In view of the good agreement with the results of Lin, Resler, and Kantrowitz for Argon, equation (5) has been used to calculate the conductivity profile in the relaxation zone behind shock waves in Xenon. The results of this calculation are plotted in figure 9, in which the conductivity  $\sigma_*$  has been normalized by the number density ahead of the shock and the time in laboratory coordinates since the passage of the shock wave.

## V. RESULTS

The procedure for the pre-ionization experiments consisted of first choosing an initial pressure and shock Mach number condition for the 17" shock tube, with Argon, Xenon, or Helium as the driven gas (see Table 1). Several runs were made at each condition, with the inverse pinch fired behind either the incident or reflected shock. The pressure and magnetic probes were inserted various distances radially into the inverse pinch to map the trajectory of the pressure front and the current sheath. For each operating condition it was decided whether the ambient gas into which the inverse pinch was fired was relaxing or in thermal equilibrium, based on the earlier results with respect to the ionization relaxation time (section 4.1). The appropriate shock jump conditions were then used to calculate the corresponding "initial" density (the density at the time the inverse pinch was fired). Then, with the inverse pinch removed from the shock tube and operated by itself, each condition of "initial" density and capacitor bank voltage was duplicated, without pre-ionization. Since the snowplow velocity depends only on the bank voltage, the initial density, and constants (equation 1), matching the density and voltage isolates the effect of the pre-ionization and/or pre-heating. The results of these experiments are presented by means of r-t diagrams in figures 10-17.

To minimize the number of 17" shock tube runs required, two magnetic and two pressure probes were used. For each driven gas several test shots were made with the probes at the same radial position in the inverse pinch, and there was generally no more than .1  $\mu$ sec difference between the arrival times of the same event as seen by the two probes of each type. In the reduction of the pressure probe data it was necessary to allow for a delay of approximately .2  $\mu$ sec in the signal, caused by the glass plate at the front of the probe (see Ref. 4).

For the magnetic probe data reduction in the experiments of Vlases and Sorrell (Refs. 1 and 4) the convention was adopted of plotting the time-history of three parts of the bell-shaped  $\dot{B}_\theta$  trace: the onset, the maximum, and the null. However, the onset of  $\dot{B}_\theta$  is often ill-defined, and especially with pre-ionization, is hard to locate accurately and consistently. In the present experiments the front of the current sheath was determined by drawing a tangent to the maximum positive slope of the  $\dot{B}_\theta$  trace and locating the intersection of this tangent with the time axis. The use of the "maximum slope tangent" has resulted in a marked reduction in the scatter in the location of the front of the current sheath.

Figure 10 is a plot of the results with the inverse pinch fired behind the incident shock wave in Argon, with  $p_1 = 100 \mu$  Hg and a shock Mach number of 7.1. Figure 11 is a

plot of the corresponding data without pre-ionization. This is a low enough Mach number that the frozen and equilibrium density jumps  $\rho_2/\rho_1$  are approximately the same and equal to 3.78. Therefore the runs without pre-ionization were made at an initial pressure of  $\sim 378 \mu$  Hg of Argon. The calculated snowplow velocity for this condition is 1.39 cm/ $\mu$ sec. With pre-ionization (figure 10) the velocity of  $\dot{B}_{\theta_{\max}}$  is found to be 1.36 cm/ $\mu$ sec, and without pre-ionization (figure 11) the measured velocity of  $\dot{B}_{\theta_{\max}}$  is 1.46 cm/ $\mu$ sec, both in good agreement with the snowplow prediction. If figures 10 and 11 are superposed, two features become apparent: first that the maximum slope curves are identical, and secondly that the pressure front is closer to  $\dot{B}_{\theta_{\max}}$  with pre-ionization than without. The first result is not surprising in that the amount of pre-ionization behind a  $M_s = 7.1$  shock in Argon is negligible, even at equilibrium, and the rate of diffusion of the front of the current sheath should not be affected significantly by the pre-heating. The second result is more encouraging since the ultimate goal is to cause the pressure front to move forward and eventually out ahead of the current sheath. Furthermore, it is observed that the pressure front without pre-ionization is propagating at somewhat less than the velocity of  $\dot{B}_{\theta_{\max}}$  (1.33 versus 1.46 cm/ $\mu$ sec), whereas with pre-ionization the velocity of the pressure front is precisely

the same as that of  $\dot{B}_{\theta_{\max}}$ .

The second condition run in Argon was  $M_s = 7.8$ ,  $p_1 = 100 \mu \text{ Hg}$ , with the inverse pinch operated behind the reflected shock wave. The inverse pinch was triggered 125  $\mu\text{sec}$  after the incident shock hit the ground electrode, as monitored by the pressure probe mounted in the ground electrode. For this condition the predicted snowplow velocity is 1.13  $\text{cm}/\mu\text{sec}$ , and the measured velocity of  $\dot{B}_{\theta_{\max}}$  with pre-ionization was 1.21  $\text{cm}/\mu\text{sec}$ , and without it was 1.16  $\text{cm}/\mu\text{sec}$ . The r-t diagram for this case is plotted in figure 12, in which the results with pre-ionization are presented, plus the maximum slope curve without pre-ionization. This was done because the rest of the curves (pressure,  $\dot{B}_{\theta_{\max}}$ , and  $\dot{B}_{\theta_{\text{null}}}$ ) without pre-ionization are practically indistinguishable from the corresponding curves with pre-ionization. For example, in both cases the pressure front propagates at precisely the snowplow velocity of 1.13  $\text{cm}/\mu\text{sec}$ . The only significant difference between the pre-ionized and un-preionized results is in the shape of the maximum slope tangent curve. Without pre-ionization (the dashed curve and darkened circles in figure 12) the front of the current sheath propagates at an almost constant velocity that is somewhat faster than that of  $\dot{B}_{\theta_{\max}}$ . This is typical of Argon without pre-ionization. With pre-ionization however, it is seen in figure 12 that the maximum slope curve becomes parabolic, which suggests the growth of the current sheath

(defined here as the separation between  $\dot{B}_{\theta \max}$  and the maximum slope curve, at a given time) is approaching the parabolic diffusion predicted by theory (see Ref. 4, section 3.2).

The results in Xenon are plotted in figures 13-16. Two sets of conditions were run, both with the inverse pinch operated behind the incident shock wave. The first condition was  $M_s = 12.0$ ,  $p_1 = 100 \mu \text{ Hg}$ , and the results with and without pre-ionization are plotted in figures 13 and 14. The two sets of profiles are quite similar. For example, the snowplow velocity for this case is  $1.06 \text{ cm}/\mu\text{sec}$ , and with pre-ionization  $\dot{B}_{\theta \max}$  propagates at  $1.12 \text{ cm}/\mu\text{sec}$ , and without pre-ionization at  $1.02 \text{ cm}/\mu\text{sec}$ . The pressure front with pre-ionization propagates at  $1.02 \text{ cm}/\mu\text{sec}$ , and at  $1.00 \text{ cm}/\mu\text{sec}$  without it. There is no significant difference in either the location of the pressure front or the rate of diffusion of the front of the current sheath with respect to  $\dot{B}_{\theta \max}$  due to the pre-ionization.

For the second condition of  $M_s = 11.8$ ,  $p_1 = 50 \mu \text{ Hg}$ , things are somewhat different. The results with and without pre-ionization are presented in figures 15 and 16. In figure 15 it is seen that the pressure front attenuates as it moves outwards, slipping farther and farther behind  $\dot{B}_{\theta \max}$ , more so than without pre-ionization. Moreover, the predicted snowplow velocity for this case is  $1.26 \text{ cm}/\mu\text{sec}$ , and without pre-ionization  $\dot{B}_{\theta \max}$  propagates at  $1.22 \text{ cm}/\mu\text{sec}$ ,

but with pre-ionization it propagates at 1.48 cm/ $\mu$ sec. This combination of much too high a current sheath speed and attenuation of the pressure front suggests that the current sheath or "piston" is leaking more extensively with pre-ionization than without, for this particular condition.

It is seen in figure 7 that for both conditions in Xenon the ionization relaxation time is longer than 50  $\mu$ sec, which means that in both cases the relaxation length behind the shock wave is longer than the inverse pinch, corresponding to time  $t_2$  in figure 5. Therefore, the electrical conductivity of the relaxing Xenon can be calculated according to section 4.2 and figure 9, but this is rather academic in view of the lack of any positive effect resulting from the pre-ionization in Xenon.

Two conditions were also run in Helium:  $M_s = 3.1$ ,  $p_1 = 50 \mu$  Hg, and  $M_s = 3.1$ ,  $p_1 = 150 \mu$  Hg. The inverse pinch was fired behind the reflected shock in the first case and behind the incident shock in the second case. Figure 17 is a plot of the pressure fronts with and without pre-ionization for the incident shock case. It is included to show there was only a small difference between the measured velocities. The magnetic probe data in Helium was very difficult to interpret because of effects induced by the presence of the probes. In the present experiments it was necessary to encase the probes in Teflon sleeves so

they could withstand the lateral impact loading due to the high pressure driver gas. As a result the probes were appreciably larger than those originally used ( $\frac{5}{8}$ " dia compared to  $\frac{5}{16}$ " dia). The effects are most pronounced in gases for which the pressure is in the front part of the current sheath (Helium and Hydrogen). A series of experiments was conducted with the present inverse pinch in which small magnetic probes were used at the same time as the large ones. In Argon and Xenon there were no essential differences in the measured profiles, except in the rear of the current sheath. In Helium, on the other hand, the  $B_{\theta}$  profile was distorted as soon as the pressure front encountered the probe. For this reason the  $B_{\theta}$  profiles are not presented for the two cases in Helium.

## VI. SUMMARY AND CONCLUSIONS

From an operational point of view the pre-ionization experiments can be considered a success. The inverse pinch has been successfully operated without a top electrode with no degradation in performance. Mated with the 17" shock tube, the combined configuration has been operated in several gases over a wide range of shock Mach numbers. The inverse pinch has been fired behind both the incident and reflected shock waves, and in all but one case the propagation speed of the current sheath was found to agree with that predicted by snowplow theory, using the density calculated from the shock jump conditions for either an equilibrium or frozen gas. The lack of appreciable scatter in the data with pre-ionization is also considered to be a positive factor in view of the fact that each set of curves is the result of several shots at the same condition, involving the reproducibility of not one, but two devices.

On the negative side, separation has certainly not been achieved, nor has anything close to separation. Even in a shock tube as large as the 17" shock tube it has been concluded that it is not possible to operate the inverse pinch behind the reflected shock at high Mach numbers because of test time limitations. On the other hand, when operating behind the incident shock, the relaxation time has been found to be so long that the inverse pinch is

fired into a pre-heated, but not pre-ionized gas. Furthermore, in the light gases found to be desirable from the viewpoint of the inverse pinch, the Mach number capability of any conventional shock tube is so limited that the two devices are practically incompatible.

According to the theoretical model of Hoffman (see section I and reference 5), it is only necessary that the gas be pre-heated and not necessarily pre-ionized for the shock front to move farther forward. This is in consonance with the results of the incident shock series in Argon at  $M_s = 7.1$  (figures 10 and 11). In the reflected shock series in Argon at  $M_s = 7.8$  the diffusion of the front of the current sheath became approximately parabolic, as would be predicted by a simple diffusion argument. However, these results are far from conclusive. In Xenon no advancement of the pressure front was observed with pre-ionization, and in one series the piston appeared to leak excessively, with  $\dot{B}_0$  propagating much faster than snowplow velocity and the pressure front attenuating noticeably.

The relaxation time experiments have shown that at low initial pressures  $p_1 \tau_{1/2}$  is not independent of  $p_1$ , but is strongly dependent upon the magnitude of  $p_1$ , especially at the lower Mach numbers in Xenon. At initial pressures less than 100  $\mu$  Hg, the relaxation times measured in the 17" shock tube were substantially longer than for the same conditions in the 6" shock tube.

A theoretical model was presented for calculating the electrical conductivity of a slightly ionized, relaxing gas that was shown to accurately predict the conductivity measured in earlier shock tube experiments in Argon. Using this model the conductivity was calculated as a function of time behind the incident shock wave in Xenon, for the Mach numbers of interest in the pre-ionization experiments.

## APPENDIX A

## IONIZATION RELAXATION TIME MEASUREMENTS IN XENON

## I. INTRODUCTION

The subject of the approach to ionization equilibrium (ionization relaxation) behind strong shock waves in noble gases has been exhaustively treated both theoretically and experimentally in the past few years (see, for example, Refs. 14, 15, 19). In this appendix the relevant results of previous workers are summarized and the present measurements of the ionization relaxation time in Xenon in both the GALCIT 6" and 17" shock tubes are presented.

## II. THEORY

The passage of a strong shock wave through a gas results in the transfer of a large amount of energy to the gas in an extremely short time. Immediately behind the shock wave all of the energy may be considered as distributed solely among the translational degrees of freedom of the gas. As discussed by Wong and Bershader (Ref. 19), since the average particle energy is small (on the order of 1 to 2 volts), the probability of an excitation or ionization collision is low, so that on the average there are many collisions before the gas gains or loses internal energy. Under these conditions there are many elastic collisions for each inelastic collision and the translational degrees of

freedom are able to remain in equilibrium as ionization relaxation proceeds. In shock tube terminology this is the region of "frozen" flow and all of the gas properties may be calculated neglecting any energy transfer to the internal degrees of freedom. After a certain time has elapsed the internal degrees of freedom are able to equilibrate with the translational degrees and the shocked gas is said to be in thermal equilibrium. This time lag, or incubation period, is called the relaxation time.

The transfer of energy between the various degrees of freedom is accomplished by means of collisions between the gas particles, and the identification and cataloging of the important collision processes for different gases, as well as measurements of the corresponding reaction rates and cross sections have comprised the bulk of the work to date.

For noble gases, such as Argon and Xenon, the approach to ionization equilibrium may be considered in terms of distinct regimes, with each regime characterized by a dominant ionization mechanism. In regime I, which is limited to low degrees of ionization, the most probable ionization mechanisms are atom-atom collisions. For the Argon experiment of Wong and Bershader regime I was limited to a degree of ionization of 0.5%, and in the experiments of Petschek and Byron, also in Argon, regime I accounted for about 10% of the final ionization. In regime II the exceedingly more effective electron-atom processes dominate

the ionization build-up. It is in regime II that most of the ionization takes place.

A third regime (regime III) can be considered in which the degree of ionization is high enough that recombination must also be included. This is because as equilibrium is approached the rates of population and de-population of a particular state must become equal. The recombination can occur radiatively and the experimentally observed sudden onset of continuum radiation emission from the shocked gas is taken as an indication of the start of regime III.

### III. MEASUREMENTS

In the Argon experiments of Wong and Bershader, at shock Mach numbers up to 18, the electron density build-up behind the shock wave was measured by the technique of two-wavelength optical interferometry. They also observed the sudden onset of luminosity, associated with the start of regime III, superposed on the interferograms, and found that this occurred at roughly 80% of the equilibrium degree of ionization. It should be emphasized that they observed the total luminosity, including both continuum and line radiation.

Petschek and Byron also argued that the sudden onset of luminosity was mainly due to electron-ion recombination. Furthermore, since the recombination is proportional to  $N_e^2/T_e^{1/2}$ , where  $N_e$  is the electron number density and  $T_e$  is the electron temperature, and since the variation in electron temperature is small compared with the change in electron density, the luminosity is essentially proportional to  $N_e^2$ . Petschek and Byron photographed the total luminosity (integrated over all wavelengths to which the film was sensitive) with a rotating-drum camera and considered the relaxation time to be defined by the point on the negative at which half the equilibrium (peak) luminosity was reached (they assumed equilibrium was attained for their conditions). With the intensity proportional to  $N_e^2$  this corresponds to

approximately 70% of the equilibrium degree of ionization. They estimated a maximum error of 20% in the determination of the relaxation time.

Yet another definition of the relaxation time was employed in the Xenon experiments of Roth and Gloerson (Ref. 12), and later by Gloerson (Ref. 13). They observed the time-history of the visible continuum emission in the neighborhood of 4970 Å with a spectrograph-photomultiplier combination. Their oscillograms show a short burst of luminosity at the shock front followed by the rapidly rising main signal at the end of the incubation period. A typical intensity versus time continuum profile is shown schematically in figure 18. Roth and Gloerson took as their relaxation time the time between peaks of the two parts of the signal.

Roth and Gloerson attribute the observed visible continuum, at least in part, to the existence of stable excited states of the diatomic Xenon molecule  $\text{Xe}_2$ , rather than entirely to recombination and bremsstrahlung. It is not within the scope of the present work to comment on this hypothesis, but rather merely to determine the magnitude of the ionization relaxation time for the conditions of the present experiment.

The above discussion is intended to highlight the various techniques that have been used to measure the relaxation time, as well as to point out the degree of

arbitrariness that exists with respect to the definition of the ionization relaxation time.

As far as Xenon is concerned, the pertinent parameters of the previous experiments have been summarized in Table 2, including the diagnostic techniques used to determine the relaxation time. The present experiments are also included in Table 2.

For the present experiments it has become convenient to define two relaxation times,  $\tau_0$  and  $\tau_{1/2}$ . Both refer to ionization relaxation behind the incident shock and both are indicated in figure 18.  $\tau_0$  is the time from the shock front to the onset of the main burst of continuum radiation.  $\tau_{1/2}$  is defined as the time from the shock front to the time at which half the peak intensity is attained.

In the 6" shock tube experiments the relaxation time was measured at least three different ways on each run. At one station a photomultiplier monitored the wavelength-integrated luminosity profile behind the incident shock wave. At a second station a monochromator-photomultiplier combination was used to observe either a strong XeI line or a narrow region of the visible continuum. As discussed in Part 2 of this thesis the thin-film heat transfer gauges used to monitor the shock velocity also provide a measurement of the relaxation time  $\tau_0$ . Since two heat transfer gauges were used to determine the shock velocity this actually provided two measurements of  $\tau_0$  on each run. Additionally,

a pressure gauge of the type described by Baganoff (Ref. 22) was mounted in the endwall of the shock tube, and although the gauge measures the pressure history behind the reflected shock, under some conditions it is possible to infer the relaxation time behind the incident shock (for details of this experiment and the associated theoretical analysis see Ref. 23).

For the relaxation time measurements in the 17" shock tube only the monochromator-photomultiplier system and the thin-film heat gauges were used.

## IV. EXPERIMENTAL DETAILS

The GALCIT 6" shock tube is constructed of stainless steel and has an internal diameter of 6". The driven section is 37' long. For these experiments Helium and Hydrogen were the principal driver gases used, although in a few cases the Helium was diluted with Nitrogen to generate some intermediate strength shocks. Research grade Xenon supplied by the Linde Company was used. Before introducing the Xenon for each run the driver section was diffusion pumped to a base pressure of at least  $0.3 \mu$  Hg, which was measured with a McLeod gauge. For additional details on the design and construction of the shock tube see reference 23.

Figure 19 is a schematic of the endwall region of the 6" shock tube, showing the arrangement of the diagnostics. The monochromater, positioned 20 cm from the endwall, was a Jarrell-Ash 0.5 meter Ebert (Model 8200), with a 1P21 photomultiplier at the exit slit. The photomultiplier was typically operated at 700-800 v, with a  $30 K\Omega$  output resistor. When monitoring a Xenon line profile the entrance and exit slits of the monochromater were .02 mm wide ( $0.32 \text{ \AA}$ ). Both slits were opened to a width of  $17.6 \text{ \AA}$  when the continuum was observed. Neutral density filters were used to reduce the incoming light level when operating at the higher pressures and Mach numbers.

As indicated in figure 19, the monochromater was

located at the same axial position as the second thin-film gauge, providing a positive reference as to when the shock wave passed the monochromater. The accuracy of the continuum relaxation time measurement was thereby increased since it was not always possible to locate the shock front on the continuum intensity oscillogram. This is because at high pressures and high shock Mach numbers the main part of the continuum signal becomes much more intense relative to the short burst of luminosity at the shock front, and with a sensitivity sufficient to resolve the peak of the main burst of continuum radiation, the shock front is quite often not resolvable. In addition, since the sidewall gauge also provides a measurement of the relaxation time (see Part 2 of this thesis), it was possible to compare the relaxation time measured by two different techniques at the same axial position in the shock tube.

The photomultiplier tube (931A) which monitored the wavelength-integrated light was positioned 10 cm from the shock tube endwall. The same power supply was used for both this tube and the photomultiplier on the monochromater. Consequently they were both operated at the same voltage for each run. A  $1K\Omega$  output resistor was used for the integrated light measurements.

The shock Mach number was determined by measuring the transit time of the shock wave between the two thin-film heat gauges located 20 and 70 cm from the endwall.

Normally the output of these gauges is amplified and fed into an electronic counter which records the transit time. However, for operation at high shock Mach numbers it is difficult to make a good measurement of the transit time due to non-reproducible triggering of the counter (this is discussed in Part 2). In the present measurements the unamplified output of the heat gauges was displayed on an oscilloscope and the transit time was measured directly from the resulting oscillogram. This introduces two sources of error. First there is the limited accuracy with which the transit time can be measured by eye, and second is the limited accuracy of the sweep speed of the oscilloscope. It is estimated that the shock position can be determined from each heat gauge signal within 2  $\mu$ sec when the transit time is on the order of 250  $\mu$ sec. This corresponds to a maximum error in the transit time of less than 2%. When the transit time is less than 200  $\mu$ sec ( $M_s > 14$ ) each signal can be read with a maximum error of 1  $\mu$ sec and a total error in the transit time of approximately 1%. The sweep speed of the oscilloscope (Tektronix 555) is accurate to 3%. The maximum transit time error is therefore 5%, and by comparing the transit time measured with the counter (for a condition where the counter can be used accurately) with that measured from the oscillogram, it is found that the difference is generally less than 1%.

The shock tube windows used for the continuum and integrated luminosity measurements were Pyrex cylinders 5/8" dia. x 1½" long. The front face of the windows was concave, with the same radius of curvature as the shock tube. The rear face of the windows was plane. For both measurements a multi-slit system was used to provide sufficient axial resolution (in the 17" shock tube experiments an additional slit was introduced by evaporating a thin film of platinum over all but a narrow vertical slit of the front face of the window).

## V. RESULTS

The results of the present measurements of the ionization relaxation time in Xenon are presented in figure 7 in which  $p_1\tau_{1/2}$  is plotted versus the shock Mach number. Both the 6" and 17" shock tube data are presented. As noted in section 4.1a of this thesis, the present results indicate a strong dependence of  $p_1\tau_{1/2}$  on the magnitude of  $p_1$ . For example, at  $M_s = 12$  the value of  $p_1\tau_{1/2}$  for  $p_1 = 500 \mu \text{ Hg}$  is more than five times larger than the value of  $p_1\tau_{1/2}$  at the same Mach number and  $p_1 = 50 \mu \text{ Hg}$ .

The observed behavior is attributed to the presence of impurities. Whether they are predominantly volume impurities due to outgassing of the shock tube (see Refs. 13 and 24), or surface impurities due to the relatively dirty walls of the shock tube is not completely clear, although the former is believed much more likely.

The duration of regime I, in which atom-atom collisions dominate the production of electrons, is limited by the time at which enough electrons become available to take over the ionization. If some impurities are present with relatively large Xenon-impurity inelastic collision cross-sections the atom-atom regime could be shortened markedly, with a resulting decrease in the relaxation time. If an approximately constant impurity level is assumed in the shock tube, independent of  $p_1$ , then one would expect

impurities to play a more dominant role at lower initial pressures. Therefore, at any Mach number, smaller values of  $p_1\tau_{1/2}$  would be predicted for the lower values of  $p_1$ . This is the behavior exhibited by the present results. Also, the impurity effects should be biggest at the lowest Mach numbers, since at high shock Mach numbers the relaxation time is getting so short that the magnitude of the relaxation time is no longer dominated by the extent of regime I. Consequently, less of a dependence of  $p_1\tau_{1/2}$  on  $p_1$  is expected at high Mach numbers. This trend is also observed in the present experiments.

These effects are not as apparent in the previous experiments for several reasons. In the first place the shock Mach number and initial pressure ranges were too narrow. Secondly, because of the small size of the shock tubes used it was necessary to run at relatively high initial pressures or else the relaxation time would be longer than the test time, and as is evident from the present measurements these effects are much more apparent at low initial pressures. Thirdly, in the previous experiments runs were not made at a constant initial pressure over a wide range of Mach numbers which again makes these trends more apparent. In spite of these reasons, the original data of Turner do indicate a dependence of  $p_1\tau$  on  $p_1$ , even over the narrow range of his experiments. For  $M_s = 9$ , the ratio of the measured relaxation time at  $p_1 = 5$  mm to that at

$p_1 = 20$  mm is 2.25 instead of 4, and at  $M_s = 9.5$  the ratio is 3 instead of 4 (note also that the ratio is increasing with increasing  $M_s$ , as predicted).

As was noted earlier (see Table 2) almost all of the previous experiments were at values of  $p_1$  greater than 0.75 mm Hg. It is therefore interesting to compare the results of Turner and Gloerson with the present measurements, only using the data from the present experiments corresponding to initial pressure greater than 0.75 mm Hg. It was noted in Turner's thesis that subsequent measurements of his with purer Xenon resulted in relaxation times five times longer than his original values. In the present comparison the values given in Turner's thesis have been multiplied by a factor of five. The results of this comparison are plotted in figure 20. In view of the different definitions of relaxation time used in each of the experiments and the different shock tube sizes, as well as the other obvious differences in initial conditions and techniques, it is felt that in the limit of high  $p_1$  the results are in surprisingly good agreement. It must be emphasized that the highest  $p_1$  used in the present experiments was 1.5 mm Hg whereas Turner's results are for initial pressures between 5 and 20 mm Hg, and Gloerson's results are for initial pressures between .78 and 1.20 mm Hg.

Also included in figure 7 are the ionization relaxation times measured in the 17" shock tube. The results are

plotted for initial pressures of 25, 50, and 100  $\mu$  Hg of Xenon, in the Mach number range of 11.5 to 14.5. The 100  $\mu$  shots agree quite well with the 100  $\mu$  curve from the 6" shock tube. The relaxation times for  $p_1 = 50 \mu$  Hg are 2 - 2.5 times longer than the corresponding 6" shock tube results. There is no 25  $\mu$  curve for the 6" shock tube but it is seen in figure 7 that the 25  $\mu$  results from the 17" shock tube lie above the 50  $\mu$  curve for the 6" shock tube.

If the dependence of  $p_1 \tau_{1/2}$  on the magnitude of  $p_1$  is considered in terms of volume impurities due to outgassing of the shock tube, then the magnitude of the effect should be inversely proportional to the volume-to-surface ratio of the shock tube. The 6" and 17" shock tubes are similar in construction and materials, with the volume-to-surface ratio 2.85 times larger for the 17" shock tube. Therefore at low initial pressures there should be less of an impurity effect in the 17" shock tube and the relaxation times should be longer than the corresponding values for the 6" shock tube. This is seen to be the case for  $p_1$  less than 100  $\mu$  Hg of Xenon.

Figure 21 is a presentation of typical wavelength-integrated, line, and continuum radiation oscillograms for a  $M_s = 13.6$  shot into 50  $\mu$  Hg of Xenon. The line profile oscillogram (XeI 4624 Å) is seen to return quickly to zero

intensity after the passage of the main signal, whereas the continuum and integrated-wavelength oscillograms indicate a subsequent burst of radiation, which is believed to be associated with the arrival of the contact surface. The origin of this luminosity was not investigated in detail, but is apparent from the XeI 4624 Å profile that it is not due to Xenon line radiation.

## APPENDIX B

## EQUILIBRIUM ELECTRICAL CONDUCTIVITY

For a completely singly ionized gas in thermal equilibrium the electrical conductivity as given by Spitzer and Härm (Refs. 17 and 25) in cgs units is

$$\sigma = \frac{0.591 (kT)^{3/2}}{m_e^{1/2} e^2 \ln(h/b_0)} \quad (B-1)$$

where  $k$  is Boltzmann's constant,  $m_e$  is the electron mass,  $e$  is the electronic charge, and  $T$  is the temperature.  $b_0$  is the impact parameter at which a positive ion deflects a mean-energy electron by 90 degrees, and  $h$  is the Debye shielding distance,

$$b_0 = \frac{e^2}{3kT} \quad \text{and} \quad h^2 = \frac{kT}{8\pi n_e e^2} \quad (B-2)$$

where  $n_e$  is the electron number density. Putting in the numerical values of the constants and the appropriate conversion factor leads to

$$\sigma_d = \frac{1.54 \times 10^{-4} T^{3/2}}{\log(h/b_0)} \text{ mho cm}^{-1} \quad (B-3)$$

This conductivity is frequently referred to as  $\sigma_d$  since its calculation is based on the assumption that the electron mobility is determined solely by distant encounters with the ions.

If a slightly ionized gas of rigid sphere molecules is considered, in which the electron mobility is dominated by close encounters between the electrons and the neutrals, the conductivity in cgs units is

$$\sigma_o = \frac{0.532 \alpha e^2}{(m_e kT)^{\frac{1}{2}} Q} \quad (\text{B-4})$$

$Q$  is the electron-atom collision cross section and  $\alpha$  is the degree of ionization (Ref. 26). Again, inserting the constants and a conversion factor leads to

$$\sigma_o = 3.84 \times 10^{-10} \frac{\alpha}{QT^{\frac{1}{2}}} \text{ mho cm}^{-1} . \quad (\text{B-5})$$

In many experiments the degree of ionization is such that neither limit strictly applies and for this intermediate regime it was proposed by Lin, Resler, and Kantrowitz (Ref. 17) that the conductivity be approximated by

$$\frac{1}{\sigma} = \frac{1}{\sigma_o} + \frac{1}{\sigma_d} . \quad (\text{B-6})$$

The above equation simply says that the total resistivity of the gas ( $1/\sigma$ ) is equal to the sum of the resistivity due to close encounters between the electrons and the neutrals, and the resistivity due to distant encounters between the electrons and positive ions.

Experience has shown that equation (B-3) for  $\sigma_d$  is applicable even for substantially less than full ionization. In fact even for degrees of ionization as low as 1% (and lower), the conductivity is still dominated by the contribution due to the distant encounters.

When the assumption of thermal equilibrium is applicable the electron number density and/or the degree of ionization is determined from Saha's equation, which can be written in the form (Ref. 27)

$$\frac{c_+^2}{1-c_+} = \left[ 3.35 \times 10^{-2} \frac{\text{Newtons}}{(\text{Meter})^2 (\text{OK})^{5/2}} \right] \left( \frac{g_+ g_e}{g_1} \right) \frac{T^{5/2}}{P} e^{-\frac{T_i}{T}} \quad (\text{B-7})$$

$T_i$  is the characteristic ionization temperature (i.e., the ionization potential expressed as a temperature), and the  $g$ 's are the statistical weights. The subscripts +, e, i refer to ions, electrons, and neutrals, respectively.

$c_+ = \frac{\rho_+}{\rho}$  is the ion-mass-fraction and  $P$  is the total pressure.

When the theoretically computed values of the conductivity are compared with experimentally measured values it has generally been found that the experimental values are lower than those predicted by equations (B-1) - (B-7) by 30-50% (for a survey of existing results in shock-heated Argon see reference 18). Of particular interest are the Argon experiments of Lin, Resler, and Kantrowitz (Ref. 17).

Their conductivity results are plotted in figure 8. The darkened circles represent experimental values of the conductivity obtained under conditions in which the shocked gas had attained ionization equilibrium, and the results agree quite well with the theory summarized in this appendix (as indicated in figure 8, these points also happen to correspond to degrees of ionization high enough that the conductivity is determined predominantly by distant encounters).

The open circles in figure 8 represent experimental values of the conductivity for conditions under which the shocked gas is still relaxing. In the temperature range of 5000-8000°K the measured conductivities are as much as two orders of magnitude lower than the theoretical values predicted by the equilibrium theory. A theoretical calculation of the electrical conductivity of this slightly ionized, relaxing gas is discussed in section IV of this thesis and the results are plotted in figure 8 (the line  $\sigma_*$ ).

## REFERENCES

1. Vlases, G. C., Ph.D. Thesis, Caltech (1963).
2. Vlases, G. C., Phys. Rev. Letters (1964), 12, pp. 43-45.
3. Vlases, G. C., Phys. Fluids (1964), 7, pp. 1358-1365.
4. Sorrell, F. Y., Ph. D. Thesis, Caltech (1966).
5. Hoffman, A. L., "A Conical Model for the Diffusive Piston in an MHD Shock Tube", to be published.
6. Whitham, B. G., Private communication (1966).
7. Liepmann, H. W., Roshko, A., Coles, D., and Sturtevant, B., Rev. Sci. Instr. (1962), 33, pp. 625-631.
8. Liepmann, H. W., and Roshko, A., Elements of Gasdynamics, John Wiley and Sons, New York (1957).
9. Roshko, A., Phys. Fluids (1960), 3, pp. 835-842.
10. Mirels, H., Phys. Fluids (1963), 6, pp. 1201-1214.
11. Turner, E. B., Ph. D. Thesis, U. of Michigan (1956); also ASTIA Document No. AD86309.
12. Roth, W., and Gloerson, P., J. Chem. Phys. (1958), 29, pp. 820-824.
13. Gloerson, P., "Some Unexpected Results of Shock Heating Xenon", General Electric Space Sciences Laboratory, R60SD364 (1960).
14. Weymann, H. D., "On the Mechanism of Thermal Ionization Behind Strong Shock Waves", U. of Maryland Tech. Note BN-144 (1958).
15. Petschek, H., and Byron, S., Ann. Phys. (1957), 1, pp. 270-315.
16. Friedman, H., and Fay, J. A., Phys. Fluids (1965), 8, pp. 1968-1975.
17. Lin, S. C., Resler, E. L., and Kantrowitz, A., J. Appl. Phys. (1955), 26, pp. 95-109.

## REFERENCES (cont.)

18. Zien, T. F., "The Electrical Conductivity of Shock-Ionized Argon", AFOSR 64-1488 (1964).
19. Wong, H., and Bershader, D., "Interferometric Study of Thermal Equilibrium of a Shock Heated Plasma", Stanford University (1964).
20. Kelly, A. J., Private communication (1966).
21. Kelly, A. J., Ph. D. Thesis, Caltech (1965).
22. Baganoff, D., Ph. D. Thesis, Caltech (1964).
23. Smith, J. A., Ph. D. Thesis, Caltech (1967).
24. Bond, J. W., Phys. Rev. (1957), 105, pp. 1683-1694.
25. Spitzer, L., and Härm, R., Phys. Rev. (1953), 89, pp. 977-981.
26. Chapman, S., and Cowling, T. G., The Mathematical Theory of Non-Uniform Gases, Cambridge University Press, Cambridge, England (1952).
27. Cole, J. D., Ae 235 Notes, Caltech (1964).

GAS	P <sub>1</sub> (μ Hg)	P <sub>4</sub> (psia)	M <sub>s</sub>	T <sub>2-F</sub> (°K)	T <sub>2-E</sub> (°K)	α <sub>2-E</sub> (%)	(ρ <sub>2</sub> /ρ <sub>1</sub> ) <sub>F</sub>	(ρ <sub>2</sub> /ρ <sub>1</sub> ) <sub>E</sub>	T <sub>5-E</sub> (°K)	α <sub>5-E</sub> (%)	(ρ <sub>2</sub> /ρ <sub>1</sub> ) <sub>E</sub>
Helium	150	45	3.1	1,000	1,000	0	3.05	3.05	2,300	0	6.9
Helium	50	22	3.1	1,000	1,000	0	3.05	3.05	2,300	0	6.9
Argon	100	22	7.1	5,000	5,000	0	3.78	3.78	9,000	5.5	10.4
Argon	100	45	7.8	6,000	6,000	.04	3.81	3.83	9,400	7.2	11.5
Xenon	50	22	11.8	14,400	7,600	10.2	3.92	7.2	9,600	24.2	43
Xenon	100	45	12.0	14,700	7,900	11.1	3.92	7.2	10,000	25.3	44

Table 1. Typical Operating Conditions of 17" Shock Tube with Helium Driver Gas.

EXPERIMENT	$M_s$	$p_1$ , mm Hg	SHOCK TUBE SIZE	SHOCK TUBE MATERIAL	DIAGNOSTICS
Turner Ref. 11 (1956)	8.5-11	5-20	$1\frac{5}{8} \times 2\frac{5}{8}$ "	Cold-drawn steel	Wavelength-integrated luminosity; time resolution provided by rotating drum camera
Roth and Gloerson Ref. 12 (1958)	* 8-11	0.5-4.0	1" I.D.	Stainless steel/ Pyrex	Continuum radiation intensity; time resolution provided by spectrograph-photomultiplier combination
Gloerson Ref. 13 (1960)	10-12	.78-1.20	2" I.D.	Stainless steel/ Pyrex	(1) Time-resolved spectroscopy both continuum and line radiation (2) Wavelength-integrated luminosity; light-pipe, photomultiplier combination
Klein and Smith GALCIT 6" Shock Tube (1966)	10-20.6	.05-1.5	6" I.D.	Stainless steel	(1) Time-resolved continuum intensity (2) Wavelength-integrated luminosity (3) Thin-film heat gauges (4) Endwall pressure gauge
Klein GALCIT 17" Shock Tube (1966)	11.6-13.6	.025-.1	17" I.D.	Stainless steel	(1) Time-resolved continuum intensity (2) Thin-film heat gauges

\* Friedman and Fay have extrapolated these results to  $M_s = 20$  (Ref. 16)

Table 2. Summary of Ionization Relaxation Time Experiments in Xenon

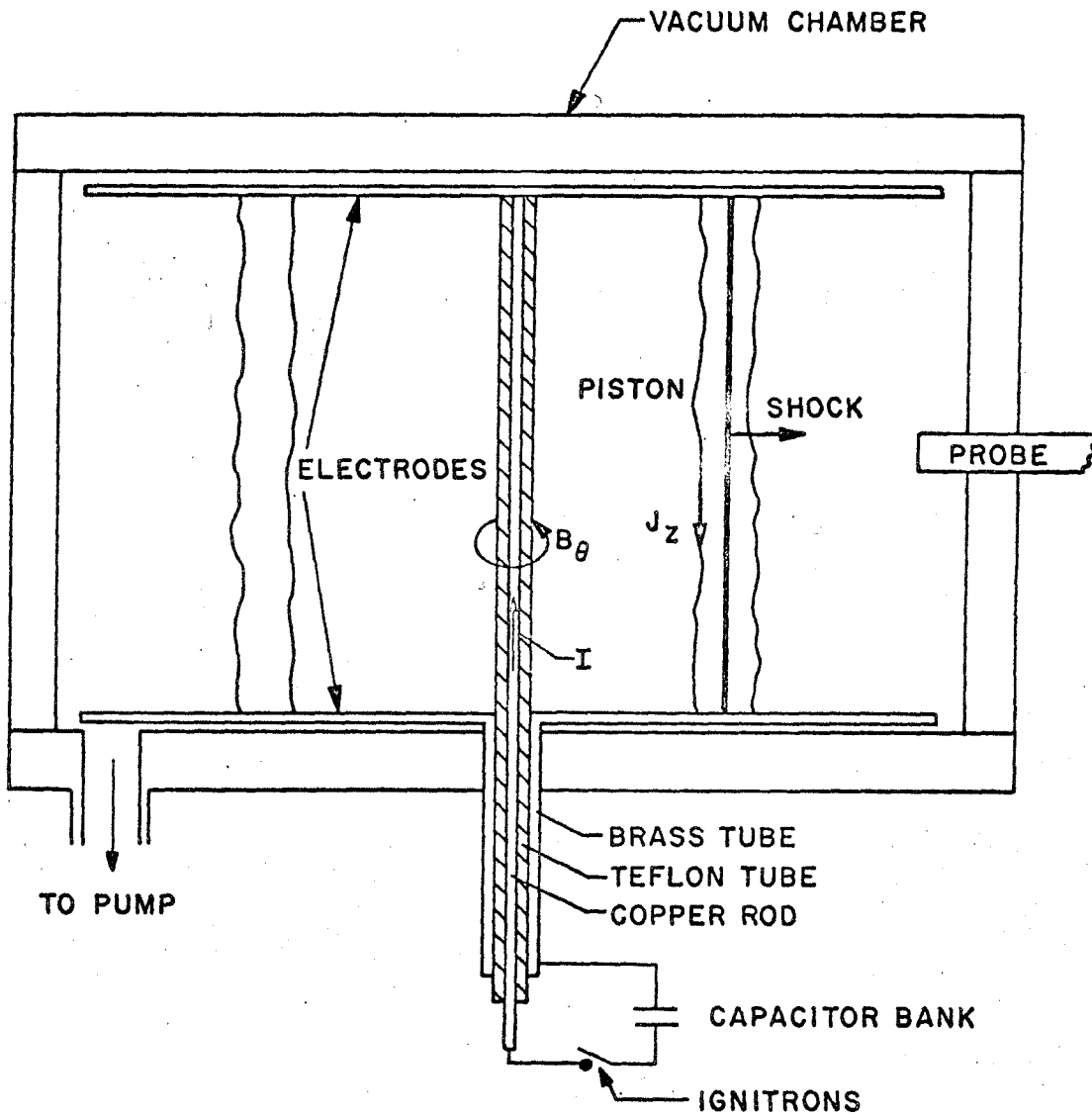


Figure 1. Schematic of typical inverse pinch shock tube.

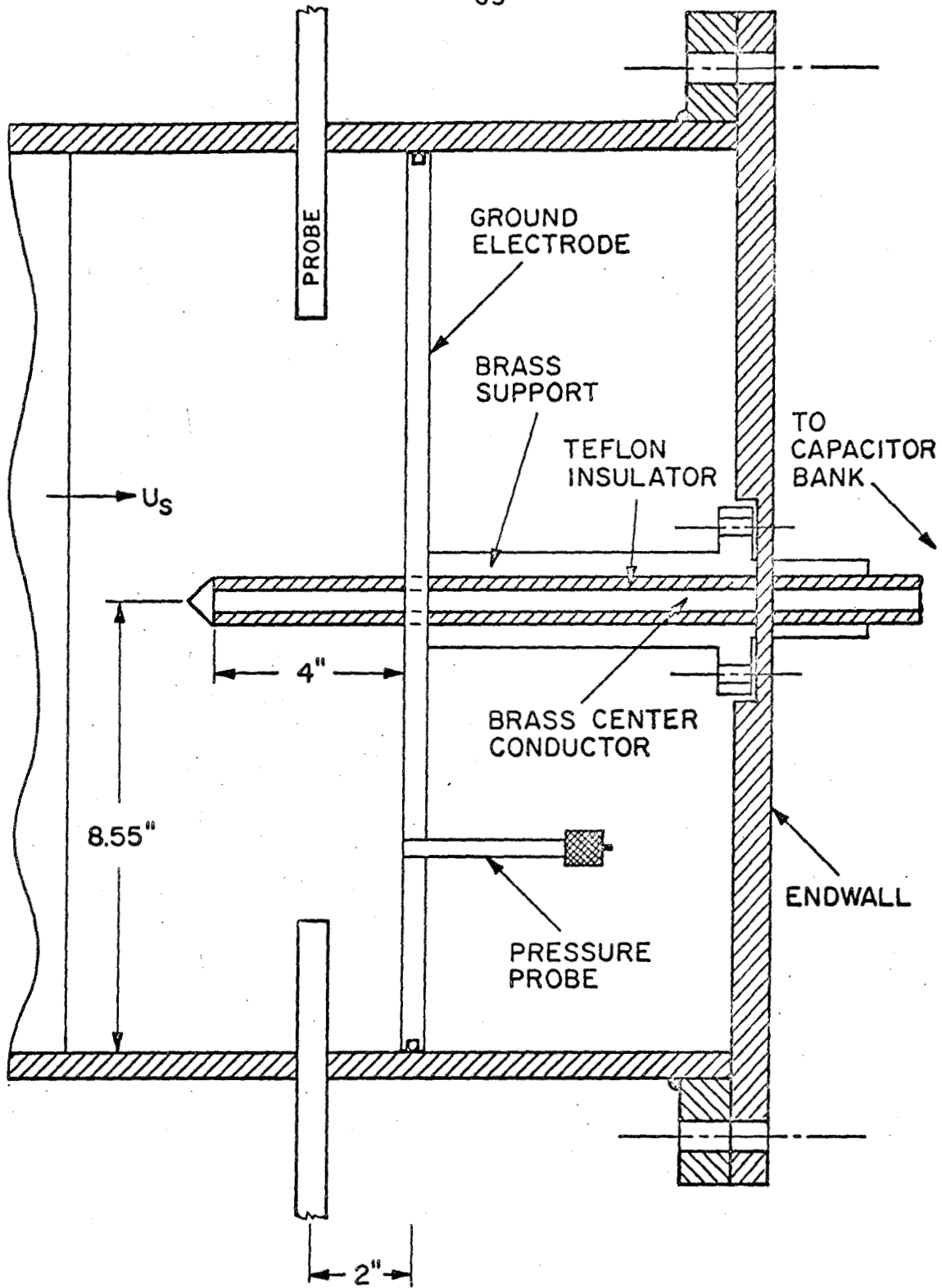
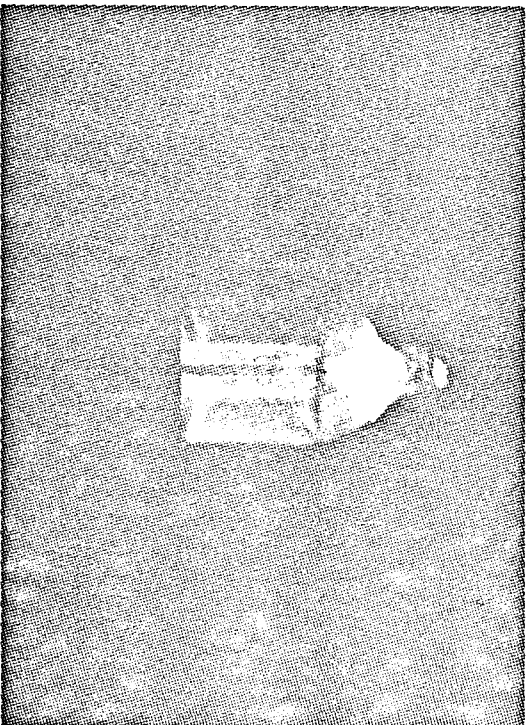


Figure 2. Inverse pinch in the 17" shock tube.



(a) 4  $\mu$ sec after breakdown.



(b) 10  $\mu$ sec after breakdown.

Figure 3. Kerr cell pictures of 6" diameter inverse pinch with no top electrode. Initial pressure 2 mm Hg of Argon. Capacitor bank voltage 12 KV. Exposure time .05  $\mu$  sec.

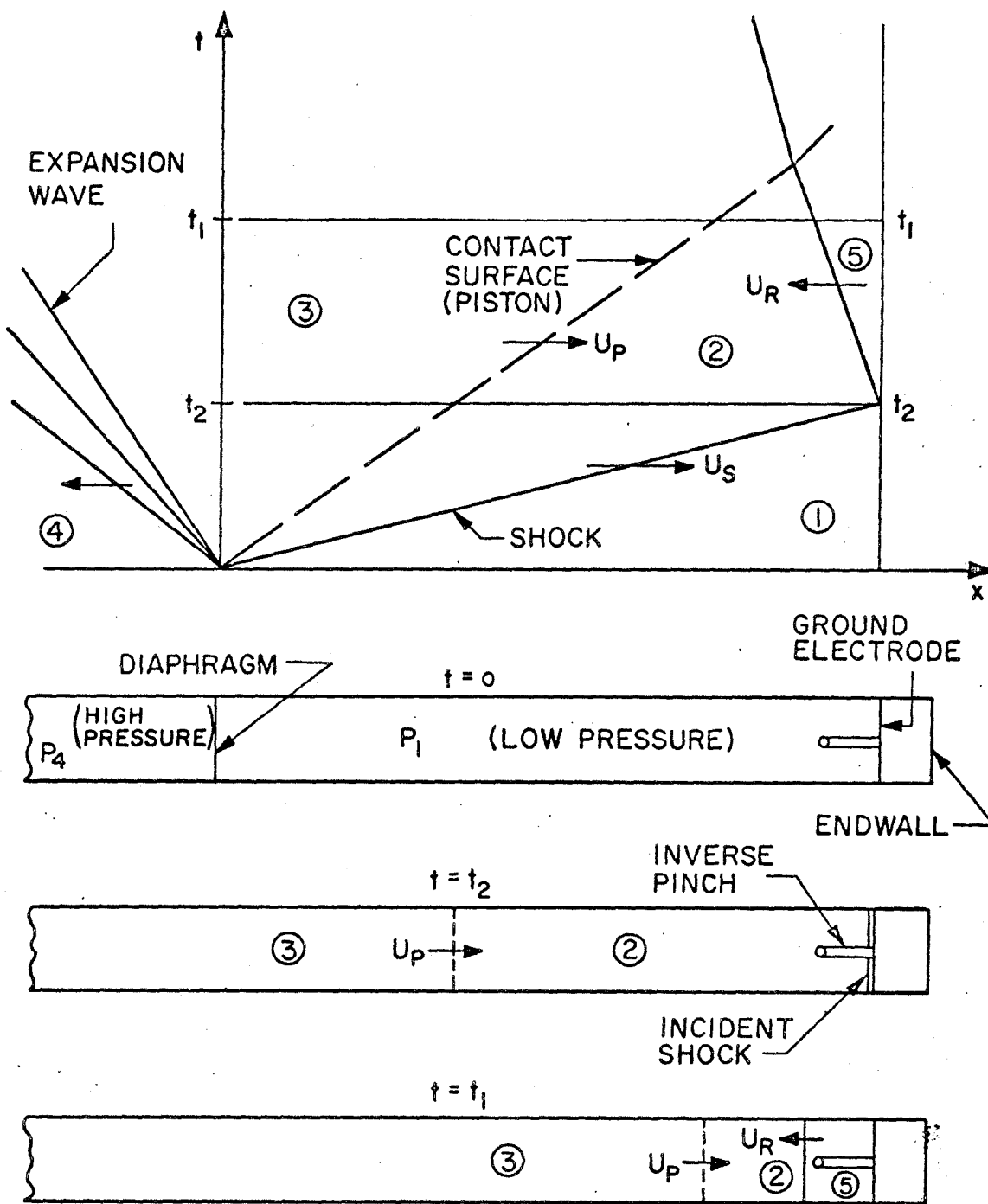


Figure 4.  $x-t$  diagram for combined shock tube operation.

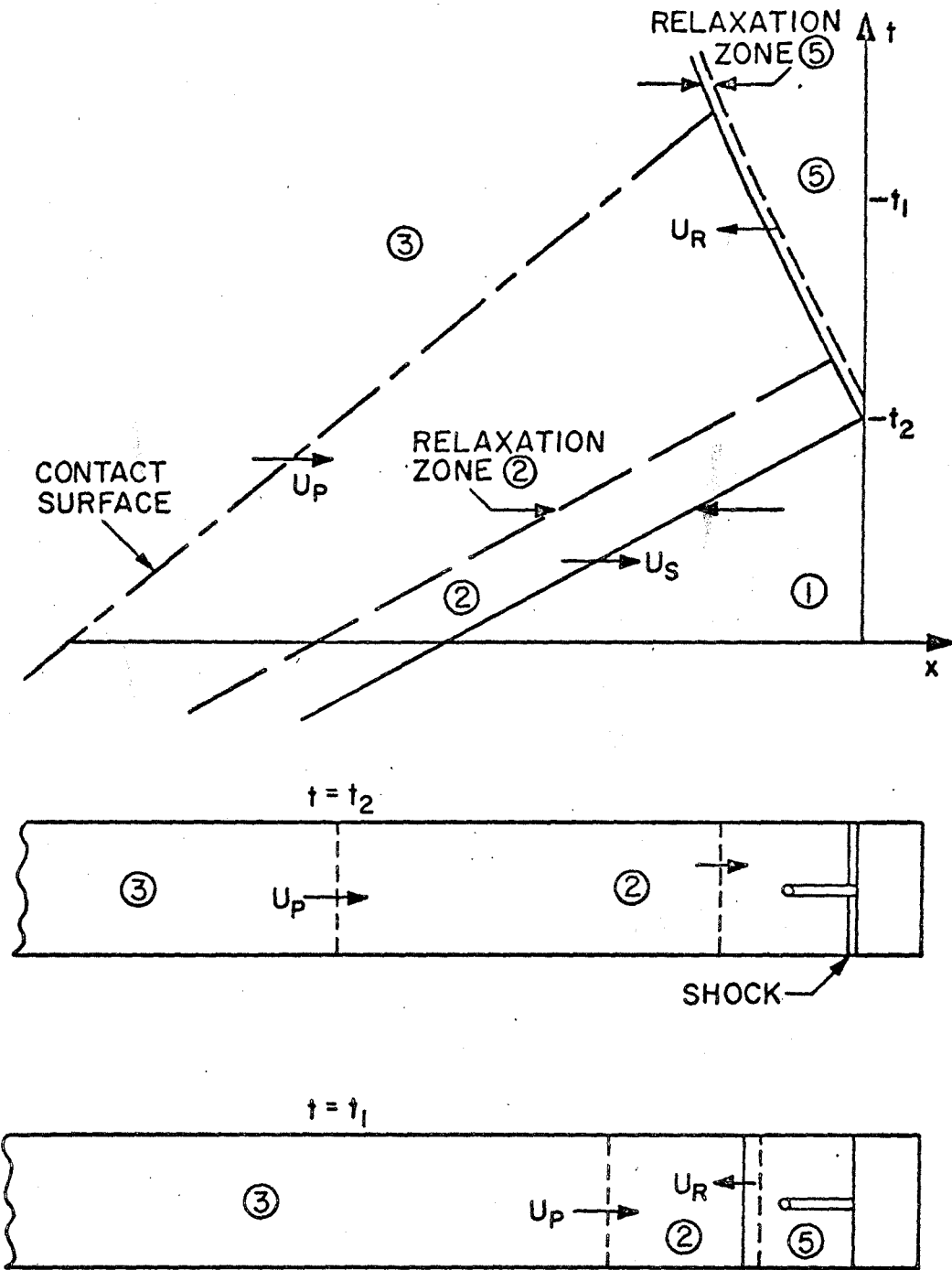


Figure 5.  $x-t$  diagram including ionization relaxation.

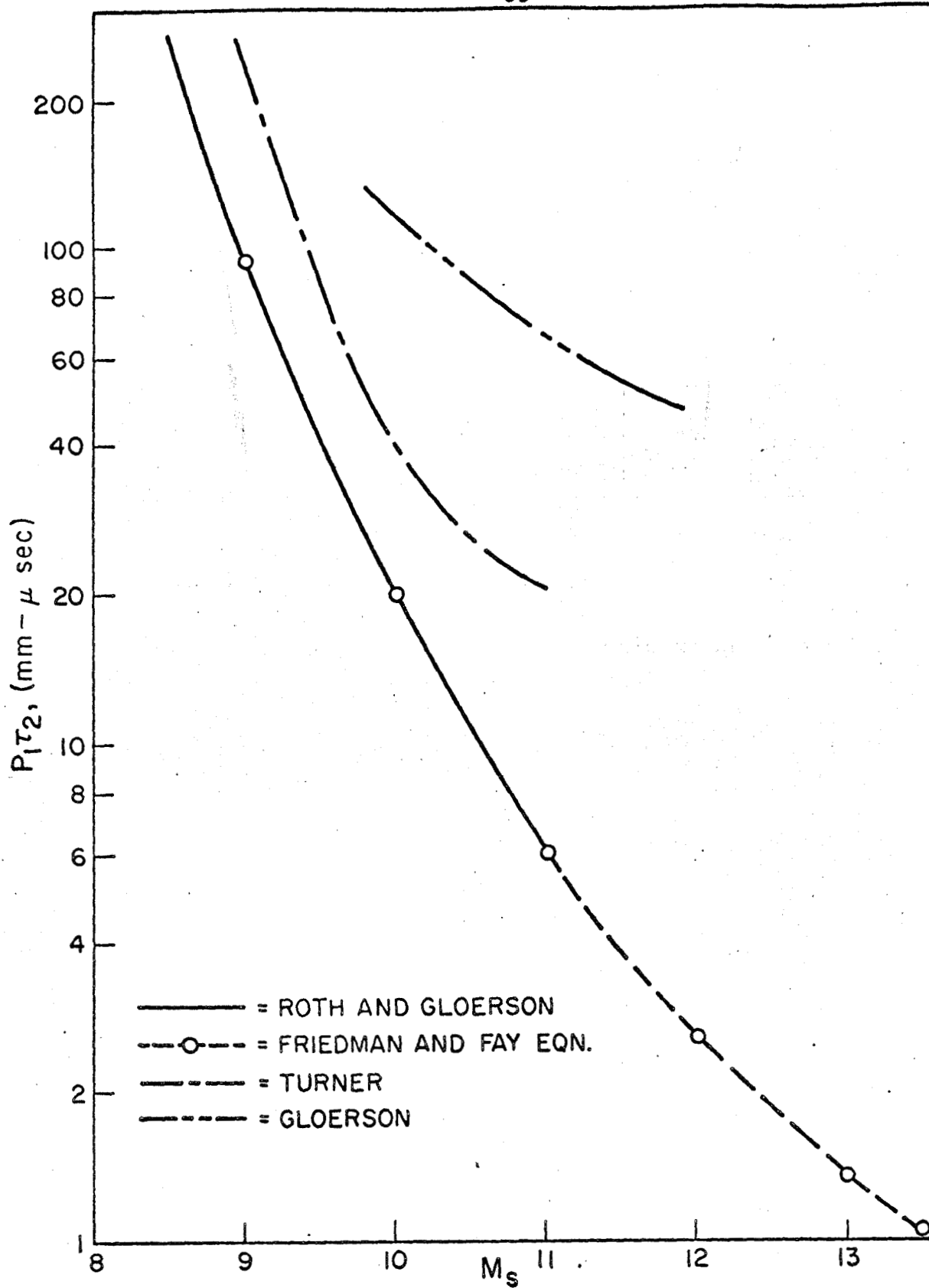


Figure 6. Previous relaxation time measurements in Xenon.

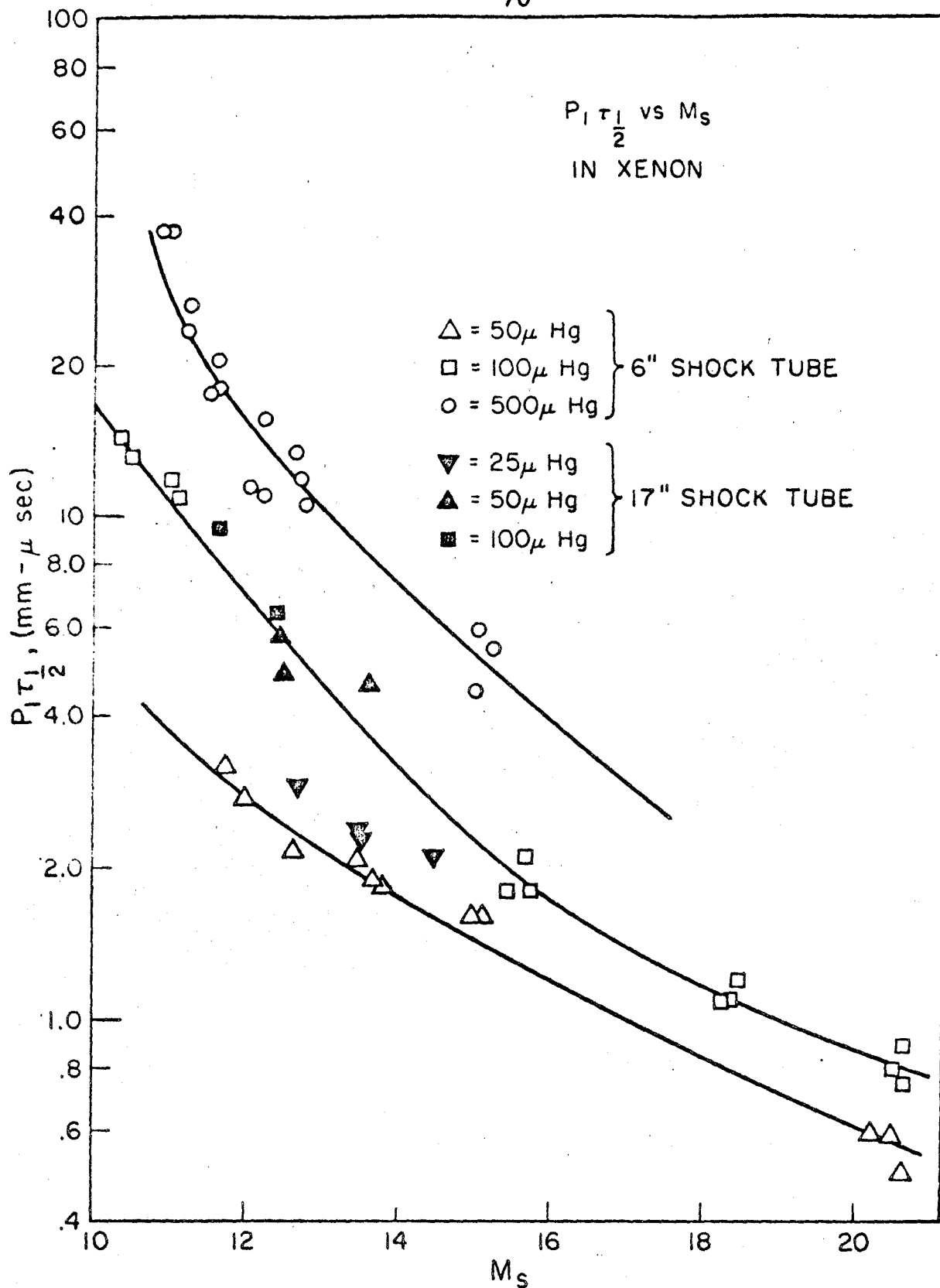


Figure 7. Ionization relaxation times in Xenon.

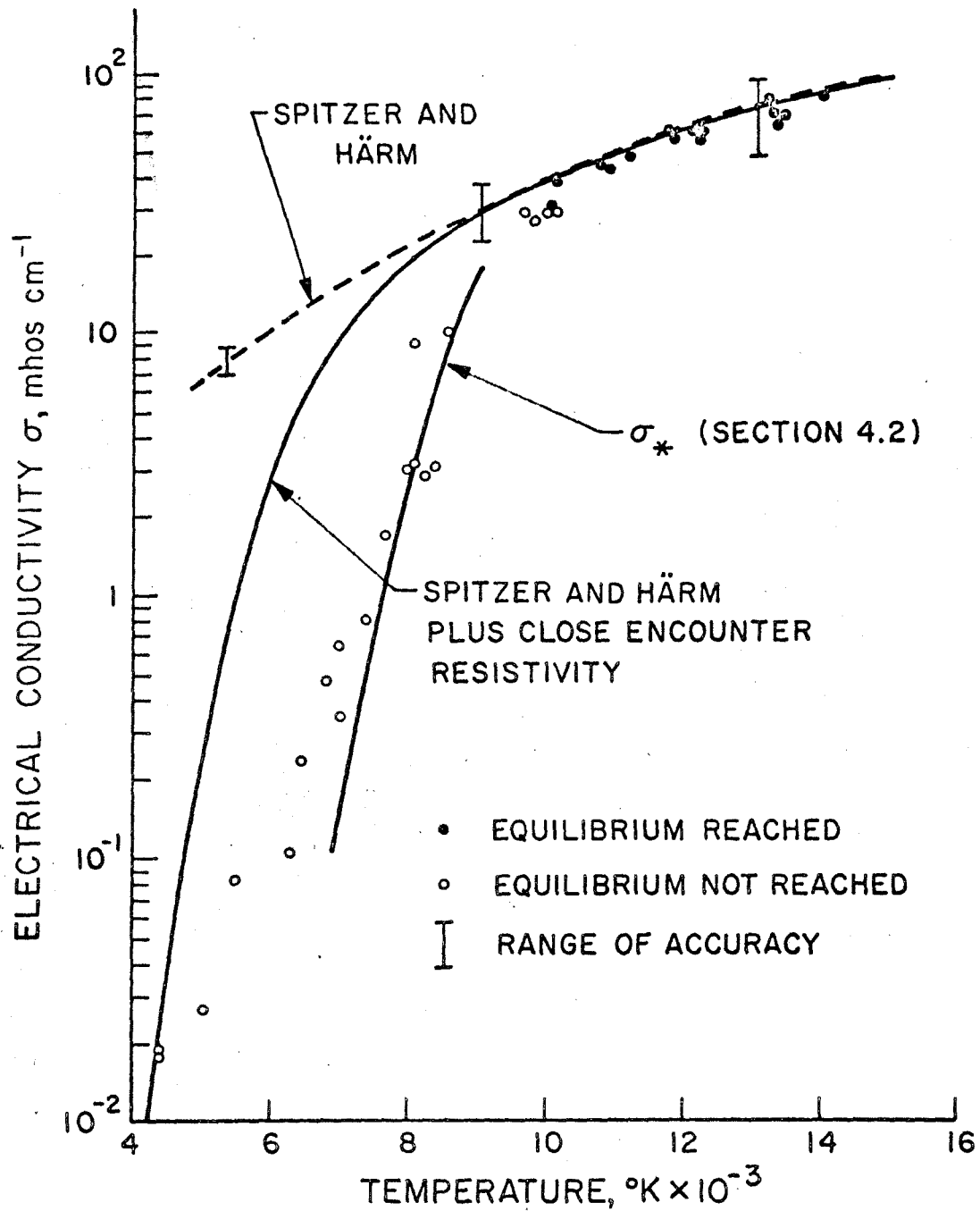


Figure 8. Electrical conductivity of shock-heated Argon for  $p_1 = 1$  cm Hg (Ref. 17).

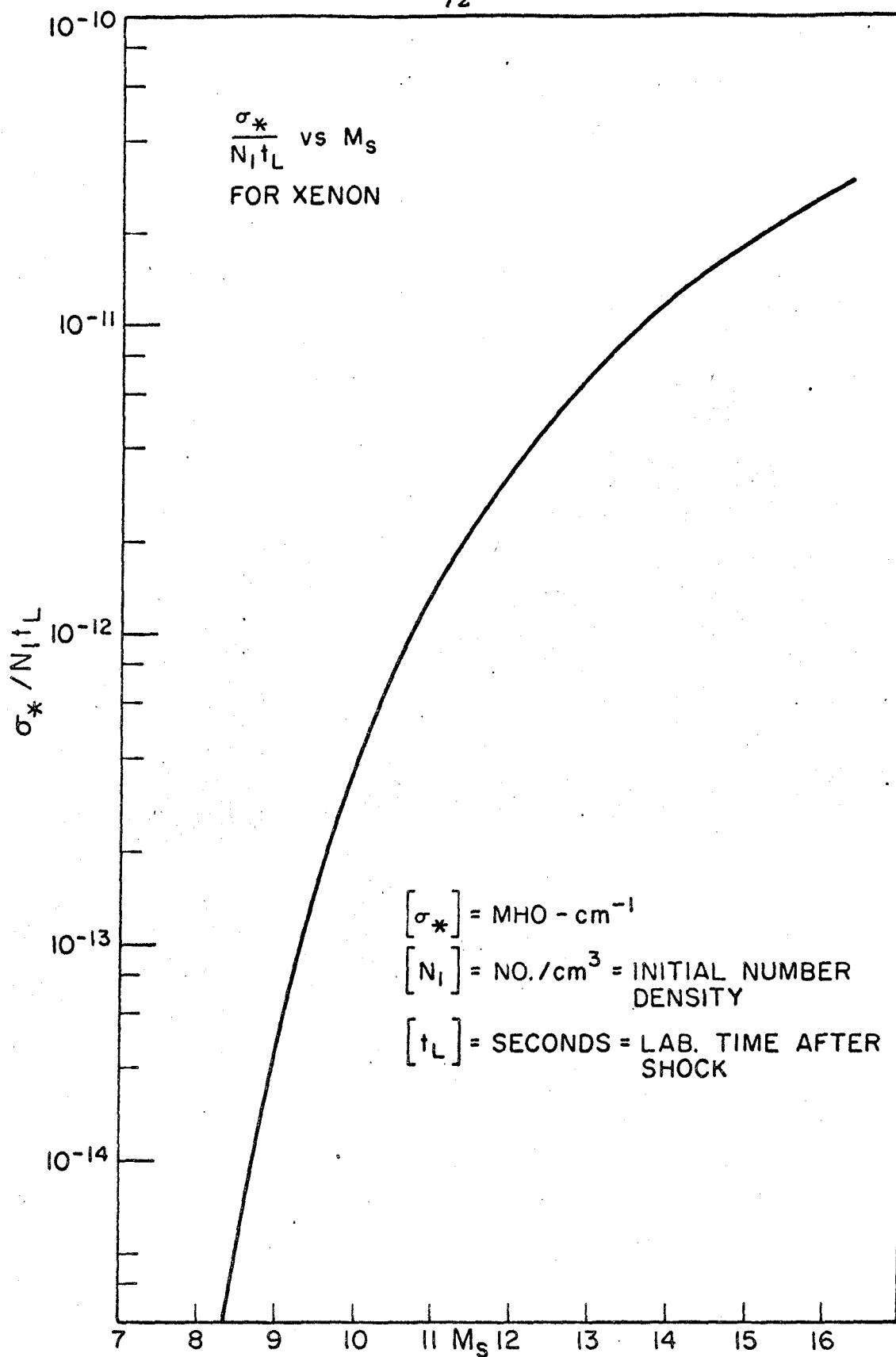


Figure 9. Relaxing gas conductivity  $\sigma_*$  in Xenon.

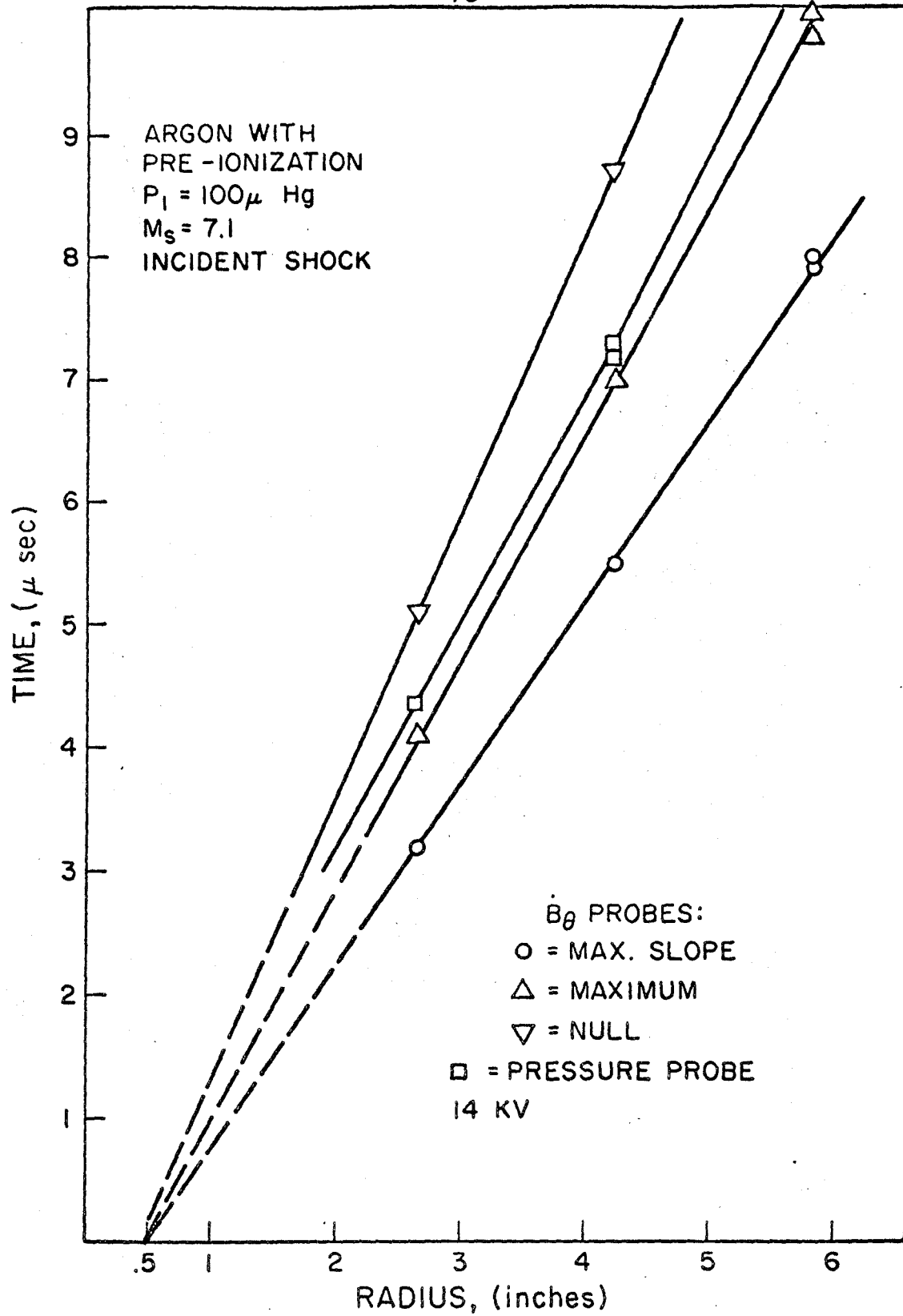


Figure 10. Pre-ionization in Argon behind the incident shock.

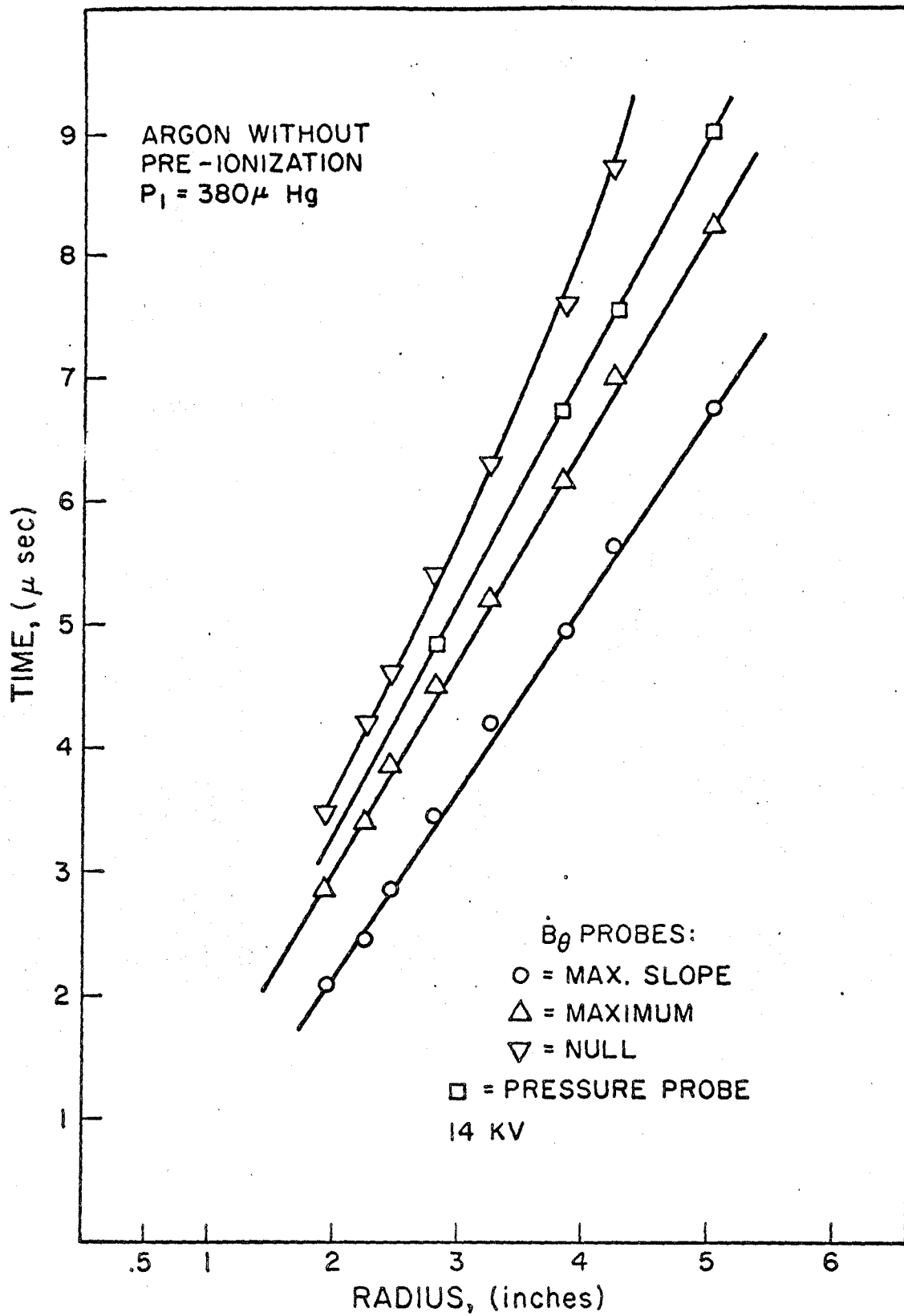


Figure 11. Magnetic and pressure probe data without pre-ionization in Argon.

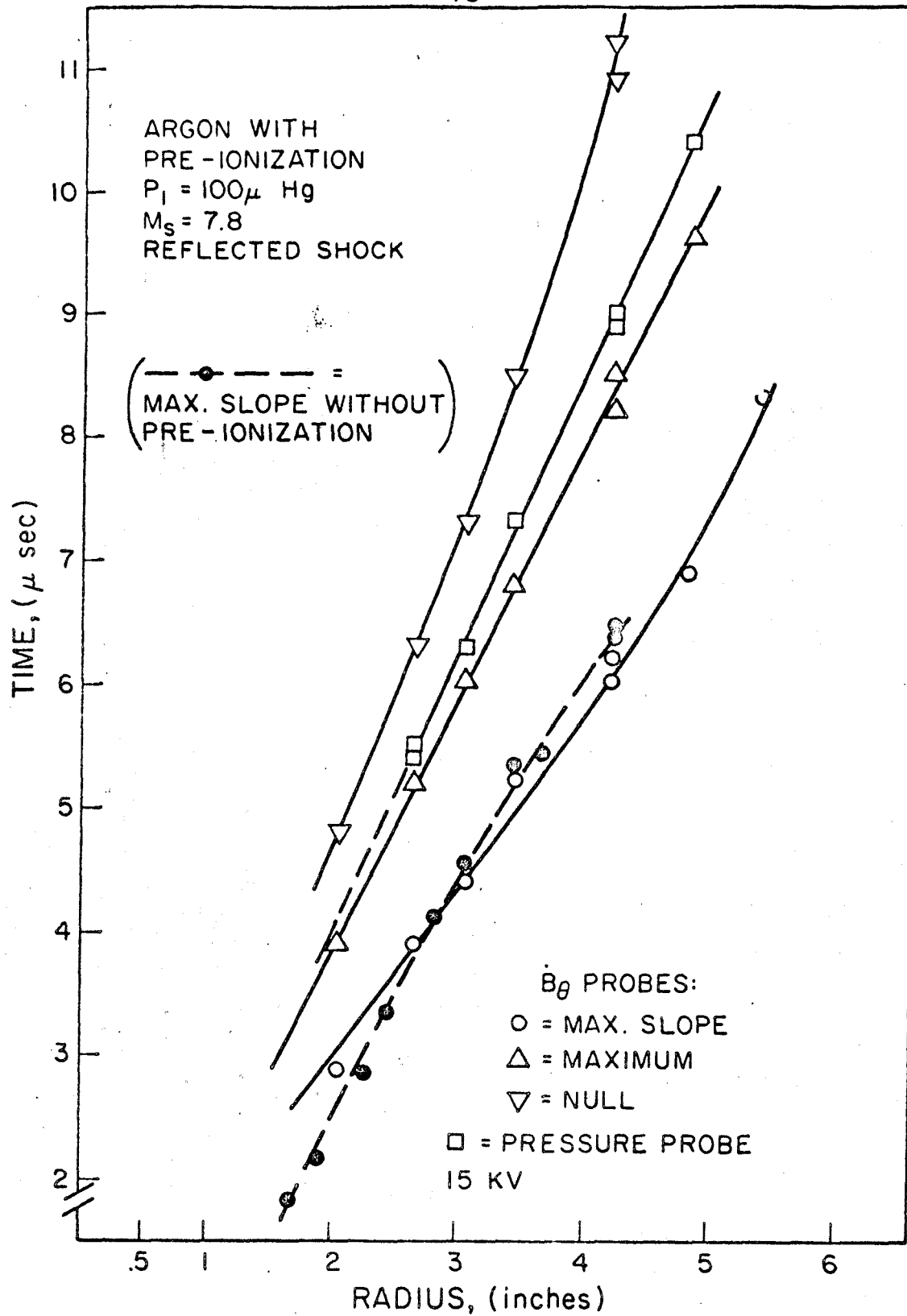


Figure 12. Pre-ionization in Argon behind the reflected shock.

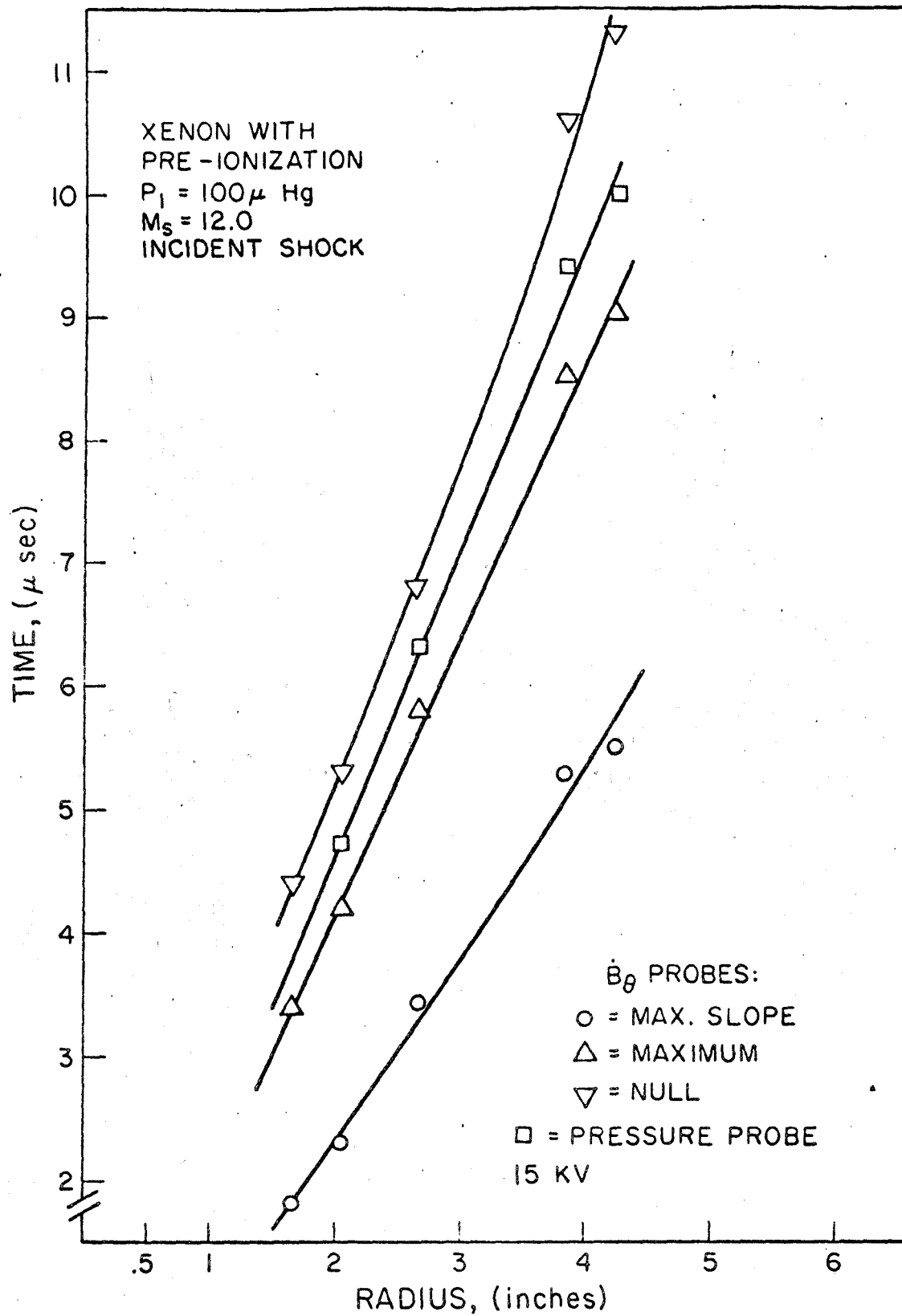


Figure 13. Pre-ionization in Xenon behind the incident shock.

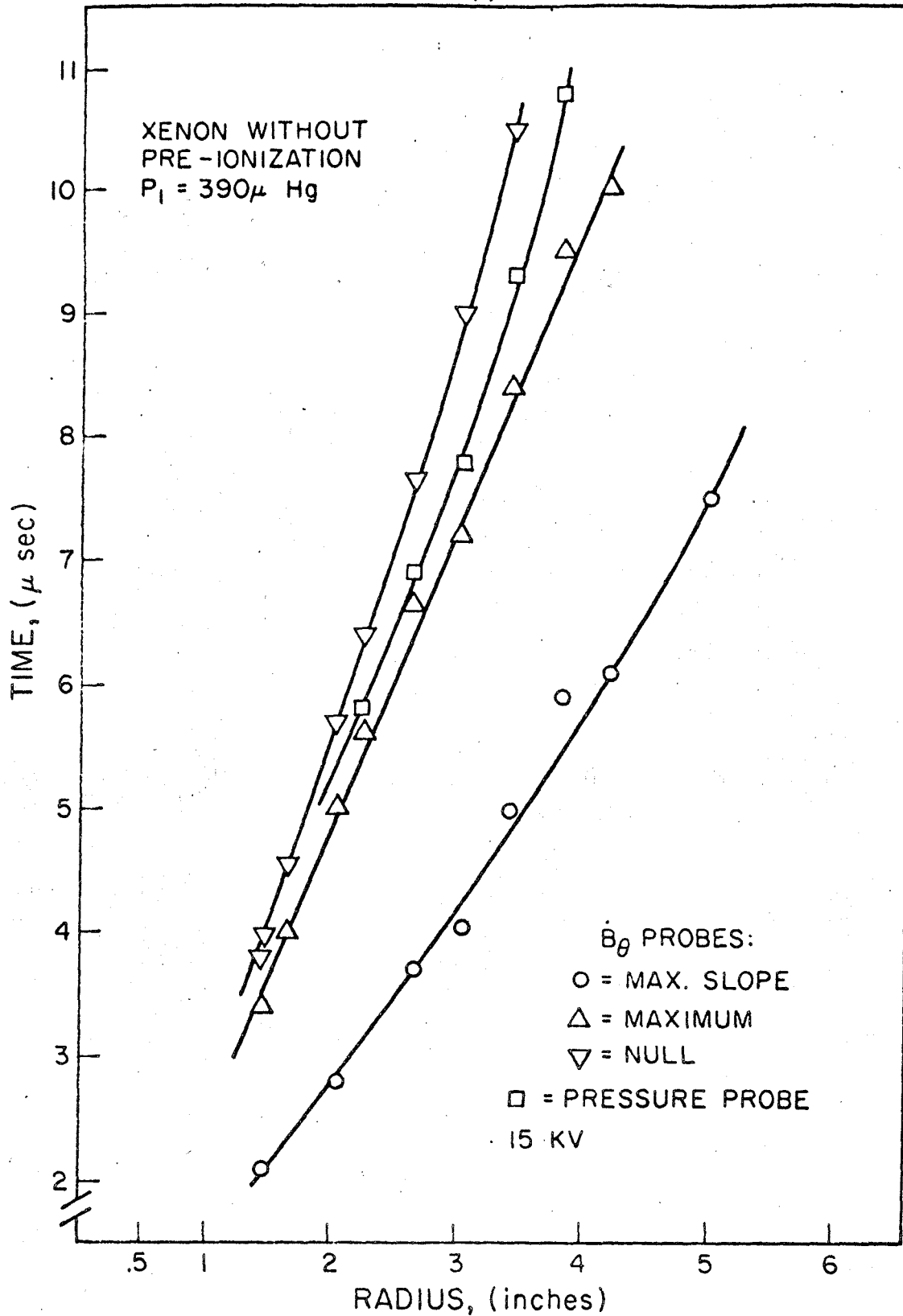


Figure 14. Magnetic and pressure probe data without pre-ionization in Xenon.

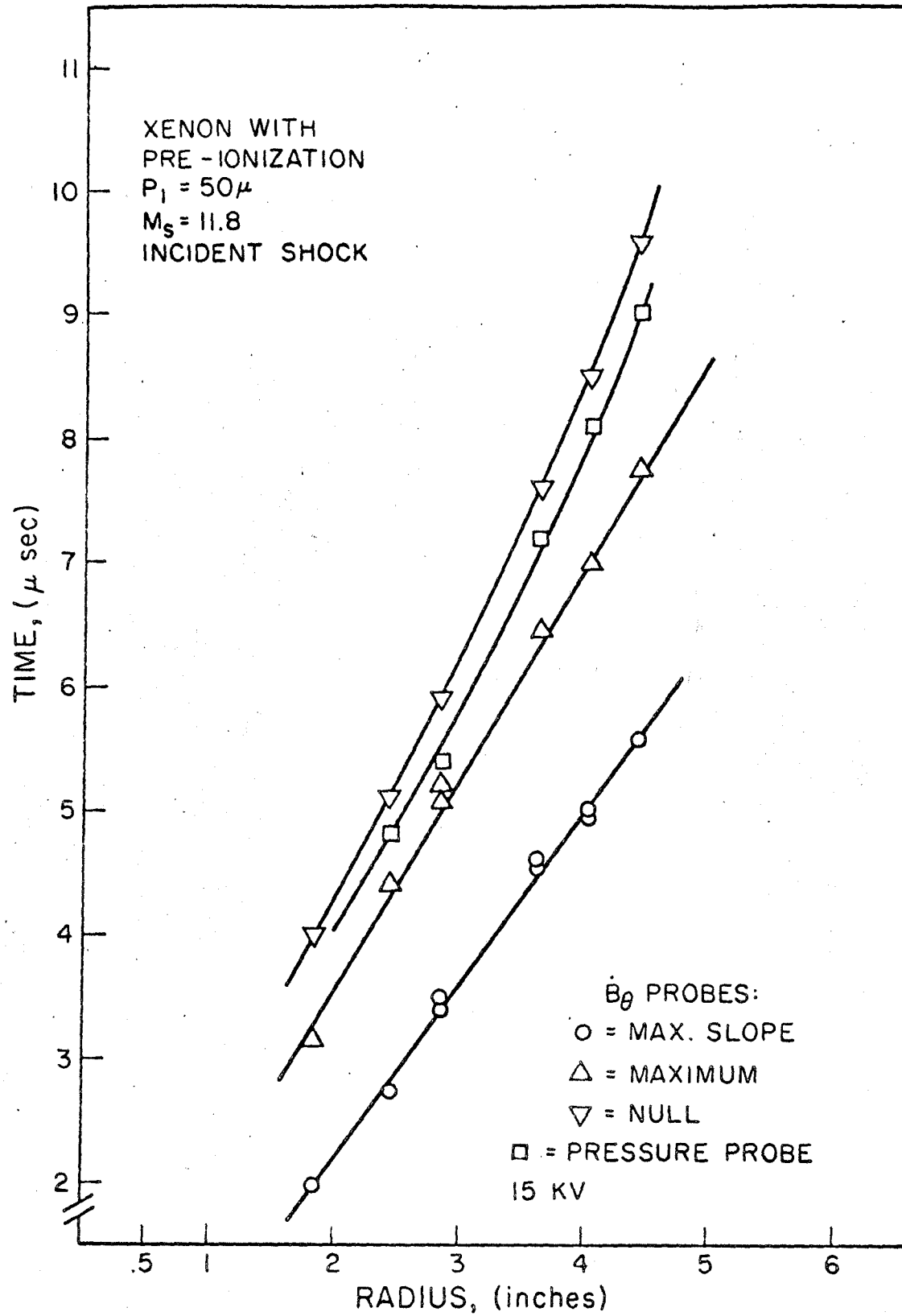


Figure 15. Pre-ionization in Xenon behind the incident shock.

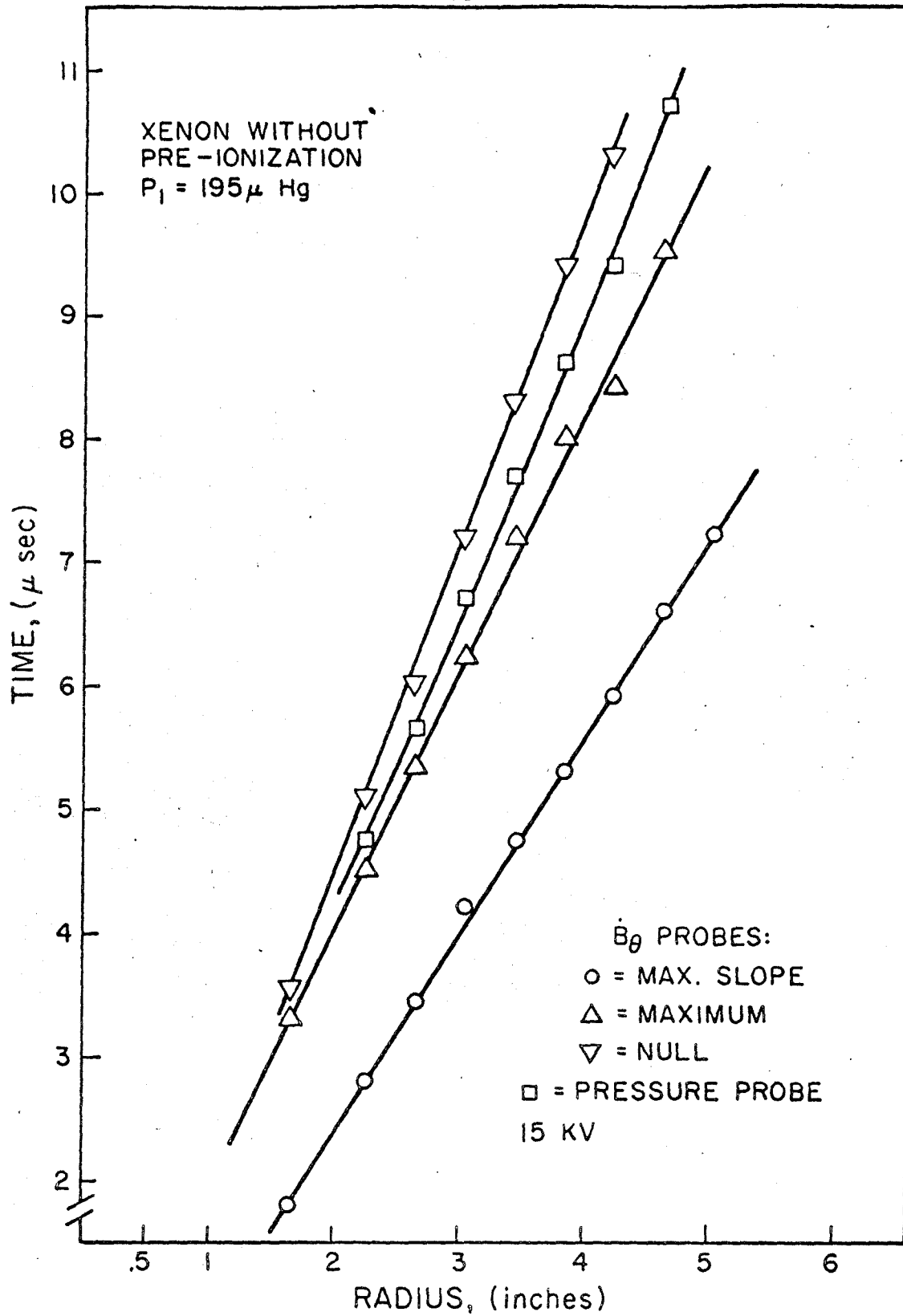


Figure 16. Magnetic and pressure probe data without pre-ionization in Xenon.

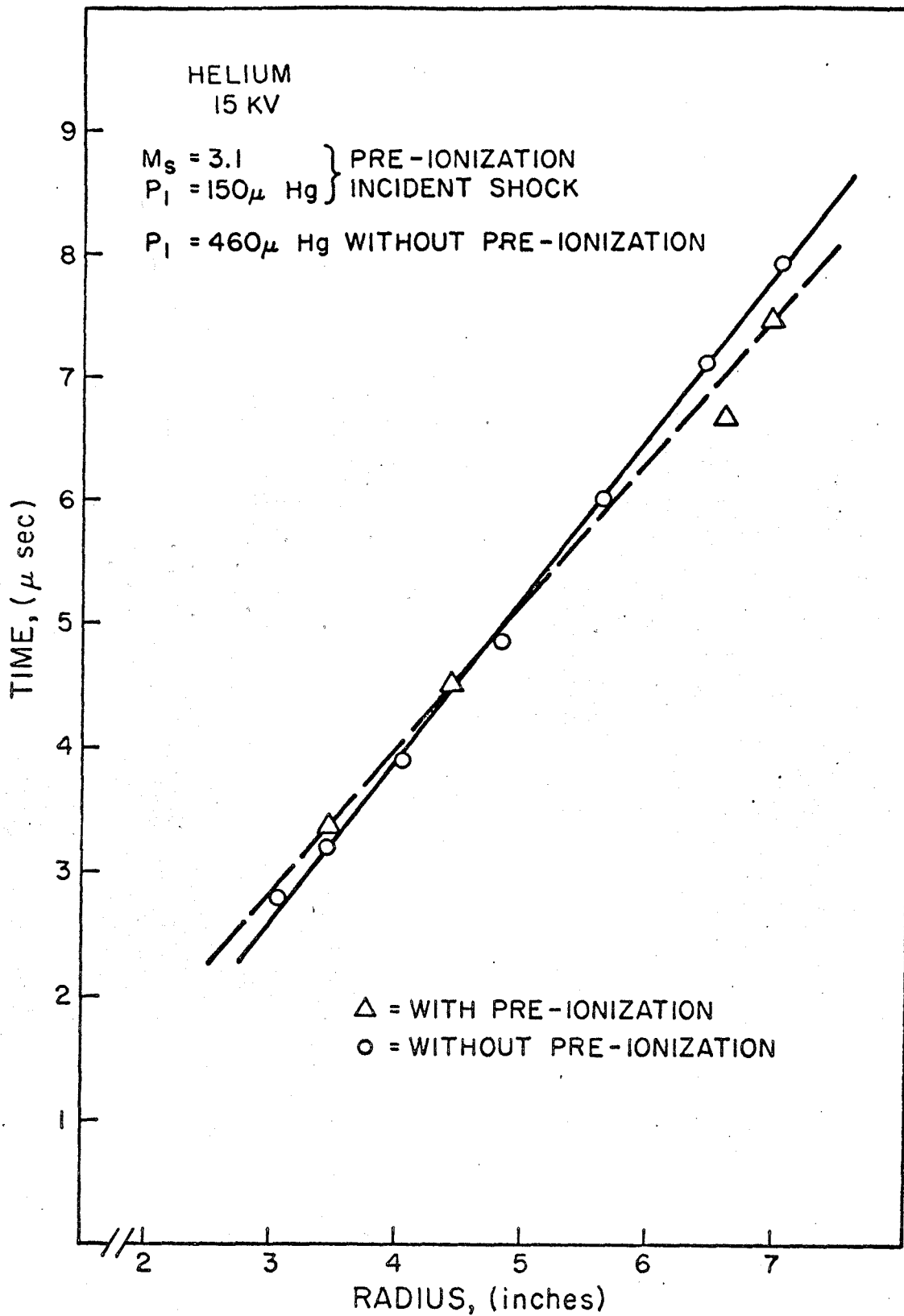
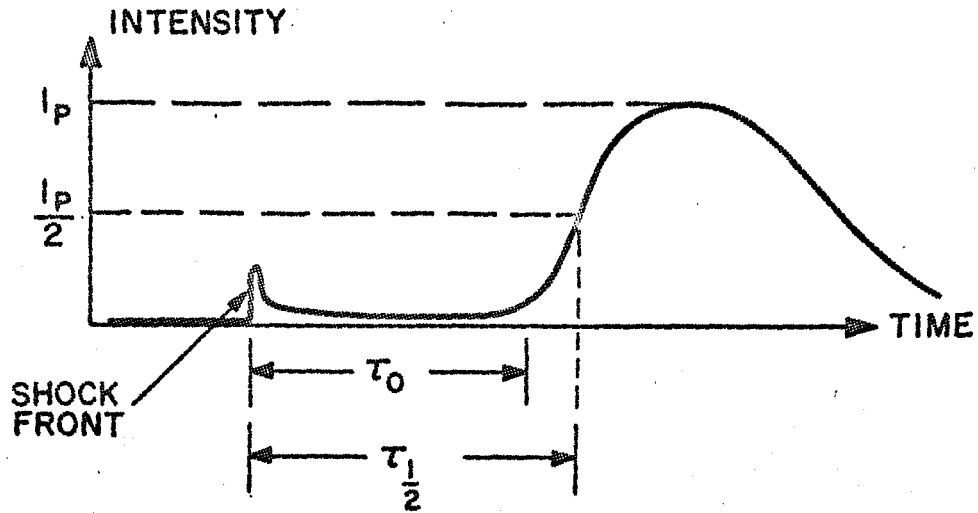
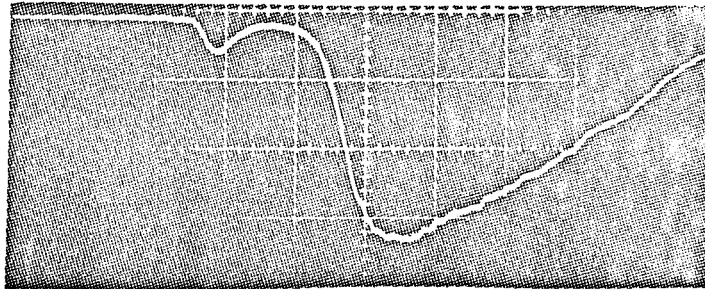


Figure 17. Pressure probe data in Helium with and without pre-ionization.



(a) Relaxation time definitions.



(b) 4945 Å continuum.  $M_s = 15.65$ ,  
 $p_1 = 100 \mu$  Hg of Xenon. Sweep  
 rate  $10 \mu$  sec/cm, left to right.

Figure 18. Relaxation time definitions and typical continuum intensity oscillogram in Xenon.

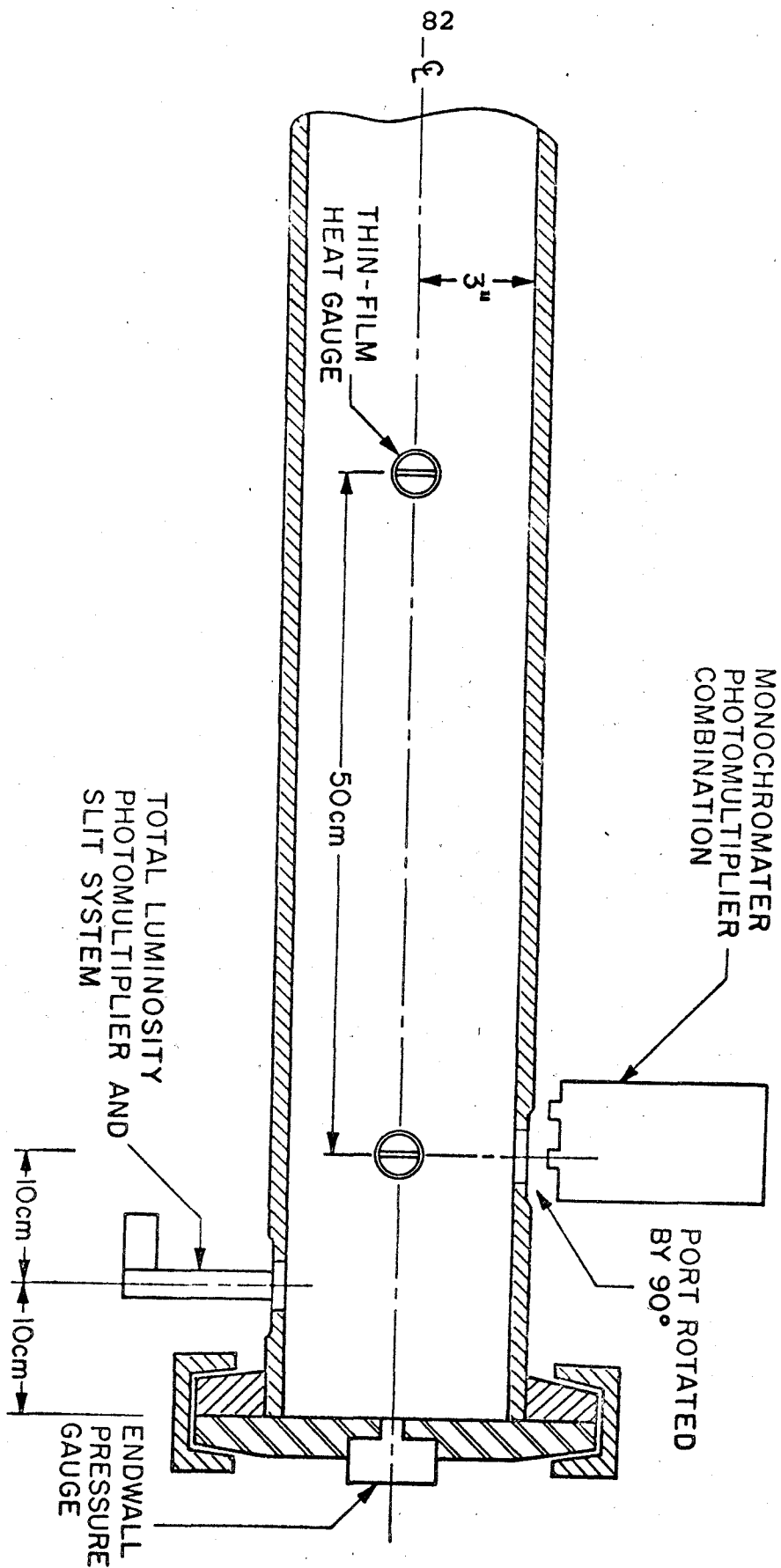


Figure 19. Schematic of 5" shock tube diagnostics.

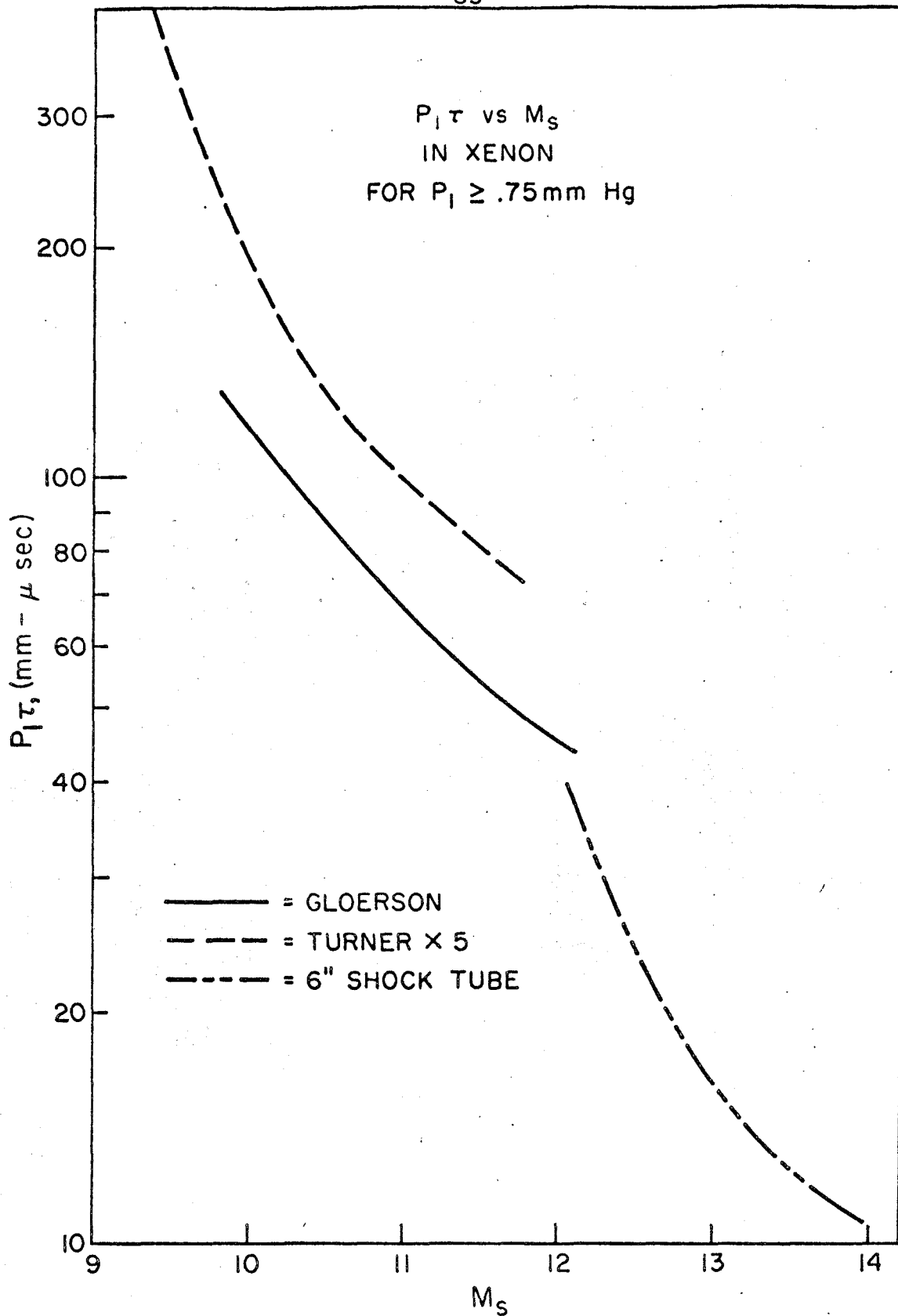
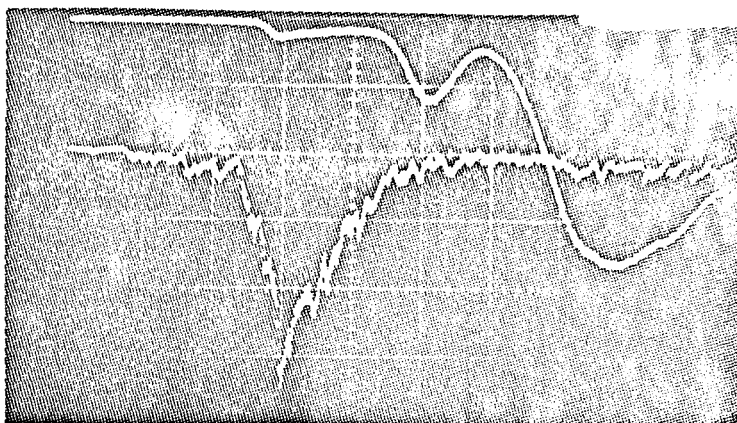
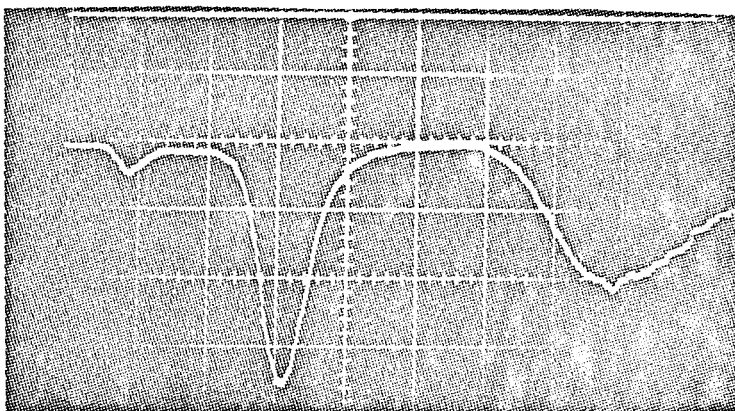


Figure 20. Relaxation times in Xenon at high initial pressures.



- (a) Upper beam: Wavelength-integrated luminosity 10 cm from endwall. Sensitivity 1v/cm.
- Lower beam: XeI 4624 Å line 20 cm from endwall. Sensitivity 20 mv/cm.



- (b) Lower beam: Continuum intensity at 4945 Å, 20 cm from endwall. Sensitivity 0.5 v/cm.

Figure 21. Wavelength-integrated, line, and continuum radiation.  $M_s = 13.6$ ,  $p_1 = 50 \mu$  Hg of Xenon. Sweep rate 20  $\mu$ sec/cm, left to right.

2. THE APPLICATION OF THIN-FILM HEAT TRANSFER  
GAUGES AND FLUSH ELECTROSTATIC PROBES TO  
PARTIALLY IONIZED FLOWS IN SHOCK TUBES

## ABSTRACT

Previous shock tube observations of "spurious" signals in the output of thin-film heat gauges at Mach numbers for which the shocked gas becomes partially ionized are summarized. It is shown that these effects, and those observed in the present experiments in Xenon, cannot be explained in terms of a shorting gauge model. It is demonstrated that the effects are due to the gauge acting more as an electrostatic probe than as a heat gauge. Under these conditions it is shown that the heat gauge provides an accurate measurement of the ionization relaxation time as well as still being useful for determining the shock velocity. The thin-film is also operated as a flush electrostatic probe to measure the ion density in the shock tube wall boundary layer, and the experimental results are in good agreement with the theoretical predictions of two solutions of the boundary layer problem: one based on an approximate solution of the transformed boundary layer equations, and the other based on the solution of the equivalent Couette flow problem. The applicability of these solutions is found to be limited to conditions for which the ionization relaxation time is either very long or very short. Because of the computational simplifications involved it is seen that the Couette flow solution is preferred under most conditions.

## TABLE OF CONTENTS

PART	TITLE	PAGE
	Abstract	i
	Table of Contents	ii
	List of Figures	iv
I.	Introduction	1
II.	Normal Thin-Film Heat Gauge Operation	5
III.	Thin-Film Gauges in Partially Ionized Flows	8
	3.1 Summary of Previous Observations	8
	3.2 Simple Theory for a Shorting Gauge	10
	3.3 Thin-Film Gauges as "Pseudo-Electro- static Probes"	13
IV.	Applications of Probes and "Pseudo-Probes"	19
	4.1 Relaxation Time Measurements	19
	4.2 Shock Velocity Measurements	21
	4.3 Ion Density Measurements	24
V.	Flush Electrostatic Probes	25
	5.1 Flush Probe Theory	26
	5.2 The Ion Density Profile in the Shock Tube Boundary Layer	29
	5.2a Solution of the Boundary Layer Equations	30
	5.2b Couette Flow Solution	37
	5.2c Comparison of the Solutions	40
	5.3 Experimental Results	41

## TABLE OF CONTENTS (cont.)

PART	TITLE	PAGE
VI.	Summary and Conclusions	43
	References	45
	Figures	47

## LIST OF FIGURES

1. Thin-film heat gauge circuitry and output in shock tube boundary layer.
2. Thin-film heat gauge output with no ionization effects.
3. Summary of typical observed gauge outputs.
4. Thin-film heat gauge output for opposite gauge voltages on successive  $M_s = 12.7$  shots into  $25 \mu$  Hg of Xenon.
5. Comparison between heat gauge output and electrostatic probe.
6. Electrostatic probe output with zero bias voltage.
7. Flush electrostatic probe output as a function of bias voltage.
8. Ion density in the boundary layer: theories and experiments.
9. Degree of ionization in the boundary layer.
10. Ion density profiles in Xenon; Couette flow solution.

## I. INTRODUCTION

For the past decade thin-film heat transfer gauges (sometimes called resistance thermometers) have been widely used as a standard shock tube diagnostic tool. They have been used with considerable success to measure transient surface temperatures, to measure shock wave speeds, and to determine the transition from laminar to turbulent flow in boundary layers (see, for example, Refs. 1-3).

With respect to each of the above applications it has universally been noted that at shock Mach numbers high enough to produce even very small degrees of ionization various "spurious" electrical signals appear in the output of the gauges (Refs. 4-6). The spurious signals tend to interfere with the actual signals and have made it difficult to use these gauges in cases where the shocked gas becomes partially ionized. In the heat transfer studies of Marrone and Hartunian (Ref. 5) it was found that by insulating the surface of the gauge with a thin coating of  $\text{SiO}_2$  the undesirable signals could be effectively eliminated for shock Mach numbers up to 14 in Argon. The coating does result in an increase in the rise time of the gauge, which becomes a significant factor when these gauges are used to measure high shock velocities.

The present interest in the problem of the nature of these "spurious" signals was stimulated by the difficulties

encountered while using thin-film gauges to measure the shock velocity in Xenon at Mach numbers of 10 to 20.6 in both the GALCIT 6" and 17" shock tubes (see also Appendix A, section IV of Part 1 of this thesis). Normally the shock velocity is determined by measuring the transit time between two gauges separated by a known distance. The gauges are mounted flush with the sidewall of the shock tube. The gauge outputs are amplified and fed into an electronic counter which records the transit time. Due to the nature of the interfering signals it became extremely difficult to achieve accurate and reproducible triggering of the counter, resulting in errors in the measured shock velocity. Alternatively, the gauge outputs were displayed on an oscilloscope and the transit time was measured from the resulting oscillograms.

By observing the oscillograms of the gauge outputs over the wide range of operating conditions in the relaxation time experiments described in Appendix A of Part 1, it became apparent that among other things the thin-film gauges provided a measurement of the ionization relaxation time. This observation motivated a further study of the nature of the gauge output in the presence of a partially ionized flow.

Normal thin-film gauge operation is reviewed in section II. One of the frequently proposed models considers the gauge as being partially short-circuited by the conducting gas in contact with it. A simple theory for such a "shorting

gauge" is presented in section III and it is seen that this cannot be the dominant effect. It is then shown that when the shocked gas is partially ionized the thin-film gauge behaves more like a "pseudo-electrostatic probe" than as a resistance thermometer. The applications of such a gauge to the measurement of shock velocity, ionization relaxation time, and charged particle number density are discussed in section IV.

In view of the similarities between thin-film gauges and flush electrostatic probes for these conditions, a series of experiments was conducted in which the gauges were operated strictly as flush electrostatic probes. In similar experiments by Bredfeldt, et al. (Refs. 7 and 8), the data from the same type of probe were compared with a theory applicable to a flat plate or steady boundary layer, but not strictly applicable to the non-steady shock tube wall boundary layer. A theory which does apply to the shock tube wall boundary layer is presented in section V. The problem is treated in two ways: first by solving the standard boundary layer equations after making several simplifying assumptions, and secondly by solving the analogous problem in Couette flow. The numerical results of the two solutions are shown to be in good agreement with each other, especially in the part of the boundary layer sampled by the probe. The boundary layer equations require the numerical integration of a nonlinear differential equation whereas the Couette

flow solutions can be computed by hand, representing a significant simplification in the calculation of the theoretical profiles. The experimental data are compared with the theoretical predictions in section 5.3. The measured ion densities also provide a verification of the theoretical values used in the calculation of the electrical conductivity in section 4.2 of Part 1 of this thesis.

## II. NORMAL THIN-FILM HEAT GAUGE OPERATION

The heat gauge consists of a thin metallic film (platinum) evaporated onto a Pyrex plug. The film resistance is typically 150-300 ohms. It is connected in series with a battery and a ballast resistance as indicated in figure 1(a). In the following discussion it will be necessary to refer to both the battery voltage  $V_B$  and the voltage across the film  $V_f$  (also called the gauge voltage). The films are normally approximately  $\frac{1}{16}$ " wide, and  $\frac{5}{8}$ " (6" shock tube) and 1" (17" shock tube) long. They are mounted flush with the shock tube wall with their length perpendicular to the shock tube axis. The gauge responds to the temperature rise of the surface of the glass backing material, associated with the passage of the shock wave, which then can be related to the heat flux from the shocked gas (see Ref. 9). The heating of the glass and film increases the gauge resistance causing the voltage across the gauge to change. It is this change in voltage with respect to the voltage initially across the gauge that is referred to as the "gauge output".

The development of the boundary layer along the shock tube wall is indicated in figure 1(b) in shock-fixed coordinates. Transition from a laminar to a turbulent boundary layer is included in figure 1(b) for completeness, even though for the conditions of the present experiments transition does not occur in the available test times.

The ideal response of a thin-film gauge to the flow situation of figure 1(b) is indicated in figure 1(c). For the laminar boundary layer the gauge output should approximate a simple step function, followed by a signal which increases with time, corresponding to the turbulent boundary layer (Refs. 1, 2, 9, 10).

An example of the approximate step function output of these gauges, corresponding to the laminar case, is presented in figure 2(a) for a  $M_s = 7.8$  shock wave into 100  $\mu$  Hg of Argon. The traces are the outputs of two gauges located 50 cm apart.

Assuming the gauges to be operated at constant current (a good approximation), the gauge output  $\Delta V_f$  is given by

$$\Delta V_f = I_o \Delta R_f \quad (1)$$

where  $I_o$  is the constant circuit current and  $\Delta R_f$  is the change in film resistance.  $\Delta R_f$  is simply related to the change in the film temperature. For the case of a passing shock wave, in which  $\Delta R_f$  is positive,  $\Delta V_f$  has the same sign as  $I_o$ . Consequently the sign of the gauge output is determined by the polarity of the battery used in the gauge circuit. This effect is illustrated by a comparison of figures 2(a) and 2(b). In figure 2(a) both gauges were operated with negative battery voltages, whereas in figure 2(b) the gauge voltage was positive. This is an important property of the gauges and it is discussed further in

section III.

As was mentioned in section I the gauge outputs are normally amplified and fed into a counter. Due to the nature of the amplifiers used in this laboratory it was necessary to operate the gauges with a negative battery voltage. This is in contrast to the experiments of Rabinowicz, et al. (Ref.1), Jahn and Weimer (Ref. 4), Marrone and Hartunian (Ref. 5), Kelly (Ref. 6), and Chabai (Ref. 9). In each of these other experiments the battery voltage was always positive. This factor will also be discussed in section III when the detailed nature of the extraneous signals is considered. For the present experiments a new gauge circuit was constructed, without any amplifiers, making it possible to easily switch from negative to positive gauge voltage, as in figure 2.

### III. THIN-FILM GAUGES IN PARTIALLY IONIZED FLOWS

#### 3.1. Summary of previous observations.

The observations of Jahn and Weimer, Marrone and Hartunian, and Kelly regarding the nature of the spurious gauge output signals in the presence of slight degrees of ionization are summarized in figure 3. Figure 3(a) contains representations of the gauge outputs of Jahn and Weimer behind both incident and reflected shocks in Nitrogen. The sketches in figure 3(b) correspond to the expected and observed gauge outputs in the experiments of Marrone and Hartunian in Air for  $M_s > 7$ . The third sketch in figure 3(b) is also a good representation of the gauge output observed by Kelly for  $M_s \sim 8$  in Argon. For shock Mach numbers on the order of 9, Kelly noted that the magnitude of the negative spike at the shock front was much greater than the positive signal. It is important to realize that the second positive rise in the gauge output of figure 3(a) - (i) is due to the arrival of the reflected shock at the gauge location, whereas in figure 3(b) - (i) the second positive rise is due to the transition from laminar to turbulent flow in the boundary layer.

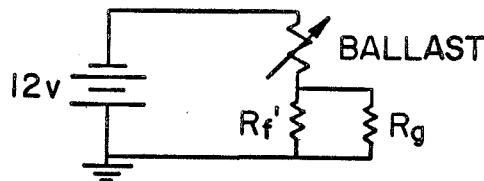
In both references 4 and 5 the anomalous behavior of the gauge outputs is attributed to short-circuiting of the gauge current through the parallel electrical path provided by the conducting gas. Marrone and Hartunian were able to

eliminate the extraneous signals by insulating the gauge surface with a thin coating of  $\text{SiO}_2$ . They were then able to successfully measure the wall temperature rise up to Mach 14 in Argon. The success of the insulation eliminates the possibility that the extraneous signals are electromagnetically induced rather than due to conduction effects. Jahn and Weimer were led to the same conclusion when they coated their gauge with Scotch Tape and obtained completely clean traces.

### 3.2. Simple theory for a shorting gauge.

In equation (1),  $\Delta V_f = I_o \Delta R_f$  was the gauge output proportional to  $\Delta R_f$ , the change in resistance of the film due to the heating of the shock tube wall by the shocked gas. Now consider the gauge output  $\Delta V_g$  which would result from the conducting gas providing a parallel electrical path for the current.

Immediately behind the shock front two things happen: the film resistance jumps to the value  $R_f' = R_f + \Delta R_f$  due to the normal heating effect, and the shocked gas offers a parallel resistance  $R_g$  to the current in the gauge circuit. The equivalent circuit corresponding to this situation is sketched below:



With good accuracy it can be assumed that  $R_f' \ll R_g$ . This approximation is verified by the observed magnitude of the gauge output as compared with the initial voltage across the gauge. If  $\Delta R_g$  is the change in gauge resistance due to the presence of the conducting gas, then

$$\Delta V_g = I_o \Delta R_g = I_o \left( \frac{R_f' R_g}{R_f' + R_g} - R_f' \right), \quad (2)$$

where  $\Delta V_g$  is measured with respect to  $\Delta V_f$ .

With  $R_f' \ll R_g$ ,

$$\Delta V_g \approx I_o \left[ R_f' \left( 1 - \frac{R_f'}{R_g} + \dots \right) - R_f' \right] \cdot (3)$$

Therefore

$$\Delta V_g \approx - \frac{I_o (R_f')^2}{R_g} \quad (4)$$

It is apparent from equation (4) that for a shorting gauge the magnitude of the gauge output will be directly proportional to  $I_o$  and to the square of  $R_f'$  (roughly the square of  $R_f$  also). Therefore, if two gauges are operated at the same  $I_o$  but with  $R_f$  differing by a factor of two, the gauge outputs due to shorting should differ by a factor of four. Also, whereas the gauge output has the same polarity as  $I_o$  for the case of  $\Delta V_f$ , for  $\Delta V_g$  the gauge output has the opposite polarity.

The parallel resistance of the gas  $R_g$  can be rewritten in the terms of the electrical conductivity  $\sigma$ . If the current path in the gas has length  $L$  and cross-sectional area  $A$ , then

$$R_g = \int_0^L \frac{dl}{\sigma A} \cdot \quad (5)$$

The gas in contact with the gauge is within the wall boundary layer so the density, temperature, and degree of ionization are all different than the corresponding value

outside the boundary layer. Any theoretical calculation of  $R_g$  is therefore complicated by the necessity of relating the conductivity of the gas outside the boundary layer to the conductivity of the gas actually providing the shorting path for the current.

### 3.3. Thin-film gauges as "pseudo-electrostatic probes".

Each of the points discussed in section 3.2 concerning how a shorting gauge would behave plays a role in demonstrating that shorting of the gauge cannot be the predominant effect regulating the nature of the gauge output in the presence of a partially ionized gas. It will be shown that the gauge acts as a "pseudo-electrostatic probe" with the heat transfer signal actually becoming negligible compared to the probe signal at the higher Mach numbers.

In figure 2 it was demonstrated that at Mach numbers of 7-8 in Argon the gauge output was as expected; approximately a step function that reversed itself when the battery polarity was reversed. The same comparison is made in figures 4(a) and 4(b) for two successive runs at  $M_s = 12.7$  at an initial pressure of  $25 \mu$  Hg of Xenon. Not only doesn't the gauge output reverse itself in going from negative to positive battery polarity, but in addition the gauge output is amplified considerably. However, the qualitative structure of the profiles are the same, with distinct changes in the slope of the profiles occurring at the same time after passage of the shock wave in both cases. This behavior is not reconcilable with the shorting gauge model of section 3.2.

It should further be noted that in the case of Argon at  $M_s$  7-8 the signal at the shock front was on the order of

5-7 mv, whereas in the case of Xenon at Mach 12.7 the jump at the shock front was approximately 50 mv with negative polarity and at least 500 mv with positive battery polarity. The magnitude of these jumps right at the shock front is greater than can be accounted for on the basis of the wall temperature rise alone, and from the viewpoint of wall temperature rise there is of course no reason for there to be any difference between the magnitude of the gauge output for negative and positive polarities, while the measured difference is more than an order of magnitude.

If the ground side of the thin-film gauge is disconnected at point (a) in figure 1(a), all of the battery voltage appears across the gauge and  $I_o = 0$ , and the heat gauge is converted into an electrostatic probe flush with the shock tube wall (flush electrostatic probe). By using different batteries the probe may be biased at different voltages, either positive or negative. Figure 5(b) is an oscillogram obtained in this manner, with a positive bias of 6.5 volts on the probe. Figure 5(a) is the output of the thin-film gauge operated with a positive voltage of 6.5 volts across the film ( $M_s = 12.7$ ,  $p_1 = 25 \mu$  Hg of Xenon). The profiles of both traces are the same, with the probe output substantially greater in magnitude than the gauge output. This is again in disagreement with the shorting gauge model since using the thin-film gauge as an electrostatic probe at the same voltage is equivalent to letting

$I_o \rightarrow 0$  in equation (4) which should result in  $\Delta V_g = 0$ . Instead, a larger signal is obtained with the same time profile.

At this point it could be argued that in figure 5(b) the observed signal is a result of the conducting gas providing a path to ground in parallel with the open-circuited film and causing the voltage across the probe to change. This may be discounted in view of figure 6 which is an oscillogram obtained under the same shock tube conditions ( $M_s = 12.7$  into  $25 \mu$  Hg of Xenon) as figure 5(b) but with zero bias voltage. Since there is no battery in the circuit the signal cannot be caused by the conducting gas partially shorting the probe.

In view of the above discussion and figures 4-6 it is concluded that in the presence of a partially ionized gas the thin-film heat gauge acts predominantly as an electrostatic probe in which current is being drawn from the gas into the external circuit, rather than as a shorting gauge in which the current flows from the external circuit into the gas. At the Mach numbers and pressures of the present experiments the heat gauge signal of 10-20 mv is effectively masked by the much larger signals due to the electrostatic probe effects.

This change in perspective makes it possible to account for many of the details of the "spurious" signals observed in the previous experiments, as well as those of the present

work. Many of these details are simply related to the polarity of the gauge voltage, a point which was introduced earlier.

When an electrostatic probe has a positive bias it will attract electrons and repel ions and conversely, a negatively biased electrostatic probe will attract all ions and repel most electrons. With the heat gauge used in a circuit such as that in figure 1(a) the top of the film will be at say 6.5 volts positive, with the potential decreasing linearly to ground at the bottom of the gauge. Thus the film is really a superposition of electrostatic probes at all potentials between the gauge voltage and ground; hence the terminology "pseudo-electrostatic probe". On the other hand, when the film is used strictly as a flush electrostatic probe by disconnecting the ground side of the film, the whole surface area of the film is at the bias voltage (say 6.5 volts positive). For this reason the probe should be a more effective collector of electrons than the heat gauge at the same voltage, as was observed in figure 5. It was noted in section II that in each of the previous experiments the gauge voltage was positive. Acting as probes these gauges will attract electrons, and the part of the resulting gauge output that is due to the probe effect should be negative. This was seen to be the case in each of the earlier experiments (see figure 3 and section 3.1).

In the experiments of Kelly, and Marrone and Hartunian,

the negative spike was observed to coincide with the arrival time of the incident shock front. It has been noted by most experimentors that there is a short burst of luminosity at the shock front for shock Mach numbers greater than  $\sim 7-9$  in most gases. In the present Xenon experiments it was noted that this burst of radiation was at least in part continuum radiation, indicating there are some free electrons at the shock front (see Appendix A, Part 1). The burst of radiation dies out quickly and with a positive gauge voltage a correspondingly short spike of negative signal would be expected to appear in the gauge output as the shock Mach number is increased. This was observed by Kelly in Argon for  $M_s > 8$  and by Marrone and Hartunian in Air at similar Mach numbers. It is reasonable to expect that the origin of these free electrons at the shock front is impurity-related in some manner. Therefore the Mach number and pressure at which these effects first appear will vary from one shock tube to another.

Jahn and Weimer did not observe a negative spike at the shock front in their Nitrogen experiments (see figure 3(a)). This is reasonable in view of the comparatively low shock Mach numbers. The onset of the negative signal coincides with the passage of the reflected shock, indicating enough ionization behind the reflected shock for the probe effects to become important. It is seen in

figure 3(a) that at roughly the same Mach number (5.5-6.5), the "probe" effect is proportional to the initial pressure, with the largest signal observed at  $p_1 = 6$  mm. The negative signal is somewhat smaller for  $p_1 = 3$  mm, and it disappears entirely for  $p_1 = 2$  mm. This is in qualitative agreement with the present model since at a constant Mach number the higher initial pressure results in a higher electron density behind the reflected shock.

It was noted earlier that in figure 4 the heat gauge output at the shock front was an order of magnitude larger with a positive gauge voltage of 6.5 volts than with the same voltage negative. With a negative gauge voltage most electrons are retarded and ions are attracted to the "pseudo-probe". However, because of their much greater mobility, enough energetic electrons reach the gauge that the net current is an electron current. On the other hand, when the gauge has a positive voltage electrons are attracted and ions repelled, and coupled with the effect of the greater electron mobility a very large negative signal results. This point is discussed farther in section 4.2.

#### IV. APPLICATIONS OF PROBES AND "PSEUDO-PROBES"

It was unanimously concluded in references 4, 5, and 6 that the effects discussed in section III were undesirable and greatly reduced the usefulness of the thin-film heat gauge as a diagnostic tool in partially ionized flows. With respect to its use as a resistance thermometer this is certainly true. As the shock Mach number is increased the heat flux signals become negligible compared with the signals due to the probe effects. However, this deficiency is far overshadowed by the additional utility of the gauge that is derived from an understanding of the nature of the probe effects.

##### 4.1. Relaxation time measurements.

In conjunction with the relaxation time measurements described in Appendix A of Part 1, it was observed that at precisely the relaxation time  $\tau_0$  (as defined in figure 18, Part 1) the heat gauge output undergoes a sharp increase in slope. This corresponds to the transition from atom-atom to electron-atom ionization, with the associated rapid increase in the electron generation rate. The values of  $\tau_0$  obtained from the heat gauges were compared with those values obtained from the continuum intensity measurements, at Mach numbers ranging from 10.5 to 20.6 and initial pressures of .05 to 1.5 mm Hg of Xenon. Over this spectrum of operating conditions  $\tau_0$  varies from approximately 5 to

130  $\mu$  sec, and the difference between the spectroscopic values of  $\tau_0$  and those obtained from the heat gauges was less than 5% over the entire range.

The same qualitative behavior results when the film is used as a biased electrostatic probe, as would be expected in view of the discussion in section III. Therefore, when the film is used either as a heat gauge or an electrostatic probe, in a partially ionized flow the outputs provide an accurate measurement of the ionization relaxation time  $\tau_0$ .

#### 4.2. Shock velocity measurements.

Figure 6 shows an oscillogram of the output of the thin-film used as an electrostatic probe with zero bias battery voltage. The probe output of .5 to 1 volt is essentially the same as that obtained when the standard heat gauge is connected directly to the oscilloscope, with no battery or amplifiers in the circuit. This large output signal is rather mysterious from the viewpoint of a shorting gauge, but is quite reasonable when the heat gauge is considered as a probe since the potential that matters is the probe potential with respect to the plasma rather than with respect to the shock tube. The plasma potential is the potential at which there are no electric fields between the probe and the plasma, and the charged particles migrate to the probe due to their thermal velocity. Because of their higher thermal velocity more electrons reach the probe than ions, so the probe may be regarded as being surrounded by a sheath in which electrons predominate. A positive potential must be applied to the probe to reduce the potential difference across the sheath to zero. Since the plasma potential is positive the probe or heat gauge with no battery is still biased negatively with respect to the plasma potential and there should be an output signal.

The gauge output with no bias battery has been observed by others (see, for example, Ref. 6), but no

attempt was made to utilize the output. The signals are large enough that without any amplification they can be used to trigger the electronic counter and/or oscilloscopes, making it very simple to accurately measure the shock velocity at high Mach numbers. Further, because no amplifiers or batteries are used the gauge is a completely passive circuit element, with practically no design, construction, or maintenance problems. Another fringe benefit has resulted because with the high gain amplifiers normally used the heat gauge circuits were extremely sensitive to the electrical noise generated by other experiments in the laboratory. This used to be an annoying difficulty with the 17" shock tube in particular, resulting in premature triggering of the oscilloscopes, counter, and the inverse pinch.

Even though the probe or gauge with no battery is in effect biased negatively with respect to the plasma potential it is seen in figure 6 that the output signal at the shock front is negative, indicating a net electron current. This is because of the larger mobility of the electrons compared with that of the ions, so that even with a slightly retarding potential more electrons than ions reach the probe. As the electron retarding potential is increased by making the probe more and more negative, fewer and fewer electrons can reach the probe and eventually the negative spike at the shock front should be eliminated.

This effect is demonstrated in figure 7 in which oscillograms are presented for successive shots at Mach 12.7 into 25  $\mu$  Hg of Xenon with the same probe more and more negatively biased. At 6.5 volts negative battery voltage the spike is somewhat rounded off, and at 12 volts it has disappeared completely.

As the Mach number is increased and hence the plasma potential, it would be expected from the above that the negative spike would be replaced by a positive spike, reflecting a net ion current. This is because as the plasma potential is increased the probe or gauge at zero battery voltage actually becomes more and more negative with respect to the plasma. This effect had already been observed in the normal heat gauge outputs in Xenon at  $M_s \sim 18-20$  in the 6" shock tube, and recently Smith (Ref. 11) has observed the same effect using electrostatic probes with zero battery voltage. At Mach numbers on the order of 18 the signal at the shock front is positive, whereas at Mach numbers of 12-14 it is negative. In terms of the shock velocity measurement either the positive or negative signal can be used, and the magnitude of the signal can be increased by operating with some non-zero bias battery voltage. Therefore, the cross-over in the polarity of the output signal at the shock front doesn't really limit the use of the gauge for shock velocity measurements, and this behavior further confirms the "pseudo-probe" nature

of the output.

#### 4.3. Ion density measurements.

When the thin-film gauges are used as biased flush electrostatic probes, still another important application emerges. The probes can be used to measure the ion number density in the shocked gas. This could also be done with the films operated as heat gauges, but the analysis in that case is complicated by having to determine what the effective bias voltage is. For this reason it is somewhat simpler to use the films strictly as probes for the ion density measurements. The use of the thin-film gauges to measure the ion density is treated in detail in section V.

Since the conversion from heat gauge to electrostatic probe only requires slight changes in the external circuit, which are readily accomplished in the normal time between runs, the same films can be used to perform all of the measurements discussed in this section: the ionization relaxation time, the shock velocity, and the ion number density. Therefore, rather than becoming less useful as a diagnostic tool, the thin-film gauge has become more versatile and more widely applicable at Mach numbers for which the shocked gas becomes partially ionized.

## V. FLUSH ELECTROSTATIC PROBES

This section deals with the use of a thin-film gauge strictly as a flush electrostatic probe, biased strongly negative to collect ion saturation current. The decision to use the ion rather than the electron saturation current was based on the experience of Bredfeldt, et al. (Ref. 7), who found that using the ion current resulted in a more accurate measurement. This is believed to be due to the fact that at the large positive probe potentials required for the collection of electron saturation current the electrons are accelerated to such an extent that they can ionize some of the neutrals, and such secondary ionization is neglected in the theory.

The flush probe samples the flow within the wall boundary layer of the shock tube, in which the mean free path is less than the sheath thickness, rendering "classical" probe theory inapplicable. Two questions then arise: what current will the probe measure for a given bias voltage, and how is this current related to the ion density in the main flow outside the boundary layer? The first of these questions is considered in section 5.1 and the second in section 5.2.

### 5.1. Flush probe theory.

A one-dimensional theory for the current-voltage characteristic of a flush electrostatic probe in a collision-dominated flow has been developed by Bredfeldt, et al. in reference 7, and is summarized here. The probe is assumed large enough that the probe and sheath areas are approximately equal. The probe current is considered to be collected from a plane distance  $d_s$  above the probe surface. If all the ions crossing the plane are eventually collected by the probe, the current will be

$$I_+ = \frac{An_{+s}e\bar{v}_+}{4} \quad (6)$$

$n_{+s}$  is the ion density at the sheath edge and  $\bar{v}_+$  is the corresponding thermal velocity;  $A$  is the probe area, and  $e$  is the electronic charge. Equation (6) is applicable assuming there is no ionization or recombination inside the sheath (the wall is infinitely catalytic).

The next step is to determine the sheath thickness  $d_s$ . This is accomplished by solving the one-dimensional Poisson's equation for the potential, where the ion drift velocity is assumed determined by their mobility and the applied electric field. This is in contrast to the collisionless case in which the ion drift velocity is calculated by equating the change in kinetic energy of the ions to the applied potential difference. The result is

(see Ref. 12)

$$I_+ = \frac{9.95 \times 10^{-14} \mu_+ V^2 A}{d_s^3} \text{ amps} \quad (7)$$

A is the probe area in  $\text{cm}^2$ ,  $\mu_+$  is the ion mobility in esu,  $d_s$  is the sheath thickness in cm, and V is the potential across the sheath in volts.

In the derivation of equation (7) the mobility is assumed constant across the sheath. However, in the boundary layer the mobility decreases towards the probe surface. Bredfeldt, et al. have treated the case of variable  $\mu_+$  and have concluded that in light of the accuracy of the other approximations it is consistent to use the value of the mobility at the sheath edge.

The ion mobility is given by

$$\mu_+ = \frac{e\tau_+}{m_+} \quad (8)$$

in which  $m_+$ , and  $\tau_+$  are the ion, mass, and collision time, respectively.

Now it is possible to determine  $d_s$  in terms of the measured current, the applied potential relative to the plasma, and the ion mobility. The solution of equation (7) involves an iteration procedure since the values of  $\mu_+$  and V depend on plasma parameters at the sheath edge, the location of which is being calculated.

A significant difference between the above results and those of the classical collisionless probe theory is that in the present case the sheath thickness depends upon the magnitude of the applied potential. This makes it possible to sample different parts of the boundary layer by varying the bias voltage on the probe.

Throughout the calculation of the current-voltage response of the probe the effect of the axial mass motion of the shocked gas was neglected. If electrons were being collected by the probe this effect would be unquestionably negligible because of the very high mobility of the electrons. However, when ions are collected the effect of the axial gas velocity is not obviously negligible. The convection velocity is just the gas velocity behind the shock wave,  $U_p$ , which is roughly 75% of the shock velocity, at the edge of the boundary layer. The axial velocity decreases rapidly to zero across the boundary layer. On the other hand the drift velocity of the ions in the probe sheath is given by the product of the electric field and the ion mobility:

$$\bar{v}_d = \mu_+ E = \frac{e\tau_+}{m_+} \frac{V}{d_s} .$$

$\bar{v}_d$  has been calculated for the conditions of the present experiments, and at the outer edge of the boundary layer  $\bar{v}_d$  is of the same order as  $U_p$  ( $10^5$ - $10^6$  cm/sec). However,

while the gas velocity decreases to zero across the boundary layer,  $\bar{v}_d$  decreases by less than an order of magnitude. It is therefore concluded that the convective effect may be neglected in the present experiments.

#### 5.2. The ion density profile in the shock tube boundary layer.

To relate the ion density measured at the edge of the sheath to that in the external flow it is necessary to calculate the ion density profile through the boundary layer. Figure 1(b) shows that in steady, or shock-fixed coordinates the boundary condition at the wall is that the wall velocity equals the shock velocity. This is in contrast to the case of the flat plate, or steady boundary layer in which the wall velocity is zero. Since the boundary layer equations are nonlinear this is a non-trivial difference between the two problems. In references 7 and 8 the measured ion densities were compared to theoretical profiles calculated for the flat plate case. In this section the ion density profile is calculated for the shock tube boundary layer case.

## 5.2a. Solution of the boundary layer equations.

Making the standard assumptions concerning the boundary layer thickness, with  $(x, y)$  the directions parallel and perpendicular to the shock tube wall, and  $(u, v)$  the corresponding velocity components, the conservation equation for the  $i^{\text{th}}$  species of an ionizing gas may be written (Ref. 13)

$$\rho u \frac{\partial c_i}{\partial x} + \rho v \frac{\partial c_i}{\partial y} = \frac{\partial}{\partial y} (\rho D_{12} \frac{\partial c_i}{\partial y}) + w_i . \quad (9)$$

$c_i$  is the mass fraction of the  $i^{\text{th}}$  species, equal to  $\rho_i/\rho$ , where  $\rho$  is the density.  $D_{12}$  is the appropriate binary diffusion coefficient, and the first term on the right-hand side of equation (9) represents the diffusion due to a concentration gradient in the  $i^{\text{th}}$  species (for ions, with only a slight degree of ionization,  $D_{12}$  is the ion-neutral diffusion coefficient).  $w_i$  is the mass rate of formation of the  $i^{\text{th}}$  species per unit volume and time. It is assumed in equation (9) that the thermal diffusion gradient is small compared with the specie concentration gradient.

The x-component of the momentum equation is

$$\rho u \frac{\partial u}{\partial x} + \rho v \frac{\partial u}{\partial y} = - \frac{\partial p}{\partial x} + \frac{\partial}{\partial y} (\mu \frac{\partial u}{\partial y}) , \quad (10)$$

where  $\mu$  is the coefficient of viscosity.

Solutions of these nonlinear partial differential equations are generally obtained by first reducing them

to a set of ordinary differential equations, if this can be done. As a first step in that program the equations are normally transformed from  $(x, y)$  coordinates to  $(\xi, \eta)$ , or boundary layer coordinates. This is done in reference 13 with the result that the transformed species conservation equation becomes (for the ions)

$$\begin{aligned} \frac{\partial}{\partial \eta} \left( \frac{NLe}{Pr} \frac{\partial z_+}{\partial \eta} \right) + f \frac{\partial z_+}{\partial \eta} - 2z_+ \frac{\partial f}{\partial \eta} \frac{d \ln c_{+\delta}}{d \ln \xi} + \frac{2\xi}{\rho u_\delta} \frac{dx}{d\xi} \frac{w_i}{c_{+\delta}} \\ = 2\xi \left( \frac{\partial f}{\partial \eta} \frac{\partial z_+}{\partial \xi} - \frac{\partial f}{\partial \xi} \frac{\partial z_+}{\partial \eta} \right) \end{aligned} \quad (11)$$

in which  $N = \rho \mu / \rho_w \mu_w$ ,  $Le$  is the Lewis number,  $Pr$  is the Prandtl number, and  $z_+ = c_+ / c_{+\delta}$ . The subscripts  $w$  and  $\delta$  refer to the values on the wall and at the edge of the boundary layer, respectively. The coordinate transformation is given by

$$\frac{d\xi}{dx} = \rho_w \mu_w u_\delta, \quad \text{and} \quad \frac{d\eta}{dy} = \frac{\rho u_\delta}{\sqrt{2\xi}}.$$

The velocity variables  $\partial f / \partial \eta = u / u_\delta$  is the usual Blasius variable. The momentum equation becomes

$$\begin{aligned} \frac{\partial}{\partial \eta} \left( N \frac{\partial^2 f}{\partial \eta^2} \right) + f \frac{\partial^2 f}{\partial \eta^2} + 2 \frac{d \ln u_\delta}{d \ln \xi} \left[ \frac{\rho_\delta}{\rho} - \left( \frac{\partial f}{\partial \eta} \right)^2 \right] \\ = 2\xi \left( \frac{\partial f}{\partial \eta} \frac{\partial^2 f}{\partial \eta \partial \xi} - \frac{\partial f}{\partial \xi} \frac{\partial^2 f}{\partial \eta^2} \right) \end{aligned} \quad (12)$$

As discussed in Hayes and Probstein (Ref. 13), one can now look for a similar, or  $\xi$ -independent solution in which the dependent variables are functions of  $\eta$  alone. This corresponds to a "constant pressure" solution in which  $p_\delta$ ,  $u_\delta$ , and  $c_{+\delta}$  are constants. It is further assumed that the condition of frozen flow exists, i.e., the reaction rates are much slower than the rate of temperature change across the boundary layer. The ion density profile  $c_+(\eta)$  is then determined by the concentration gradient alone, and  $w_i = 0$ .

At this point several comments are in order with respect to the affect of the "constant pressure" assumption on the applicability of the solution. This assumption is equivalent to saying that all flow properties at the edge of the boundary layer are only slowly varying. It was seen in Part 1 of this thesis that for a relaxing gas this is certainly not true. Most of the ionization of the gas takes place in a very short time and distance (the electron-atom ionization regime) and the "constant pressure" approximation is certainly not valid there. On the other hand, in regime I (see Appendix A of Part 1), where atom-atom ionization dominates, conditions are in fact only slowly varying, with the density and temperature approximately constant and the degree of ionization increasing very slowly. Since regime I comprises approximately 70% of the total relaxation time, the "constant pressure"

approximation is expected to be a good one in the limit of long relaxation times. Also, if the ionization relaxation time is extremely short (say less than 5  $\mu\text{sec}$ ) the "constant pressure" approximation should be good again, since if equilibrium conditions are established quickly behind the shock then in principle the variables at the edge of the boundary layer will again be slowly varying. For the present discussion, which is motivated by the need to determine the ion density for the conditions of interest to the pre-ionization experiments of Part 1, only the long relaxation time case will be considered, in which the flow external to the boundary layer consists of a slightly ionized, relaxing gas with the ionization proceeding by atom-atom collisions at the rate calculated in section 4.2 of Part 1. The pressure, temperature, and density at the edge of the boundary layer are then obtained from the shock jump conditions for a perfect gas.

If in equation (11) it is further assumed that the Prandtl number equals the Lewis number (i.e., the Schmidt number is unity), then the equation for  $z_+$  is the same as the equation for  $f'$  (the prime indicates differentiation with respect to  $\eta$ ). This is also apparent from the untransformed equations (9) and (10). With  $w_+ = 0$  and the pressure constant the equations are the same if  $\mu = \rho D_{12}$ . But the Schmidt number  $S = \mu/\rho D_{12}$ , and therefore for  $S = 1$  the untransformed equations are the same.

Since  $z_+$  and  $f'$  satisfy the same differential equation they are related by

$$z_+ = af' + b \quad , \quad (13)$$

in which  $a$  and  $b$  are constants. The boundary conditions are:

$$\begin{aligned} z_+(0) = 0 & \quad \text{and} \quad z_+(\infty) = 1 \\ f'(0) = u_s/u_\delta & \quad \text{and} \quad f'(\infty) = 1 \end{aligned}$$

Evaluating the constants leads to

$$z_+(\eta) = \frac{\frac{u_s}{u_\delta} - f'}{\left(\frac{u_s}{u_\delta} - 1\right)} = \frac{\alpha(\eta)}{\alpha_\delta} \quad , \quad (14)$$

where  $\alpha$  is the degree of ionization.

For a slightly ionized gas the ion density is given by

$$\frac{n_+}{n_{+\delta}} = \frac{\rho}{\rho_\delta} \frac{\left(\frac{u_s}{u_\delta} - f'\right)}{\left(\frac{u_s}{u_\delta} - 1\right)} \quad . \quad (15)$$

With  $N = 1$ , the momentum equation (12) reduces to the familiar Blasius equation

$$f''' + ff'' = 0, \quad (16)$$

which must now be solved with the following boundary conditions

$$f(0) = 0, \quad f'(0) = u_s/u_\delta, \quad f'(\infty) = 1.$$

Fortunately this has already been done by Mirels, and the solution is discussed in reference 14. Mirels presents tables of  $f'$  as a function of  $\eta$  for  $u_s/u_\delta = 1.5, 2, 3, 4, 5,$  and  $6$ . For a monatomic gas at moderate Mach numbers only  $u_s/u_\delta$  is of interest since for the Mach number range of 8 to 16,  $u_s/u_\delta = 3.89$  plus or minus a maximum difference of 1.8% ( $u_s/u_\delta$  equals  $\rho_2/\rho_1$ , the density jump across the shock and for  $M_s \rightarrow \infty$  in a monatomic, calorically perfect gas,  $\rho_2/\rho_1 \sim 4$ ). Mirels has also solved the energy equation, making it possible to complete the calculation of  $n_+/n_{+\delta}$ , since the pressure is constant across the boundary layer and  $\rho T = \rho_\delta T_\delta$ .

The most difficult part of the calculation using either equation (14) or (15) is the transformation back to laboratory coordinates. For  $Pr = 1$  this is simplified somewhat, but the calculation is still rather tedious. The details of the transformation are presented in reference 14 and will not be repeated here. This calculation has been carried out for the case of  $M_s = 12$  in Xenon and the resulting ion density profile is plotted in figure 8. The ion density in the boundary layer  $n_+(y)$  is normalized by the value at the outer edge of the boundary layer, and  $n_{+\delta}$  is calculated according to section 4.2 of Part 1. The abscissa is  $y/\delta$ , where  $\delta$  is the boundary layer thickness, supplied by another auxiliary calculation. This is given by Rott and Hartunian (Ref. 15) as

$$\delta = 2 \left[ \frac{\mu_2 x}{\pi \rho_2 [u_s - (\sqrt{2} - 1)(u_s - u_\delta)]} \right]^{\frac{1}{2}}, \quad (17)$$

in which  $\mu_2$  and  $\rho_2$  are the viscosity and density in the external flow (recall that  $N = \rho\mu/\rho_w\mu_w$  is assumed equal to unity for this theory).

## 5.2b. Couette flow solution.

The ion density profile in the boundary layer has also been calculated by solving the analogous problem in Couette flow. That is, the upper wall moves with velocity  $u_s$  and the lower wall moves at shock velocity  $u_s$ . The wall separation is set equal to the boundary layer thickness  $\delta$  which is calculated by equation (17). The walls are assumed to extend to plus and minus infinity in both the  $x$  and  $z$  directions, and the only variations are in the  $y$  direction, perpendicular to the walls. The lower wall corresponds to  $y = 0$  as in the shock tube. The vertical velocity  $v$  is zero. Therefore, equations (9) and (10) reduce to

$$\rho D_{12} \frac{dc_+}{dy} = \text{constant} \quad (18)$$

and

$$\tau = \mu \frac{du}{dy} = \text{constant} = \tau_w \quad (19)$$

where  $\tau$  is the shear stress and  $\tau_w$  is the shear stress at the lower wall.

The corresponding energy equation is also quite simple (see Ref. 16)

$$\tau u - q = \text{constant} = \tau_w u_s - q_w \quad (20)$$

where  $q$  is the heat flux.

Just using equations (18) and (19) and the boundary

conditions the solution for the ion density is obtained.

The result is

$$\frac{n_+(y)}{n_{+\delta}} = \frac{\rho}{\rho_{\delta}} \frac{\left( \frac{u_s}{u_{\delta}} - \frac{u}{u_{\delta}} \right)}{\left( \frac{u_s}{u_{\delta}} - 1 \right)}. \quad (21)$$

This is precisely the same as the result obtained by solving the transformed boundary layer equations (see equation (15)). However, equation (21) is already in laboratory coordinates and the complicated transformation associated with the previous solution has been eliminated. Furthermore, the velocity and density profiles can be calculated by hand, making use of the simple energy equation (2), rather than by a numerical integration of a nonlinear differential equation. In the derivation of equation (21) it was only necessary to assume that the Schmidt number was a constant.

Again assuming that  $\mu$  is proportional to  $T$  (the same as assuming  $N = 1$  in the previous calculation) the velocity profile is given implicitly by

$$\frac{y}{\delta} = \frac{\int_0^{\frac{u-u_s}{u_{\delta}-u_s}} \left( 1 + \frac{h_r-h_w}{h_w} \xi - \frac{Pr}{2h_w} (u_{\delta} - u_s)^2 \xi^2 \right) d\xi}{1 + \frac{1}{2} \frac{(h_r - h_w)}{h_w} - \frac{1}{6} \frac{Pr}{h_w} (u_{\delta} - u_s)^2} \quad (22)$$

where  $h_r$  is the recovery enthalpy and is given by

$$h_r = h_\delta + \frac{\text{Pr}}{c_p} \left[ \frac{u_\delta^2 - u_s^2}{2} - u_s(u_\delta - u_s) \right]. \quad (23)$$

The Couette flow solution for  $M_s = 12$  in Xenon, with  $\text{Pr} = 1$  is also plotted in figure 8.

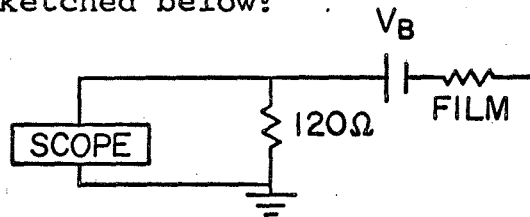
### 5.2c. Comparison of the solutions.

Figure 8 shows a comparison of the ion density profiles calculated by the two methods for a shock Mach number of 12 in Xenon, and figure 9 is a comparison of the corresponding degree of ionization profiles. For  $y/\delta$  greater than .05 the agreement is quite good. It is only very close to the probe, where the gradients are the steepest, that there are significant differences between the two solutions, and at worst the disagreement is by a factor of two.

It will be seen in section 5.3 that with the probe biases used,  $d_s$  generally corresponds to a  $y/\delta$  greater than .05. As long as this is the case, and in view of the substantial computational simplifications afforded by the Couette flow solution, it seems perfectly reasonable to use the ion density profiles based upon the Couette flow in any future investigations. The profiles have therefore been calculated for Mach numbers from 8 to 18 in Xenon and some of the results are plotted in figure 10. From figure 10 it is apparent that for  $y/\delta$  greater than .05 there is very little variation in  $n_+/n_{+\delta}$  in going from Mach 8 to 18. Most of the Mach number dependence appears in the calculation of the free stream ion density  $n_{+\delta}$ . The initial pressure dependence is reflected in the calculation of the boundary layer thickness.

### 5.3. Experimental results.

Running in Xenon and Argon in the 17" shock tube the ion density was measured as a function of time behind the incident shock wave using the thin-film gauge as a negatively biased flush electrostatic probe. The probe circuit is sketched below:



For each shock tube condition of Mach number and initial pressure two shots were made: one with  $V_B = 15$  volts, and the other with  $V_B = 45$  volts. The probe area was measured to be  $.6 \text{ cm}^2$ .

In reducing the data a value of  $d_s$  was guessed and the temperature and density at that distance into the boundary layer were used in the calculation of  $d_s$  according to equation (7). The calculated value of  $d_s$  was then used as the second guess, and so on. The cross-sections for the ion mean free path calculation were based on the results of Amdur and Mason (Ref. 17). The current  $I_+$  in equation (7) is of course the measured probe current.

The results of two of these measurements in Xenon are included in figure 8. The triangle corresponds to  $M_s = 12.0$ ,  $p_1 = 100 \mu \text{ Hg}$ , and the circle is for  $M_s = 11.8$ ,  $p_1 = 50 \mu \text{ Hg}$ . Both data points are for a bias voltage of

45 volts and a time of 50  $\mu$ sec after passage of the shock. This is a convenient way to plot the results since the time and initial pressure dependence are absorbed in the normalizing factors  $n_{+0}$  and  $\delta$ , and all the data for a given shock Mach number can be plotted on a single curve. The data points for  $M_s = 12.0$  and 11.8 are included on the same plot because of the weak Mach number dependence, as noted above.

With  $V_B = 45$  volts,  $d_s/\delta$  is greater than .05 and the Couette flow solution is acceptable. Under some conditions, for  $V_B = 15$  volts,  $d_s/\delta$  is on the order of .05 and some care must be taken in comparing the 15 volt data with the theoretical profiles.

In view of the approximate nature of the theoretical analyses the agreement between the calculated and measured values of the ion density is considered to be quite good.

## VI. SUMMARY AND CONCLUSIONS

The use of thin-film heat gauges at Mach numbers for which the shocked gas becomes partially ionized has been considered both theoretically and experimentally. It has been demonstrated that the new effects observed under these conditions cannot be explained simply on the basis of a model in which the conducting gas is viewed as providing a parallel electrical path for the gauge current, but rather the effects are due to the gauge acting more as an electrostatic probe than as a heat gauge. From this point of view it is possible to account for the qualitative observations of previous experiments, as well as those of the present experiments. It is concluded that the gauge can be thought of as a "pseudo-electrostatic probe", or a superposition of electrostatic probes at all potentials from the gauge voltage to ground.

While the use of the heat gauge as a resistance thermometer does become limited by the new effects, the gauge has been shown to provide an accurate measurement of the ionization relaxation time at the same time as it monitors the shock velocity, and by the very nature of the "probe effects" the shock velocity measurement has been appreciably simplified. In addition, by using the thin-film as an electrostatic probe the ion density history behind the incident shock is also measured. The conclusion is that contrary to previous speculation, the thin-film

gauge is even more useful as a diagnostic tool at the higher Mach numbers than it was before the ionization effects became important.

The ion density sampled by the flush probe has been related to the ion density at the edge of the shock tube boundary layer by calculating the ion density profile two different ways: first by an approximate solution of the transformed boundary layer equations, and secondly by solving the equivalent Couette flow problem. The results of the two solutions have been found to be in good agreement with each other, especially in the region of the boundary layer sampled by the probe. The Couette flow solution is recommended for any future applications of the technique in view of the computational simplifications involved.

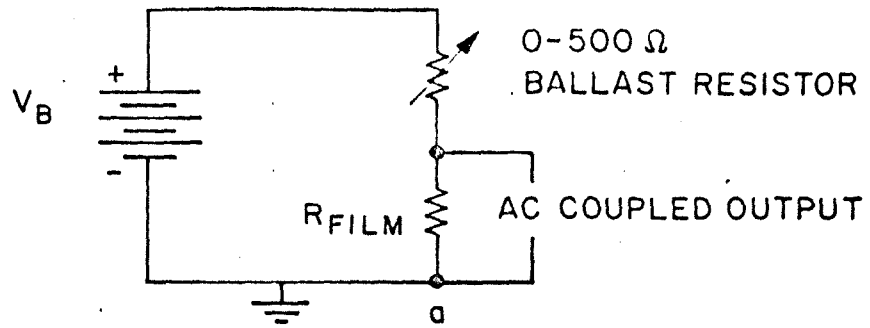
Ion number densities have been measured in the 17" shock tube in Xenon and Argon and the measured values are in good agreement with the theoretical predictions. This agreement not only checks the consistency of the experimental technique and the calculated ion density profiles, but it also serves as an important check on the method of calculating the ion density in the outer flow according to section 4.2 of Part 1 of this thesis. Since the calculation of the conductivity of the pre-ionized, relaxing gas was based on these theoretical values of  $n_{+6}$ , it was important that some experimental verification of the ion density be provided.

## REFERENCES

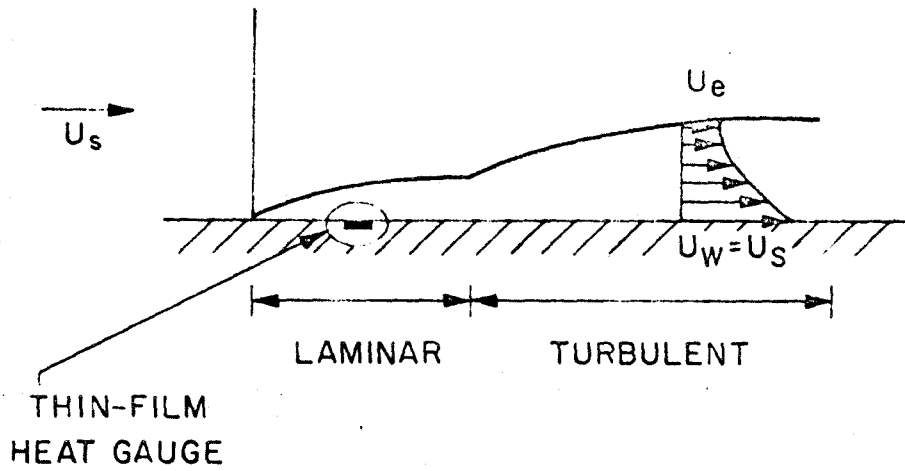
1. Rabinowicz, J., Jessey, M. E., and Bartsch, C. A., J. Appl. Phys. (1956), 27, pp. 97-98.
2. Hartunian, R. A., Russo, A. L. and Marrone, P. V., J. Aero. Sci. (1960), 27, pp. 587-594.
3. Chabai, A. J. and Emrich, R. J., J. Appl. Phys. (1955), 26, pp. 779-780.
4. Jahn, R. G. and Weimer, D., J. Appl. Phys. (1958), 29, pp. 741-742.
5. Marrone, P. V., and Hartunian, R. A., Phys. Fluids (1959), 2, pp. 719-721.
6. Kelly, A. J., Ph. D. Thesis, Caltech (1965).
7. Bredfeldt, H. R., Scharfman, W. E., Guthart, H., and Morita, T., "The Use of Ion Probes in Re-entry Physics", Stanford Research Institute, Technical Report 26 (1965).
8. Bredfeldt, H. W., Scharfman, W. E., and Guthart, H., "Boundary Layer Ion Density Profiles as Measured by Electrostatic Probes", AIAA Paper No. 66-159 (1966).
9. Chabai, A. J., "Measurement of Wall Heat Transfer and of Transition to Turbulence During Hot Gas and Rarefaction Flows in a Shock Tube", Lehigh University, Technical Report 12 (1958).
10. Mirels, H., "The Wall Boundary Layer Behind a Moving Shock Wave", published in Boundary Layer Research, H. Görtler, ed., Springer-Verlag, Berlin (1958).
11. Smith, J. A., Private communication (1966).
12. Cobine, J. D., Gaseous Conductors, Dover Publications, New York (1958).
13. Hayes, W. D., and Probstein, R. F., Hypersonic Flow Theory, Academic Press, New York (1959).
14. Mirels, H., "Laminar Boundary Layer Behind Shock Advancing into Stationary Fluid", NACA TN 3401 (1955).
15. Rott, N., and Hartunian, R., "On the Heat Transfer to the Walls of a Shock Tube", Cornell University Graduate School of Aeronautical Engineering (1955).

## REFERENCES (cont.)

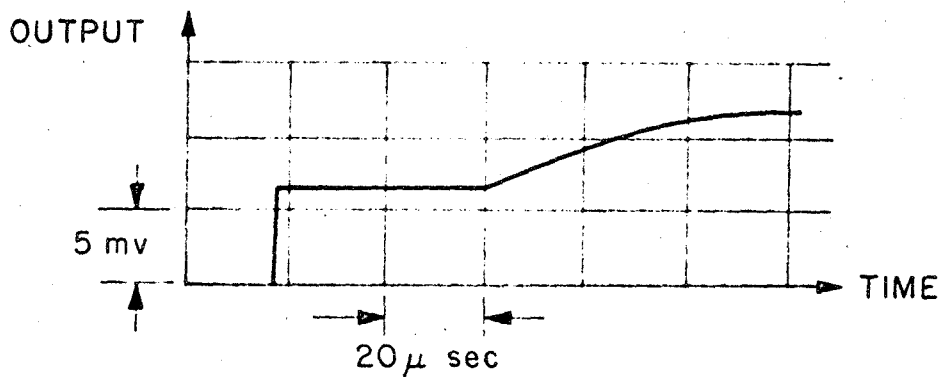
16. Liepmann, H. W., and Bleviss, Z. O., "The Effects of Dissociation and Ionization on Compressible Couette Flow", Douglas Aircraft Company Report No. SM-19831 (1956).
17. Amdur, I., and Mason, E. A., Phys. Fluids (1958), 1, pp. 370-383.



(a) HEAT GAUGE CIRCUIT.



(b) BOUNDARY LAYER IN SHOCK-FIXED COORDINATES.

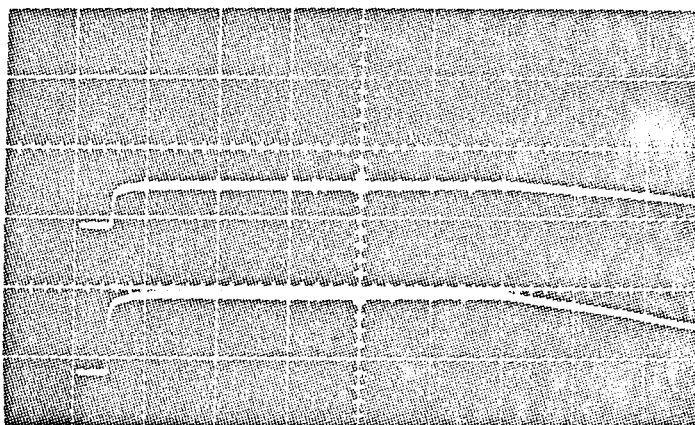


(c) TYPICAL HEAT GAUGE OUTPUT.

Figure 1. Thin-film heat gauge circuitry and output in shock tube wall boundary layer.

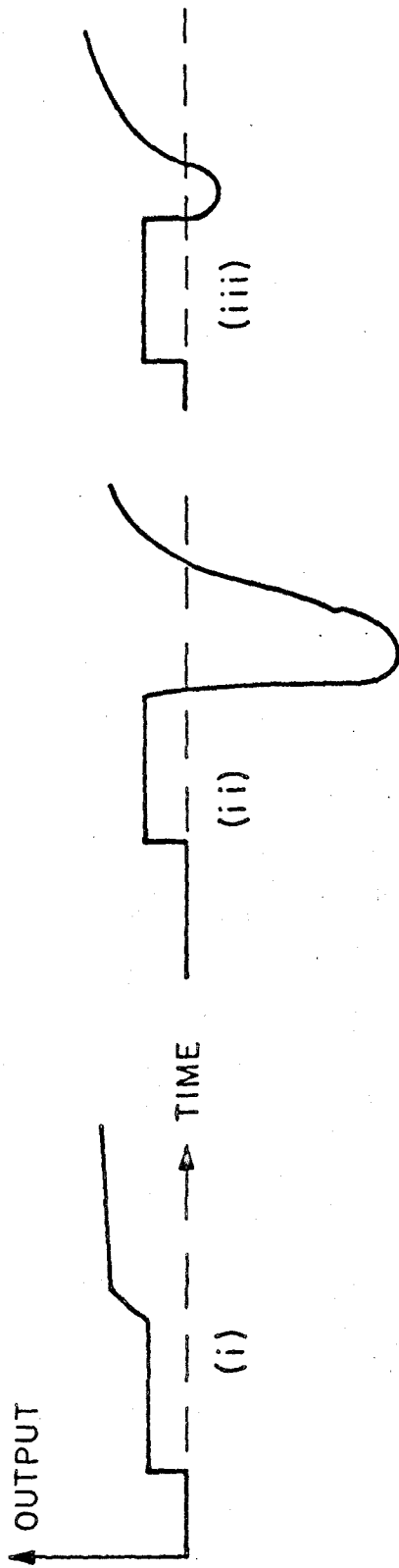


- (a) Two gauges 50 cm apart. Negative gauge voltage. Sweep rate 50  $\mu$ sec/cm, left to right; sensitivity: 10 mv/cm.  $M_s = 7.8$ ,  $p_1 = 100 \mu$  Hg of Argon.

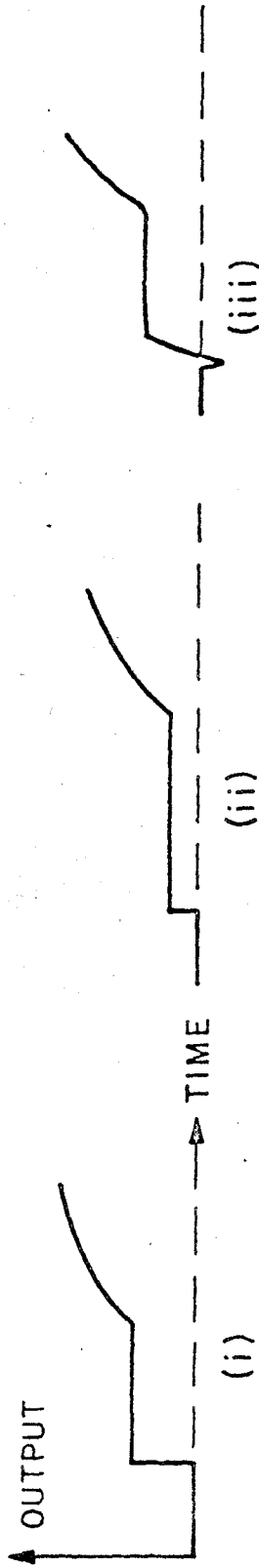


- (b) Positive gauge voltage. Sweep rate 100  $\mu$ sec/cm, left to right; sensitivity: upper beam 10 mv/cm; lower beam 5 mv/cm.  $M_s = 7.1$ ;  $p_1 = 100 \mu$  Hg of Argon.

Figure 2. Thin-film heat gauge outputs with no ionization effects.

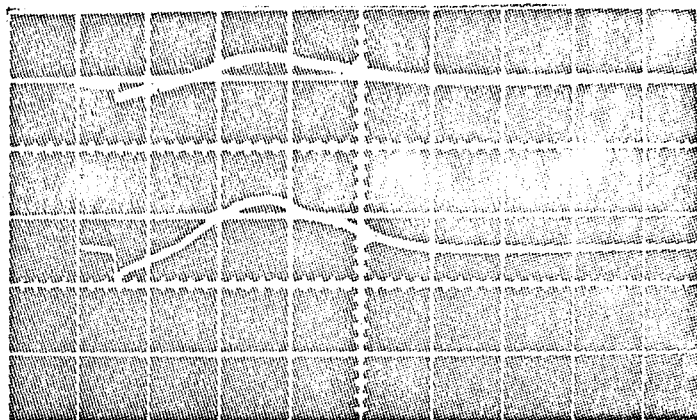


(a) Gauge outputs of Jahn and Weimer (Ref. 4) behind incident and reflected shocks in Nitrogen: (i)  $M_s = 6.5$ ,  $p_1 = 2$  mm Nitrogen; (ii)  $M_s = 5.5$ ,  $p_1 = 6$  mm Hg; (iii)  $M_s = 6.3$ ,  $p_1 = 3$  mm Hg.

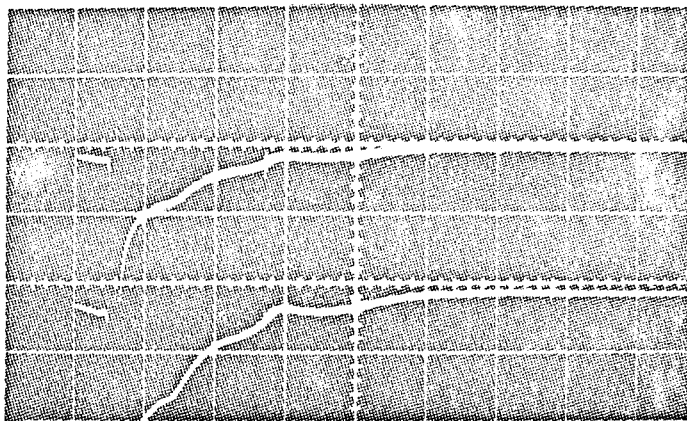


(b) Typical gauge outputs of Marrone and Hartunian (Ref. 5) behind incident shocks for  $M_s > 7$  in air: (i) expected gauge output; (ii) trace reflecting general lowering of output level; (iii) trace showing negative pulse at shock front.

Figure 3. Summary of typical observed gauge outputs.

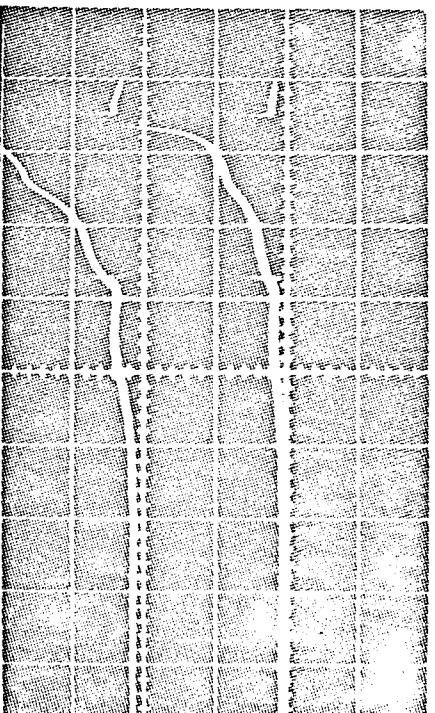


(a) Gauge voltage 6.5v negative.

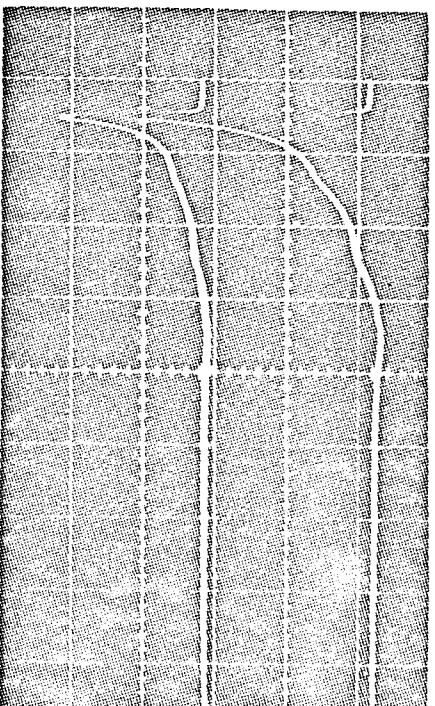


(b) Gauge voltage 6.5v positive.

Figure 4. Thin-film heat gauge output for opposite gauge voltages on successive  $M_s = 12.7$  shots into  $25 \mu$  Hg of Xenon. Sweep rate  $100 \mu\text{sec/cm}$ , left to right. Sensitivity: upper beam  $200 \text{ mv/cm}$ ; lower beam  $100 \text{ mv/cm}$ .



(a) Gauge voltage 6.5v positive.  
Sensitivity: upper beam 200 mv/cm;  
lower beam 100 mv/cm.

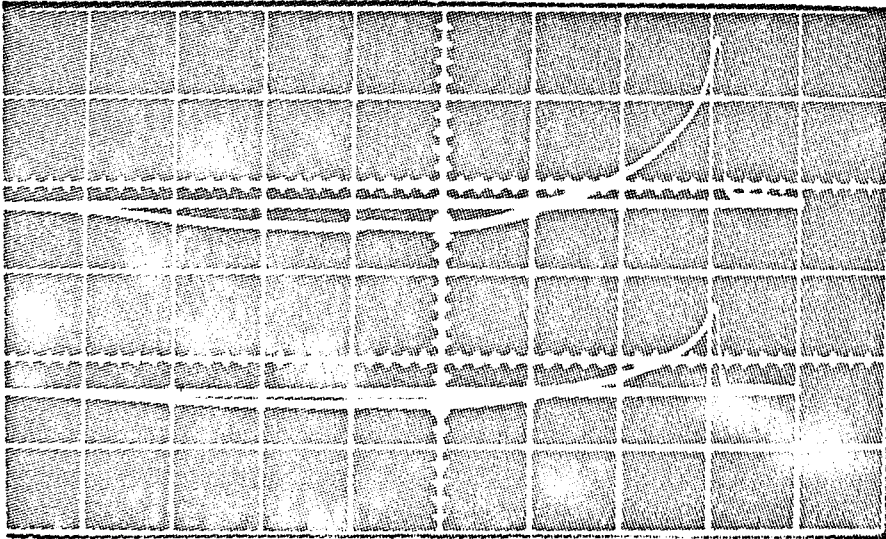


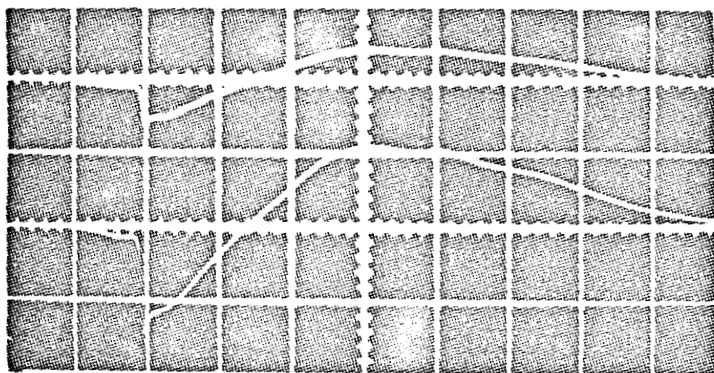
(b) Electrostatic probe biased at 6.5v  
positive. Sensitivity: upper beam  
0.5 v/cm; lower beam 1.0 v/cm.

Figure 5. Comparison between heat gauge output  
and electrostatic probe.  $M_s = 12.7$ ,  
 $P_1 = 25 \mu$  Hg of Xenon. Sweep rate  
100  $\mu$ sec/cm, left to right.

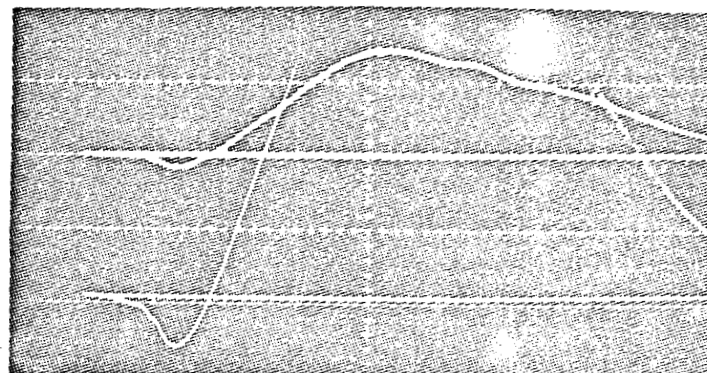
Electrostatic probe output with zero bias voltage.  $M_s = 12.7$ ,  $P_1 = 25 \mu$  Hg of Xenon. Sweep rate  $50 \mu\text{sec/cm}$  left to right. Sensitivity: upper beam  $1.0 \text{ V/cm}$ ; lower beam  $0.5 \text{ V/cm}$ .

Figure 6.

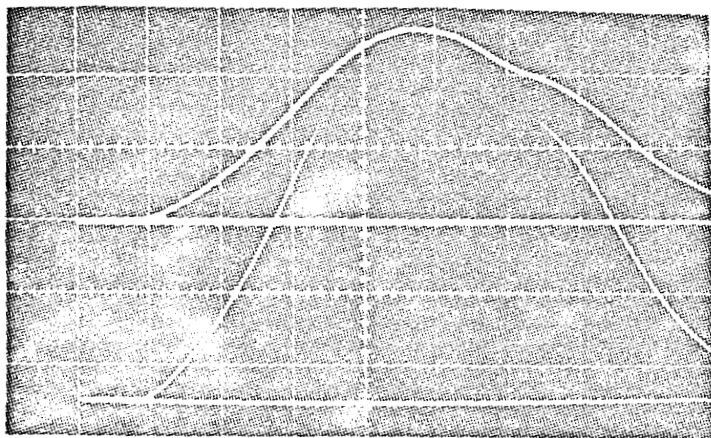




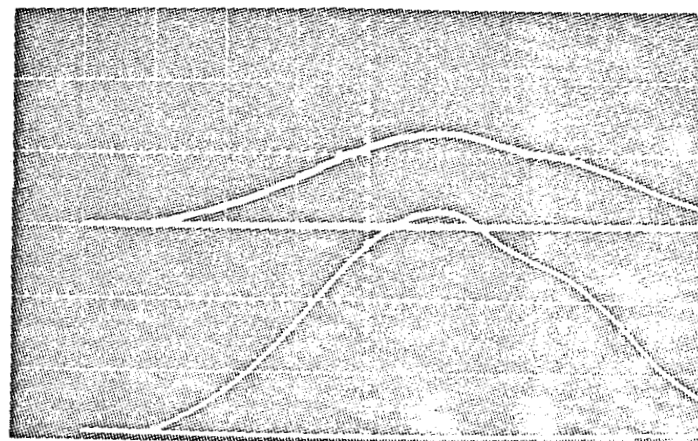
(a) Bias: 3v negative. Sensitivity:  
Upper .5v/cm; Lower .2v/cm.



(b) Bias: 6.5v negative. Sensitivity:  
Upper .2v/cm; Lower .05v/cm.



(c) Bias: 12v negative. Sensitivity:  
Upper .2v/cm; Lower .1v/cm.



(d) Bias: 15v negative. Sensitivity:  
Upper .5v/cm; Lower .2v/cm.

Figure 7. Flush Electrostatic Probe Output as a Function of Bias Voltage.  
 $M_s = 12.7$ ,  $p_1 = 25 \mu$  Hg of Xenon. Sweep Rate  $50 \mu$ sec/cm, left to right.

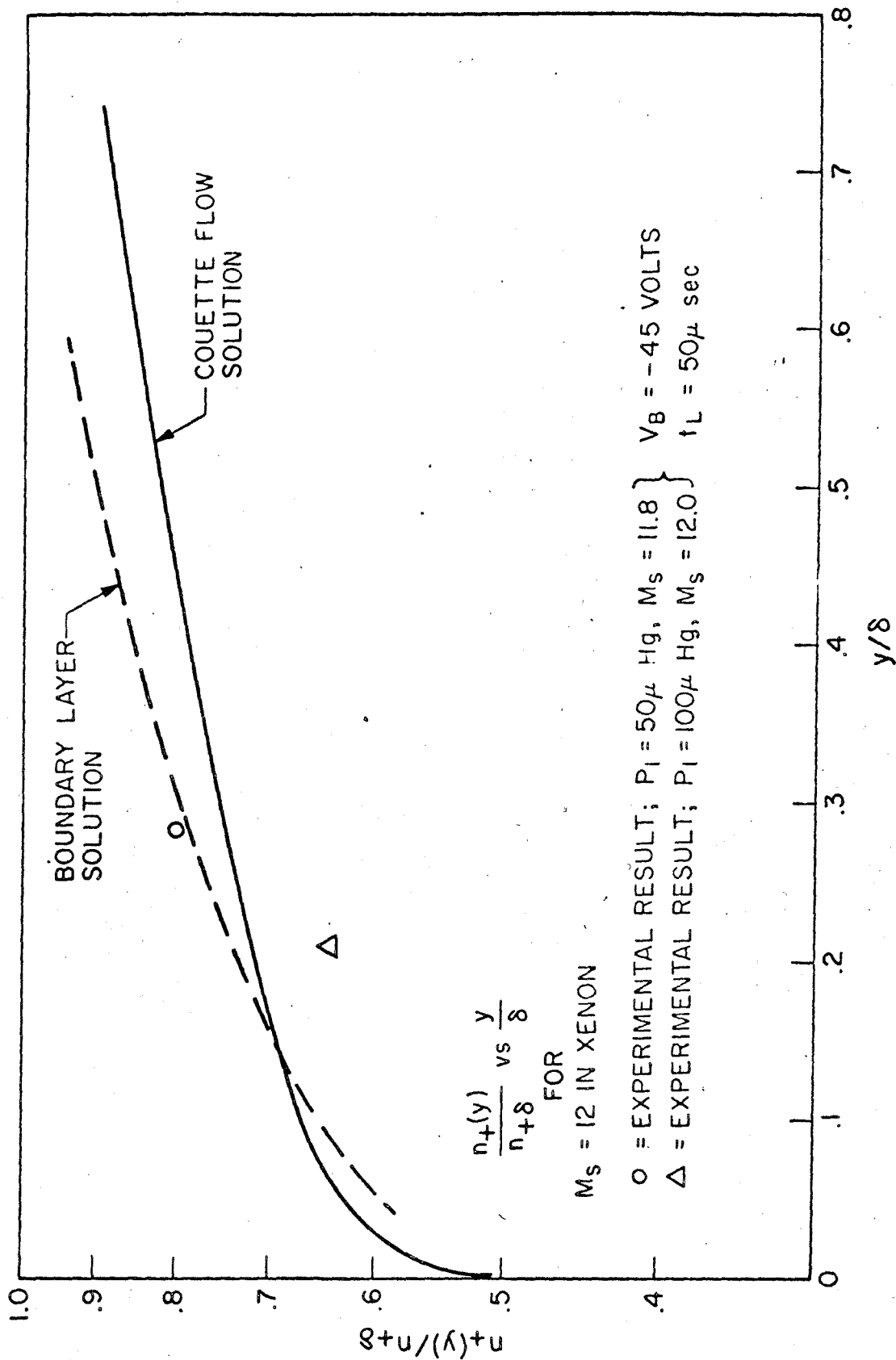


Figure 3. Ion density in the boundary layer; theories and experiments.

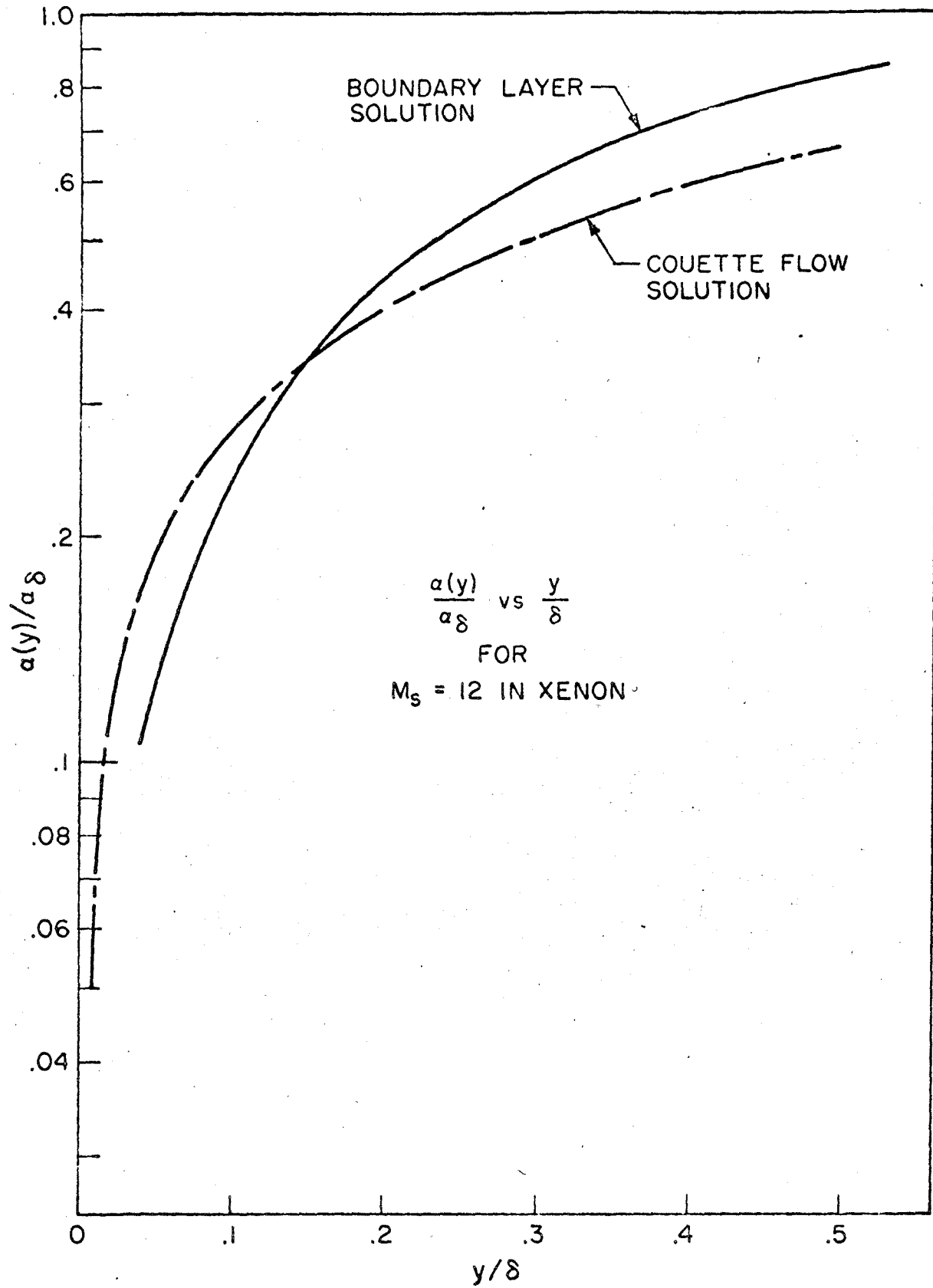


Figure 9. Degree of ionization in the boundary layer.

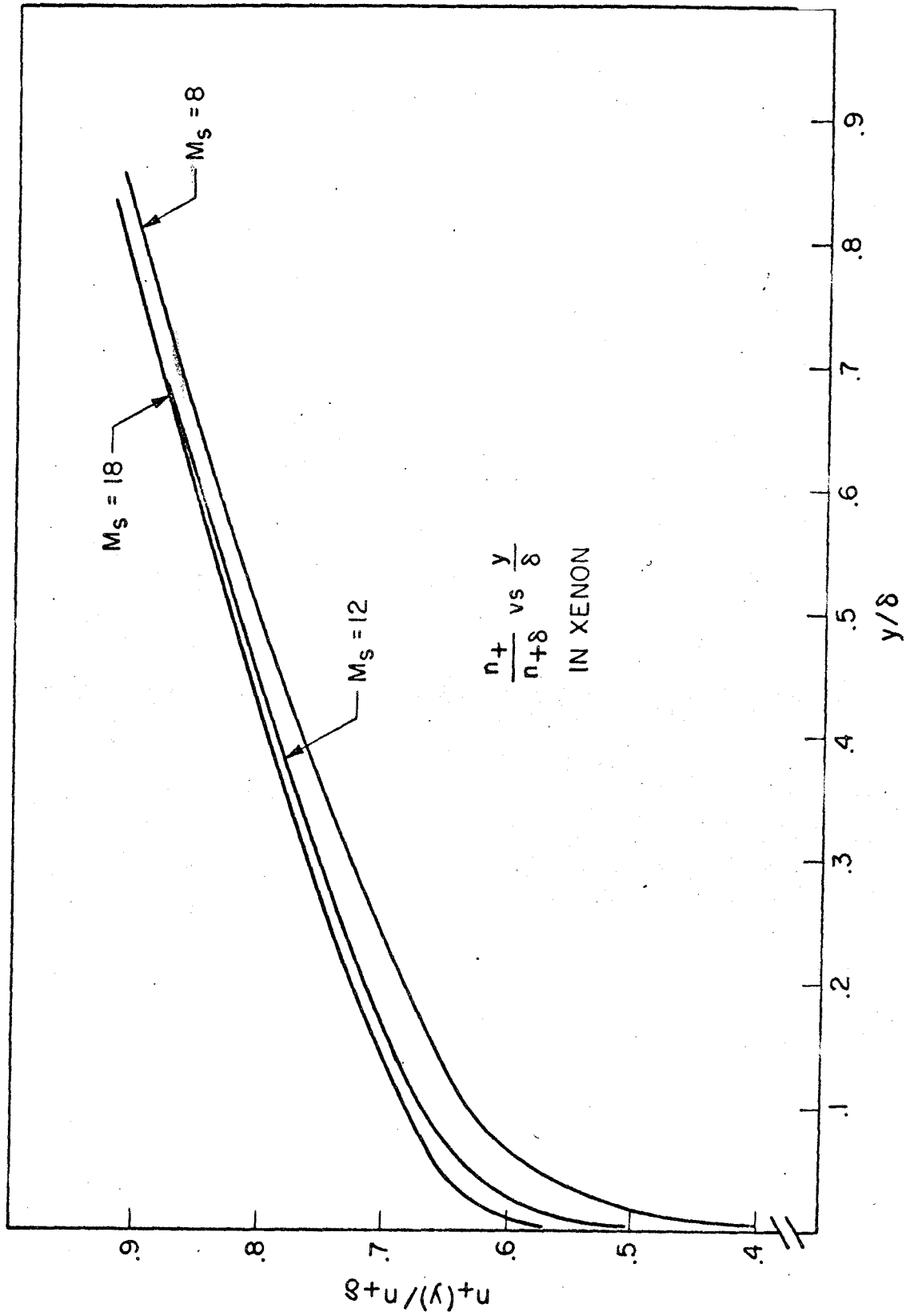


Figure 10. Ion density profiles in Xenon; Couette flow solution.